THE UNIVERSITY OF NOTTINGHAM

DEPARTMENT OF ELECTRICAL AND ELETRONIC ENGINEERING

Development of Digital Filtering Techniques in Three-Dimensional TLM Models

By:

Rawin Vongurai, BEng (Hons.)

**Thesis submitted to the University of Nottingham
for the degree of Doctor of Philosophy**

April 2013

Abstract

Digital filtering (DF) techniques are receiving significant interest, because they can represent fine features such as vias, thin-panels and thin-wires in full-field solutions of electromagnetic problems with significant savings in computational costs. However, a limitation of this technique is that DF can only represent a fine feature as a plane or as an internal boundary. In other words, an internal boundary can represent the electromagnetic properties of a fine feature in one dimension or two directions.

The DF technique is usually involved with time domain solvers such as the Finite-difference time-domain (FDTD) and the Transmission Line Modeling (TLM) methods. Both of them are commonly used to investigate the electromagnetic fields in the problem spaces. Here the TLM method is selected for demonstrating the DF technique.

This thesis presents the formulation of TLM in three-dimensions in order to investigate the limitations of the DF technique and the solutions. As a result, new techniques have been developed. These techniques can be applied to the three dimensional TLM method in order to represent the fine features in three-dimensions appropriately.

The developed techniques were demonstrated using some examples of three-dimensional embedded objects, such as conducting volumes and dielectrics. Their accuracy and efficiency are compared with the standard TLM method in the time and frequency-domain. The results show good agreement between these techniques and the standard TLM method.

Publications

[1]   V. Rawin, C. Christopoulos, D. Thomas, S. Greedy, " Application of digital filtering techniques in three-dimensional multi-scale problems," Antennas and Propagation Conference (LAPC), 2011 Loughborough, pp. 1 − 4, 14th-15th Nov. 2011.

[2]   V. Rawin, C. Christopoulos, D. Thomas, S. Greedy, " Application of Digital Filtering Techniques in Field Solvers to Represent Small Embedded Features in a Coarse Mesh," Progress in Electromagnetics Research Symposium (PIERS), Kuala Lumpur, Malaysia, 27th - 30th March 2012.

[3]   R. Vongurai, C. Christopoulos, D. Thomas, "Embedded structures modeled by digital filter interfaces in time-domain electromagnetic models," Electromagnetics in Advanced Applications (ICEAA), 2012 International Conference, pp. 186-189, 2nd-7th Sept. 2012.

[4]   V. Rawin, C. Christopoulos, D. Thomas, S. Greedy, "The Representation of Small Embedded Features in a Coarse Mesh Using Digital Filtering Techniques in 3D Time-Domain Field Solvers ," *IEEE Trans. on Microwave Theory and Techniques* (under review)

Acknowledgements

First and foremost, I would like to express gratitude to Professor Christos Christopoulos for giving me the opportunity to study for a PhD under his supervision. He has always been very kind and gentle towards me. I can say that I am the luckiest person in the world. Even after his retirement, he helped, supported and encouraged me to complete my studies successfully.

Secondly, I would like to express my gratitude towards Professor Dave Thomas. He is a person who always makes me smile; I have never felt any pressure during our meetings. He always supported me, helped me, understood me and brought me up to finishing my study. I really appreciate everything he had done for me.

I would like to thank my co-supervisors Dr. Steve Greedy and Professor Phillip Sewell. I would also like to thank all my friends and members of the George Green Institute for Electromagnetics Research.

Lastly, I would like to thank my parents and my family very much for their support.

Contents

List of Symbols

Notation	Description
$\vec{E}$	Electric field
$\vec{H}$	Magnetic field
Δl	Spatial sampling (space-step)
Δt	Temporal sampling (time-step)
x, y, z	Rectangular coordinate system
$\Delta x, \Delta y, \Delta z$	Nodal mesh size
k	Temporal iteration number
λ_0	Wave-length of free space
μ_0	Dielectric permeability of vacuum
μ_r	Dielectric permeability of material
ε_0	Vacuum permittivity
ε_r	Relative permittivity of material
v	Velocity of propagation
c	Velocity of light in freespace
ω	Angular frequency
Z_0	Intrinsic impedance

Notation	Description
NP	Number of poles
NZ	Number of zeros
$\Re$	Real part of a complex number
$\Im$	Imaginary part of a complex number
DF	Digital filtering
$DF(\ )$	Digital filtering function
S	Scattering matrix
SCN	Symmetrical Condensed Node

1. Introduction

1.1 Introduction and Objective of the Thesis

Most popular methods used by scientists and engineers to analyse electromagnetic phenomena include analytical methods and or numerical methods such as Transmission Line Modelling (TLM) [1.1]-[1.2], Finite Difference Time Domain (FDTD) [1.3] - [1.4], Finite Element Method (FEM) [1.5] and Method of Moments (MOM) [1.6]. TLM and FDTD are differential equation based techniques for full field solutions of electromagnetic problems. These techniques solve Maxwell's equations, by creating a mesh over the problem space and iteratively solving for the electromagnetic fields in the mesh. The accuracy of the solution depends on the resolution of the mesh and how well it represents the problem space.

In general, solving a complex problem using numerical methods incur high computational costs in computer-memory and simulation-time because a network with a very fine mesh (size of the mesh is smaller compared to the wavelength) is required. The general example of this problem is the modelling of a wire embedded inside a cabinet. The wire diameter is usually much smaller than the wavelength, while the mesh size is comparable to the

wavelength. Problems of this type are described as multi-scale problems [1.7] as discussed in the next section.

1.1.1 Multi-scale Problems

Consider a thin wire located inside a regular mesh as shown in Fig.1.1.
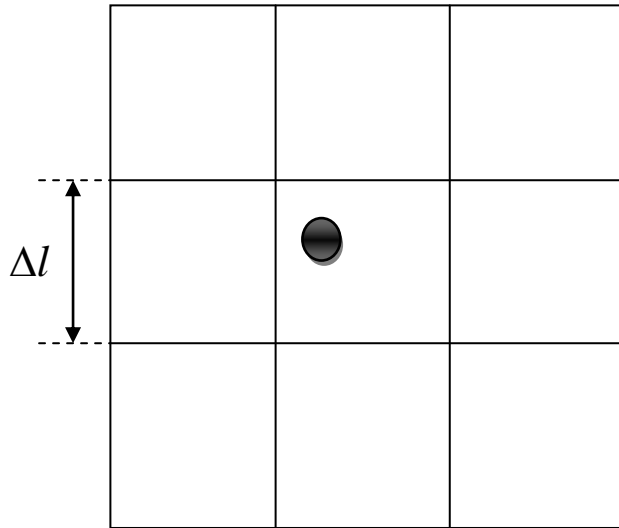
Fig.1.1 A thin wire of radius less than mesh size inside a regular mesh

Fig.1.1 shows a thin wire with a radius smaller than the mesh size with spatial resolution or space-step (Δl). Therefore, it is impossible to simulate the model directly. The straightforward way to solve this problem is to decrease the size of the space step Δl to be less than or equal to the radius of thin wire. However, this solution requires high computational effort. Alternative methods avoiding these problems include applying (i) a hybrid mesh or (ii) a multi-grid mesh as illustrated in Fig.1.2 and 1.3 respectively.
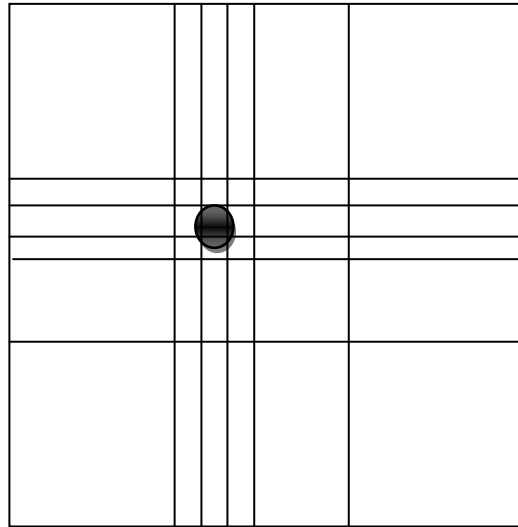
Fig.1.2 A thin wire of radius inside hybrid mesh
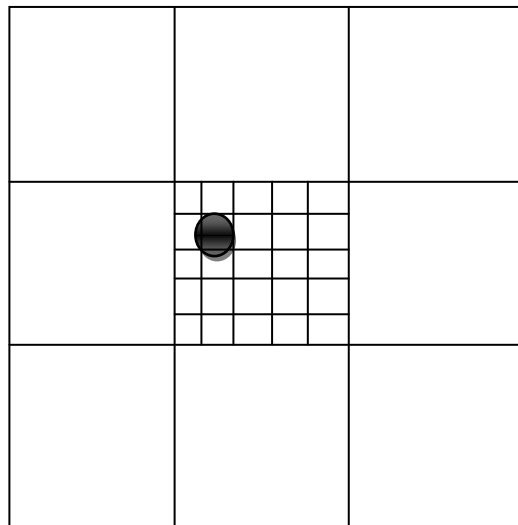
Fig.1.3 A thin wire of radius inside multigrid mesh

In Fig.1.2, The obvious advantage of the hybrid mesh is that the fine mesh is not required over the entire problem space. In addition, it is not mandatory for a node to be a square (2D) or a cube (3D) in space, and can be shaped according to the required resolution in each direction. Also, the small time step

is determined by the smallest cell. However, the disadvantage is the difficulty in precisely determining the loss of accuracy for high grading ratios. A complete theoretical development and implementation details regarding the hybrid mesh can be found in [1.2] and [1.8].

From Fig.1.3, one can infer that the advantages of a multi-grid mesh are (i) locally applied fine mesh (ii) that other model developments are not required to describe the fine features. However, the main disadvantage is the difficulty in modelling the information transfer at the interface between the fine and coarse mesh regions because they have different spatial and temporal granularity. At the moment, there exist several solutions to minimise and overcome this problem. One of the popular techniques that can be used to solve this problem is described in the next section.

1.1.2 Transmission-Line Modelling Method

The Transmission-Line Modelling (TLM) Method is a numerical method for investigating electromagnetic fields in the time or frequency domain. This work will focus on the time-domain TLM. Basically, physical systems can be modelled using a network of transmission-lines with propagating voltages and currents. For electromagnetic field modelling, the voltages and currents are related to the electric and magnetic fields. The TLM method can be applied to one, two and three dimensional problems. The one-dimensional TLM method is commonly used to study basic physical systems such as electrical circuits. The two-dimensional TLM method has the same fundamental and computational procedure as the one-dimensional TLM method and is used to solve two dimensional problems like planar microwave circuits. However, more practical problems require the three-dimensional TLM method. The

three-dimensional TLM method will be considered and described in the next chapter.

In Transmission-Line Modelling (TLM) method, a well-known technique that was developed for multi-grid mesh problems is the TLM multiple grid scheme method [1.2], [1.9] and [1.10] ,which uses a range of fine and coarse mesh regions, to describe the electromagnetic field behaviour in a problem space under the following four conditions, in order to maintain synchronism and connectivity in the modelling of different parts of space in TLM (the location at the interface between the fine and coarse mesh regions). The conditions are;

(i)   Charge conservation

(ii)   Energy conservation

(iii)   No reflections

(iv)   Zero delays

However, it is not possible to follow all of these four conditions at the same time. Therefore, a compromise is required [1.2].

There is also another technique that can be applied in TLM for the same purpose called Digital filtering (DF) technique [1.11] as introduced and described in section 1.1.3 and chapter 3 respectively. However, there are some limitations and conditions to apply this technique in the TLM method as discussed in Chapter 3.

Another solution is to glue the two meshes together with an unstructured mesh [1.12].

The objective of this thesis is to implement and further develop DF techniques for the TLM method to represent more general problems especially, the

properties of fine embedded objects in three-dimensions, with benefits in terms of computational cost savings.

1.1.3 Digital Filtering Techniques

The digital filtering (DF) technique is applied in the three-dimensional TLM method, in order to represent the behaviour of fine embedded features such as thin panels, wires and materials with frequency-dependent properties [1.13]-[1.15]. The DF technique combines four techniques—the Fast Fourier Transform (FFT), the Frequency-domain Prony's method [1.16], Laguerre's Method [1.17] -[1.19] and Bilinear-Z-transform. They are employed to estimate the DF parameters of a fine feature. Then, these parameters are used to construct the digital filters representing the properties and field characteristics of the fine feature. Moreover, the purpose of these techniques is to substitute the fine embedded feature with a digital filter which gives the same behaviour, but with lower computational requirements.

1.2 Outline of the Thesis

Chapter two begins by introducing the basic theory of the TLM method. Then, the three-dimensional TLM method is described; first, the development of the three-dimensional node is presented. Details of the symmetrical condensed node (SCN) [1.2], [1.20]-[1.21] are then explained. Then, the propagation properties and the computations in the SCN meshes are given. The chapter also covers the techniques to excite and measure the field components at a node.

The SCN with capacitive and inductive stubs is described and the scattering and calculation of electromagnetic field in a stubbed SCN are given.

Chapter three introduces the DF techniques. Then, it is demonstrated how to apply the FFT, the Frequency-domain Prony's method, Laguerre's Method and Bilinear-Z-transform to obtain the DF parameters. It is also shown how to employ these parameters in connection with the three-dimensional TLM method. The conditions for selecting the sampling interval for the techniques are described. In addition, the implementation of the digital filter and the use of DF techniques in a three-dimensional TLM simulation are summarised in schematic and block diagrams.

Chapter four begins with discussion on the original research by investigating the problems and limitations of the DF techniques combined with the three-dimensional TLM method. Then, the DF technique is developed to minimize and overcome these problems. The example of a thin-wire (conducting post) placed between two parallel metal plates inside a large volume of space with matched-boundary condition (Mur's absorbing boundary in FDTD [1.22]) is presented in order to demonstrate the effectiveness of the proposed techniques. This example also provides the comparisons between the three-dimensional TLM method and the developed DF techniques in time- and frequency-domain and in terms of their respective computational costs. Some limitations and conditions of the developed DF techniques are described in the chapter.

Chapter five investigates and develops the DF techniques given in chapter four to be able to use with general problems in three-dimensions. The DF techniques are developed and successfully applied to the representation of a fine-embedded object in a coarse mesh by extracting the DF parameters using a TLM fine mesh simulation. The methods and procedures are explained. The validations and limitations of the technique are also given. Examples of joining

DF-nodes to replicate the properties of conductors and dielectric materials are presented. At the conclusion, this technique is summarised in block diagrams.

Chapter six summarises the conclusions of the work and outlines the strengths and weaknesses of the DF technique developed. Further work for the development of the DF techniques is then proposed.

1.3   References

[1.1]   C. Christopoulos, *The Transmission-Line Modeling Method: TLM. New York*: IEEE Press, 1995.

[1.2]   R.A. Scaramuzza, and C. Christopoulos, "*Developments in TLM and its application in EM field simulation*", InLJml.Comp. and Maths, COMPEL, pp. 49-52, (11), 1992.

[1.3]   K.S. Kunz, and R.J. Luebbers, *The finite difference time domain method for electromagnetics.* Boca Raton: CRC Press. pp. 448, 1993.

[1.4]   A. Taflove, and S.C. Hagness, *Computational electrodynamics : the finite-difference time-domain method.* 3rd ed. Artech House antennas and propagation library, Boston: Artech House. xxii, pp. 1006, 2005.

[1.5]   J.L. Volakis, A. Chaterjee, L.C. Kempel, *Finite Element Method for Electromagnetics*, New York: IEEE Press, 1998.

[1.6]   R.F. Harrington, *Field Computation by Moment Methods.* New York: McMillan, 1968.

[1.7]   C. Christopoulos, "Multi-Scale Modeling in Time-Domain Electromagnetics", *International Journal of Electronic Communication* (AEU), vol.57, (2), pp. 100-110. 2003.

[1.8]   V. Trenkic, C. Christopoulos and T.M. Benson, "On the time step in hybrid symmetrical condensed TLM nodes," *IEEE Trans. on Microwave Theory and Techniques*, vol 43, pp. 2172–2174, 1995.

[1.9]   J.L. Herring, and C. Christopoulos, "Solving electromagnetic field problems using a multiple grid transmission-line modeling method," *IEEE Transactions on Antennas and Propagation.*, vol. 42, (12), pp. 1654-1658, Dec 1994.

[1.10] J.L. Herring, C. Christopoulos, "Multigrid TLM method for solving EM field problems," Electronics Letters, vol. 27, pp. 1794–1795, 1991.

[1.11] J. Paul, V. Podlozny, and C. Christopoulos, "The use of digital filtering techniques for the simulation of fine features in EMC problems solved in the time domain," *IEEE Trans. Electromagn. Compat.*, vol. 45, (2), pp. 238-244, May 2003.

[1.12] P. Sewell, J.G. Wykes, T.M. Benson, D.W.P. Thomas, A. Vukovic and C. Christopoulos, "Transmission line modeling using unstructured meshes," *IEEE Trans. Science, Measurement & Technology*, vol. 151, (6), pp. 445-448, 4 Nov. 2004.

[1.13] J. Paul, C. Christopoulos, and D. W. P. Thomas, "Generalized material models in TLM—Part 1: Materials with frequency-dependent properties," *IEEE Trans. Antennas Propagat.*, vol. 47, pp. 1528–1534, Oct.1999.

[1.14] J. Paul, C. Christopoulos, and D. W. P. Thomas, "Generalized material models in TLM—Part 2: Materials with anisotropic properties," *IEEE Trans. Antennas Propagat.*, vol. 47, pp.1535–1542, Oct. 1999.

[1.15] J. Paul, C. Christopoulos, and D. W. P. Thomas, "Generalized material models in TLM—Part 3: Materials with nonlinear properties," *IEEE Trans. Antennas Propagat.*, vol. 50, pp. 997–1004, July 2002.

[1.16] J. N. Brittingham, E. K. Miller, and J. L. Willows, "Pole extraction from real-frequency information," *Proc. IEEE*, vol. 68, pp. 263-273, Feb. 1980.

[1.17] W.H. Press, S.A. Teukolsky, W.T. Vetterling and B.P. Flannery, *Numerical Recipes: The Art of Scientific Computing,* 3rd ed., New York: Cambridge University Press, 2007.

[1.18] A. Ralston and P. Rabinowitz, *A First Course in Numerical Analysis*, 2nd ed., New York: Dover, 2001.

[1.19] D.A. Adams, "A Stopping Criterion for Polynomial Root Finding," *Communications of the ACM*, vol. 10, pp. 655-658.

[1.20] P. B. Johns, "A Symmetrical Condensed Node for the TLM Method," *IEEE Trans. Microwave Theory Tech.*, vol. 35, no. 4, pp. 370-377, Apr. 1987.

[1.21] P. P. M. So and W. J. R Hoefer, "A new look at the 3D condensed node TLM scattering," *IEEE Int. Microwave Symp. Dig.,* Atlanta, Ga, pp. 1443-1446, June 1993.

[1.22] G. Mur, "Absorbing boundary conditions for the finite-difference approximation of the time-domain electromagnetic-field equations." *IEEE Trans. Electromagn. Compat*., vol. 23, pp. 377-382, Nov. 1981.

2.   Three-Dimensional TLM

2.1   Introduction and development of Three-Dimensional TLM

The three-dimensional TLM network originally developed by combining two-dimensional shunt and series nodes [2.1] as shown in Fig.2.1 with a time step delay between them is known as the *expanded node* network [2.2]. The main advantage of this network is that three of the six field components $\left(E_x, E_y, E_z, H_x, H_y, H_z\right)$ can be determined at each scattering point.
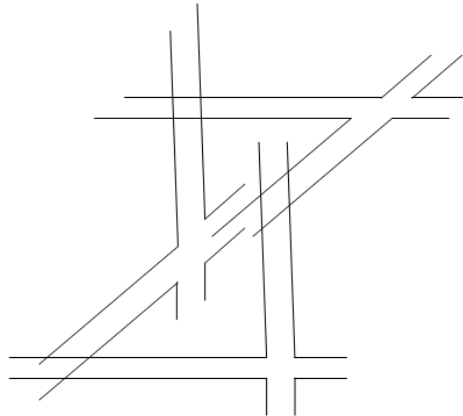

Fig.2.1 An expanded node.

The expanded node has been employed for solving three-dimensional electromagnetic problems over many years [2.3]. However, the complicated

topology of the computational cell causes errors and difficulty in modelling boundaries. The scattering points, where the field components are determined are spatially separated and cannot also be updated at the same time. Because of these problems, a more compact node was developed and is referred to as the *asymmetrical condensed node* [2.4]. It is simply a three-dimensional node, which all field components are calculated at the same point. In other words, all scattering processes of the node is placed at one point in the field space. The boundary conditions can be applied either at the node or in between nodes. Moreover, it is asymmetrical because the first connection to the node can be either to a shunt or to a series node, depending on the direction of the observation. More information on the asymmetrical condensed node can be found in [2.4] and [2.5]. Another compact three-dimensional node is the *three-dimensional symmetrical condensed TLM node* (3D-SCN) introduced by Johns in 1986 [2.6] as illustrated in Fig.2.2. The 3D-SCN node whose scattering properties obtained by energy and charge conservation [2.7] minimises the problems of the expanded and asymmetrical condensed nodes. The 3D-SCN is explained in the next section.
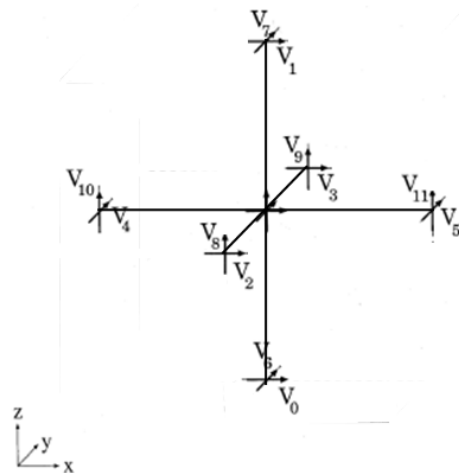

Fig.2.2 A three-dimensional symmetrical condensed TLM node.

2.2   Three-Dimensional Symmetrical Condensed Node

The 3-D SCN node represents a block of space with size Δl^3 where $\Delta l = \Delta x = \Delta y = \Delta z$. It contains twelve ports in order to represent the two field polarisations at the centre of each face of the cell. Moreover, the scattering matrix of the node (S) relating the vector of scattered voltages $(\vec{V}^r)$ to the vector of incident voltages $(\vec{V}^i)$ is given in (2.1).

$$\vec{V}^r = S\vec{V}^i \qquad (2.1)$$

where i and r are incident and scattered ports respectively.

Let us consider an incident voltage pulse excited into port 0 of the TLM node in Fig.2.2. This pulse is x-directed. Therefore, it is associated with the field components E_x and H_y. Maxwell's equations relating these field components are

$$\frac{\partial H_y}{\partial z} - \frac{\partial H_z}{\partial y} = \varepsilon \frac{\partial E_x}{\partial t} \qquad (2.2)$$

$$\frac{\partial E_z}{\partial x} - \frac{\partial E_x}{\partial z} = -\mu \frac{\partial H_y}{\partial t} \qquad (2.3)$$

Equation (2.2) implies that an incident pulse on port 0 can scatter back into port 0 since it is reflected, port 1 because it is associated with E_x and H_y, ports 2 and 3 because they are associated with E_x and H_z. Equation (2.3)

25

implies that the pulse can also scatter into ports 10 and 11, since they are associated with E_x and H_y.

Moreover, let us consider that the magnitudes of the pulses scattered into ports 0 and 1 are a and c respectively. The magnitudes of the pulses scattered into ports 2 and 3 are equal because of the symmetry of the node and are considered as b. Similarly, the magnitudes of the pulses scattered into ports 10 and 11 have the same amplitude but have opposite signs and are considered as d and $-d$ respectively. When this procedure is applied to all ports, the S can be determined through the use of the laws of conservation of power [2.7] as described in [2.1]. Consequently, it becomes the 12 x 12 matrix given in (2.4).

$$
S = \begin{vmatrix}
a & c & b & b & & & & & & & d & -d \\
c & a & b & b & & & & & & & -d & d \\
b & b & a & c & d & -d & & & & & & \\
b & b & c & a & -d & d & & & & & & \\
 & & d & -d & a & c & b & b & & & & \\
 & & -d & d & c & a & b & b & & & & \\
 & & & & b & b & a & c & d & -d & & \\
 & & & & b & b & c & a & -d & d & & \\
 & & & & & & d & -d & a & c & b & b \\
 & & & & & & -d & d & c & a & b & b \\
d & -d & & & & & & & b & b & a & c \\
-d & d & & & & & & & b & b & c & a
\end{vmatrix}
\qquad (2.4)
$$

For a lossless network where the total scattered power is equal to the total incident power, the unknown parameters a, b, c and d can be determined

[2.1]. Therefore, s for a lossless network can be obtained as shown in (2.5) and is referred to as a *regular mesh*.

$$
S = 0.5 \begin{vmatrix}
0 & 0 & 1 & 1 & & & & & & & 1 & -1 \\
0 & 0 & 1 & 1 & & & & & & & -1 & 1 \\
1 & 1 & 0 & 0 & 1 & -1 & & & & & & \\
1 & 1 & 0 & 0 & -1 & 1 & & & & & & \\
& & 1 & -1 & 0 & 0 & 1 & 1 & & & & \\
& & -1 & 1 & 0 & 0 & 1 & 1 & & & & \\
& & & & 1 & 1 & 0 & 0 & 1 & -1 & & \\
& & & & 1 & 1 & 0 & 0 & -1 & 1 & & \\
& & & & & & 1 & -1 & 0 & 0 & 1 & 1 \\
& & & & & & -1 & 1 & 0 & 0 & 1 & 1 \\
1 & -1 & & & & & & & 1 & 1 & 0 & 0 \\
-1 & 1 & & & & & & & 1 & 1 & 0 & 0
\end{vmatrix} \tag{2.5}
$$

2.2.1 The Connection Process for the Regular SCN Mesh

In order to establish the connection process between regular SCN nodes, suppose that an incident voltage pulse is excited into port 10 at node (x, y, z) in Fig.2.3 at time-step k, such that $_kV_{10}^i(x,y,z)=1$. It will propagate along the x-direction with the electric field polarised in the z-direction generating the scattered voltages as given in (2.6).

$$
_kV_8^r(x,y,z)=_kV_9^r(x,y,z)=_kV_0^r(x,y,z)=-_kV_1^r(x,y,z)=0.5 \tag{2.6}
$$

The other scattered voltages are equal to zero. These scattered voltages will then propagate into the neighbouring nodes at the next time-step $k+1$.

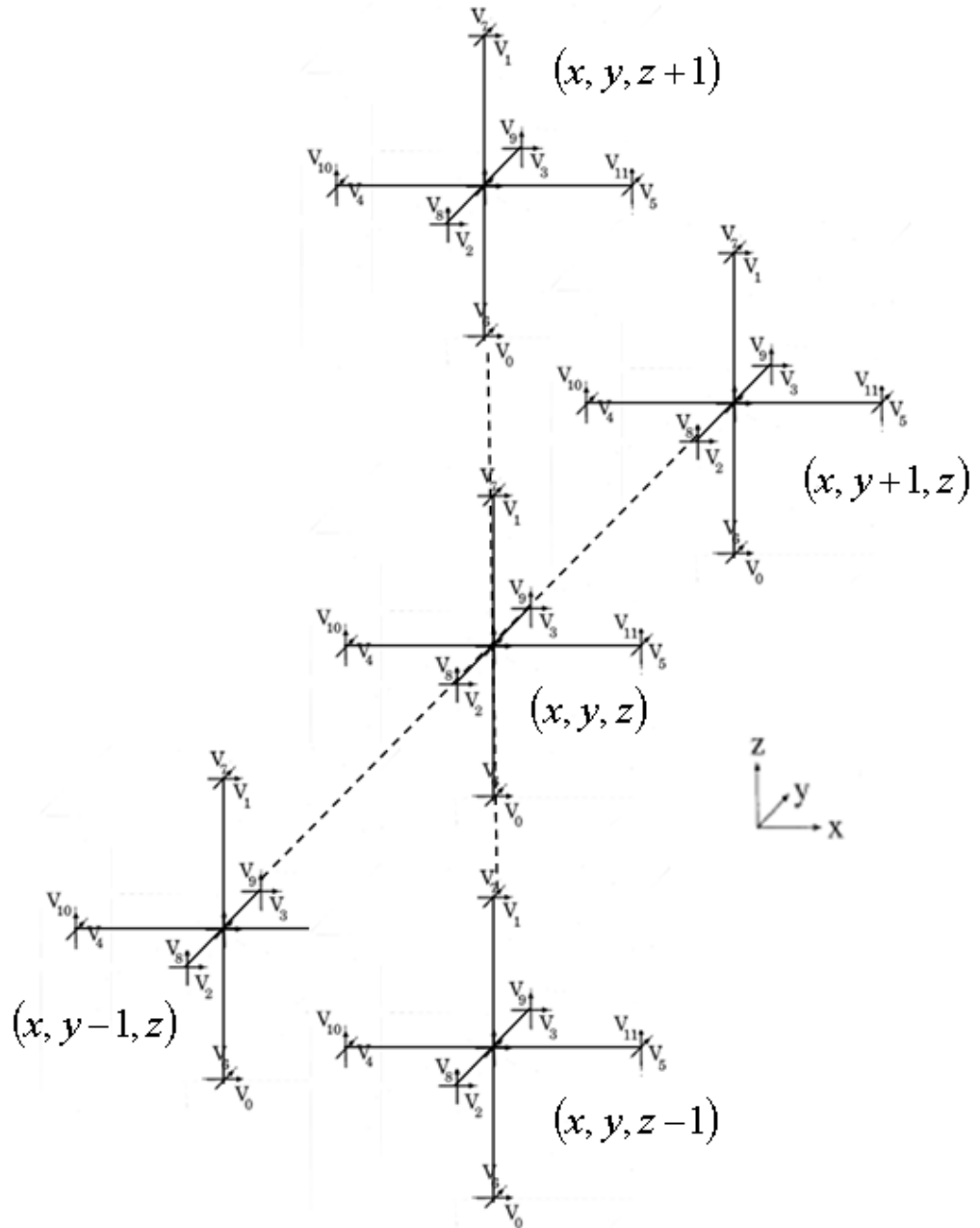Consequently, the incident voltages at the neighbouring nodes can be obtained as given in (2.7).

Fig.2.3 A cluster of SCN nodes.

$$_{k+1}V_0^i(x, y, z+1) = {}_kV_1^r(x, y, z) = -0.5 \tag{2.7a}$$

$$_{k+1}V_1^i(x, y, z-1) = {}_kV_0^r(x, y, z) = 0.5 \tag{2.7b}$$

$$_{k+1}V_8^i(x, y+1, z) = {}_kV_9^r(x, y, z) = 0.5 \tag{2.7c}$$

$$_{k+1}V_9^i(x, y-1, z) = {}_kV_8^r(x, y, z) = 0.5 \tag{2.7d}$$

The new incident voltages in (2.7) are then scattered into other ports of these nodes to obtain the scattered voltages that propagating into the neighbouring nodes at the next time-step $k+2$.

Equation (2.7) also implies that it takes two time-steps for a wave to propagate the distance of a block of space or the distance between two adjacent nodes Δl. Thus, the velocity within 3D-SCN, v, is [2.1]

$$v = \frac{\Delta l}{2\Delta t} \tag{2.8}$$

where Δt is the time discretisation.

2.2.2 Modeling of the 3D-SCN Boundary

The boundary of the three-dimensional TLM model is a plane adjacent to the 3D-SCN as shown in Fig.2.4. If the boundary has an impedance value of Z_b, the new incident voltage on the port adjacent to this boundary will be

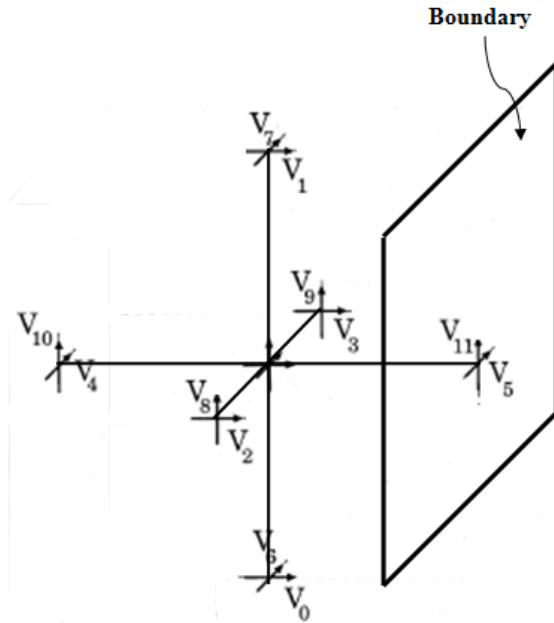$$_{k+1}V_n^i = \left(\frac{Z_b - Z}{Z_b + Z} \right)_k V_n^r \qquad (2.9)$$

Fig.2.4 A SCN adjacent to a boundary [2.7].

In general, there are three boundary conditions for the three-dimensional TLM model. They are the absorbing (matched) [2.8], the conducting (short-circuit) and the magnetic (open-circuit) boundary conditions. The new incident voltages on the port adjacent to these boundaries can be obtained as given in (2.10).

For absorbing boundary, $_{k+1}V_n^i = (0)_k V_n^r = 0$ (2.10a)

For open-circuit boundary, $_{k+1}V_n^i = (1)_k V_n^r =_k V_n^r$ (2.10b)

For conducting boundary, $_{k+1}V_n^i = (-1)_k V_n^r = -_k V_n^r$ (2.10c)

2.2.3 Calculating the field components from SCN mesh

In the SCN mesh, the electric and magnetic field components can be determined at any point from the $x-$, $y-$ and z-directed voltages (V_x, V_y, V_z) and currents (I_x, I_y, I_z) respectively. In general, they are calculated either at the node or in between nodes. The electric and magnetic field components at the node can be calculated as given in (2.11) and (2.12) respectively [2.1].

$$E_x = -\frac{V_x}{\Delta l} = -\frac{\left(\frac{1}{2}\left(V_0^i + V_1^i + V_2^i + V_3^i\right)\right)}{\Delta l} = -\frac{V_0^i + V_1^i + V_2^i + V_3^i}{2\Delta l}$$ (2.11a)

$$E_y = -\frac{V_y}{\Delta l} = -\frac{\left(\frac{1}{2}\left(V_4^i + V_5^i + V_6^i + V_7^i\right)\right)}{\Delta l} = -\frac{V_4^i + V_5^i + V_6^i + V_7^i}{2\Delta l}$$ (2.11b)

$$E_z = -\frac{V_z}{\Delta l} = -\frac{\left(\frac{1}{2}\left(V_8^i + V_9^i + V_{10}^i + V_{11}^i\right)\right)}{\Delta l} = -\frac{V_8^i + V_9^i + V_{10}^i + V_{11}^i}{2\Delta l}$$ (2.11c)

$$H_x = \frac{I_x}{\Delta x} = \frac{-V_6^i + V_7^i + V_8^i - V_9^i}{2Z\Delta l}$$ 2.12a)

$$H_y = \frac{I_y}{\Delta y} = \frac{-V_{10}^i + V_{11}^i + V_0^i - V_1^i}{2Z\Delta l} \qquad (2.12b)$$

$$H_z = \frac{I_z}{\Delta z} = \frac{-V_2^i + V_3^i + V_4^i - V_5^i}{2Z\Delta l} \qquad (2.12c)$$

Similarly, the electric and magnetic field components placed between nodes can be calculated. For instance, the E_z and H_y components in between nodes (x, y, z) and $(x+1, y, z)$ in Fig. 2.3 can be calculated as given in (2.13) and (2.14) respectively.

$$E_z = -\frac{\left(V_{11}^i + V_{10}^i\right)}{\Delta z} \qquad (2.13)$$

$$H_y = \frac{V_{10}^i - V_{11}^i}{Z_0 \Delta y} \qquad (2.14)$$

where $Z_0 = \sqrt{\mu_0/\varepsilon_0} = \sqrt{L/C}$ [2.9] is the impedance of the transmission-line and Z_0 is equal to 377Ω for the model of free space.

The calculations of electric current and charge are not covered here but can be found in Ref. [2.1].

2.2.4 Computational procedure in a SCN mesh

The first step in the computational procedure of the three-dimensional SCN mesh is the assignment of initial conditions such as the input excitations, the time step, the size of nodes and the boundary conditions. Then, the scattered voltages at each node are determined from the scattering matrix (S) related to the incident voltages (V^i) as given in (2.1). At the next time step, the new incident voltages are obtained from the neighbouring nodes as described in section 2.2.1 during the connection process. In addition, the new incident voltages are calculated from the scattered voltages at the same node, within those nodes adjacent to the boundary as explained in section 2.2.2 during the connection process. Moreover, the outputs—all electromagnetic quantities—can be determined and calculated at any simulation stage. The complete computation procedure for the three-dimensional SCN mesh can be summarised in a schematic diagram as shown in Fig. 2.5.
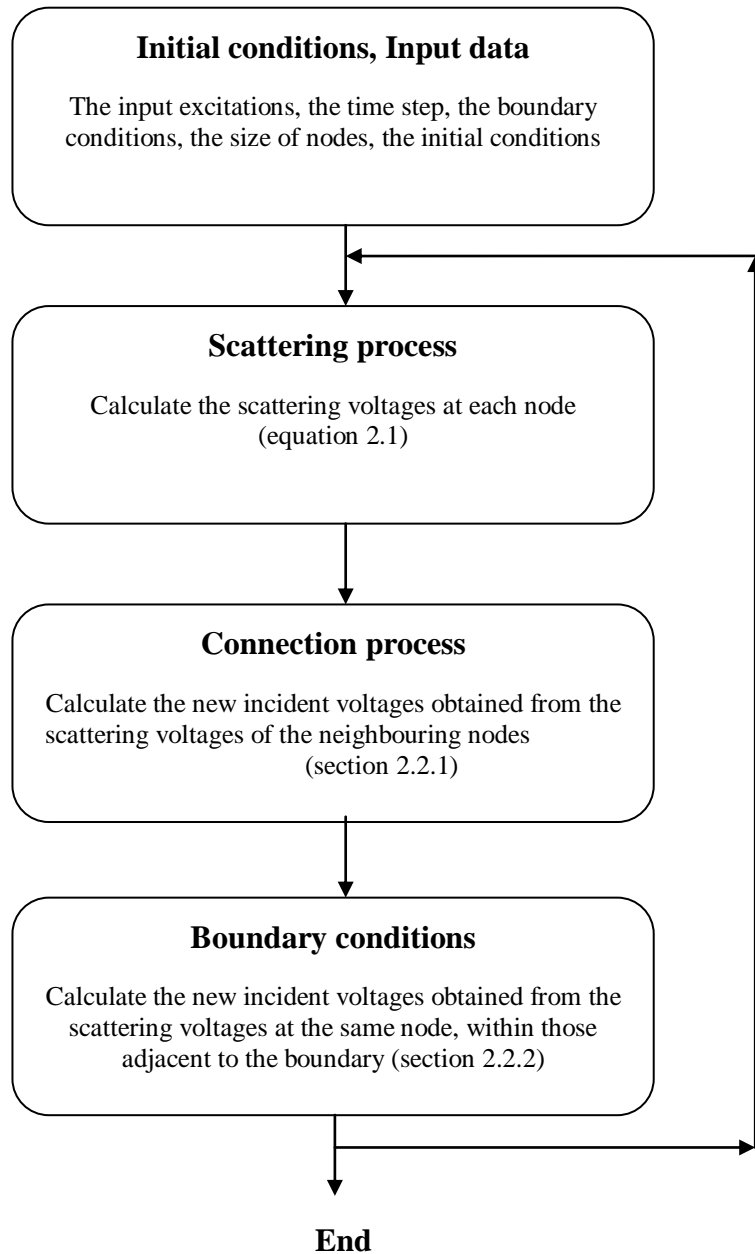
```
┌─────────────────────────────────────────┐
│       Initial conditions, Input data     │
│                                           │
│  The input excitations, the time step,    │
│  the boundary conditions, the size of     │
│  nodes, the initial conditions            │
└─────────────────────────────────────────┘
                     │
                     ▼
┌─────────────────────────────────────────┐
│            Scattering process             │
│                                           │
│  Calculate the scattering voltages at     │
│  each node (equation 2.1)                 │
└─────────────────────────────────────────┘
                     │
                     ▼
┌─────────────────────────────────────────┐
│           Connection process              │
│                                           │
│  Calculate the new incident voltages      │
│  obtained from the scattering voltages    │
│  of the neighbouring nodes                │
│  (section 2.2.1)                          │
└─────────────────────────────────────────┘
                     │
                     ▼
┌─────────────────────────────────────────┐
│           Boundary conditions             │
│                                           │
│  Calculate the new incident voltages      │
│  obtained from the scattering voltages    │
│  at the same node, within those           │
│  adjacent to the boundary (section 2.2.2) │
└─────────────────────────────────────────┘
                     │
                     ▼
                    End
```

Initial conditions, Input data

The input excitations, the time step, the boundary conditions, the size of nodes, the initial conditions

Scattering process

Calculate the scattering voltages at each node (equation 2.1)

Connection process

Calculate the new incident voltages obtained from the scattering voltages of the neighbouring nodes (section 2.2.1)

Boundary conditions

Calculate the new incident voltages obtained from the scattering voltages at the same node, within those adjacent to the boundary (section 2.2.2)

End

Fig.2.5 Schematic diagram of the computation procedure for the SCN mesh.

2.3   Modelling of the SCN with loaded stubs

The use of stubs is required to model fine features and non-uniform materials such as dielectric, magnetic and lossy materials. The node with stubs can be constructed by adding six extra ports, stub-ports 12, 13, 14, 15, 16 and 17, to the SCN. As a result, the scattering matrix now has a size of 18x18. But, the ports 0-11 are still connected to the neighbouring nodes as in the regular SCN. The stub-ports are used in the calculation of the electric and magnetic fields. In addition, the stub-ports 12, 13 and 14 are open-circuited, adding capacitance to the node. These ports are referred to as *capacitive stubs*. On the other hand, the stub-ports 15, 16 and 17 are short-circuited, adding inductance to the node. These ports are referred to as *inductive stubs*.

Suppose that $\hat{Y}_x$ is the characteristic admittance of the x-directional capacitance stub normalized to the characteristic admittance of free space (Y_0), which is [2.1]

$$\hat{Y}_x = \frac{2\varepsilon_r}{u_0 \Delta t}\left(\frac{\Delta y \Delta z}{\Delta x}\right) - 4 \qquad (2.15a)$$

where $u_0 = \dfrac{1}{\sqrt{\mu_0 \varepsilon_0}}$.

Similarly, the y-directional and z-directional capacitive stubs are

$$\hat{Y}_y = \frac{2\varepsilon_r}{u_0 \Delta t}\left(\frac{\Delta x \Delta z}{\Delta y}\right) - 4 \qquad (2.15b)$$

$$\hat{Y}_z = \frac{2\varepsilon_z}{u_0 \Delta t}\left(\frac{\Delta x \Delta y}{\Delta z}\right) - 4 \qquad (2.15c)$$

Similarly, suppose that $\hat{Z}_x$ is the characteristic impedance of the x-directional inductive stub normalized to the characteristic impedance of free space (Z_0), which is

$$\hat{Z}_x = \frac{2\mu_r}{u_0 \Delta t}\left(\frac{\Delta y \Delta z}{\Delta x}\right) - 4 \qquad (2.16a)$$

Similarly, for the y-directional and z-directional inductive stubs are

$$\hat{Z}_y = \frac{2\mu_r}{u_0 \Delta t}\left(\frac{\Delta x \Delta z}{\Delta y}\right) - 4 \qquad (2.16b)$$

$$\hat{Z}_z = \frac{2\mu_r}{u_0 \Delta t}\left(\frac{\Delta x \Delta y}{\Delta z}\right) - 4 \qquad (2.16c)$$

The scattering matrix of the SCN with loaded stubs can now be obtained as given in (2.17)

S=

	0	1	2	3	4	5	6	7	8	9	10	11	12	13	14	15	16	17
0	a	c	b	b							d	-d	g				-i	
1	c	a	b	b							-d	d	g				i	
2	b	b	a	c	d	-d							g					i
3	b	b	c	a	-d	d							g					-i
4			d	-d	a	c	b	b						g				-i
5			-d	d	c	a	b	b						g				i
6					b	b	a	c	d	-d				g		i		
7					b	b	c	a	-d	d				g		-i		
8							d	-d	a	c	b	b			g	-i		
9							-d	d	a	a	b	b			g	i		
10	d	-d							b	b	a	c			g		i	
11	-d	d							b	b	c	a			g		-i	
12	e	e	e	e									h					
13					e	e	e	e						h				
14									e	e	e	e			h			
15							f	-f	-f	f						j		
16	-f	f									f	-f					j	
17			f	-f	-f	f												j

$$(2.17)$$

where

$$a = \frac{-\hat{Y}}{2\left(4+\hat{Y}\right)} + \frac{\hat{Z}}{2\left(4+\hat{Z}\right)} \qquad (2.18a)$$

$$b = \frac{4}{2\left(4+\hat{Y}\right)} \qquad (2.18b)$$

$$c = \frac{-\hat{Y}}{2\left(4+\hat{Y}\right)} - \frac{\hat{Z}}{2\left(4+\hat{Z}\right)} \qquad (2.18c)$$

$$d = \frac{4}{2\left(4+\hat{Z}\right)} \qquad (2.18d)$$

$$e = b \qquad (2.18e)$$

$$f = \hat{Z}d \qquad (2.18f)$$

$$g = \hat{Y}b \qquad (2.18g)$$

$$h = \frac{\hat{Y}-4}{\hat{Y}+4} \qquad (2.18h)$$

$$i = d \qquad (2.18i)$$

$$j = \frac{4-\hat{Z}}{4+\hat{Z}} \qquad (2.18j)$$

Note that $\hat{Y}$ and $\hat{Z}$ in (2.18) refer to the corresponding directional stubs appropriately. In addition, they must correspond to real positive component values to maintain the stability. Further details on the SCN with loaded-stubs can be found in Ref. [2.1] and [2.7].

In the computational procedure of the three-dimensional TLM model, the scattering process of the SCN nodes with loaded-stubs occurs between the scattering process of the regular SCN nodes and the connection process. This can be simply summarized in a schematic diagram as shown in Fig. 2.6.

The SCN with capacitive, inductive and Lossy stubs [2.1] are not explained here as all modeling in the project is done in the presence of the SCN with loaded-stubs.

2.4   Example TLM simulation

In order to demonstrate the accuracy of the simulation program created for the project, this section presents a comparison between the three-dimensional SCN stub loaded model simulation and the analytical result for the structure shown in Fig.2.7.

The model in Fig.2.7 is a 3 mm x 5 mm x 10 mm (thickness x width x height) silicon block placed in a problem space of 801 mm x 5 mm x 10 mm, with a space step Δl of 1 mm. The boundary conditions at the extremities of the problem space are such that it is matched at Xmin-Xmax, open-circuited at Ymin-Ymax and conducting at the top and the bottom (Zmin-Zmax). In addition, the dielectric block has a relative permittivity ε_r of 16 at room temperature.
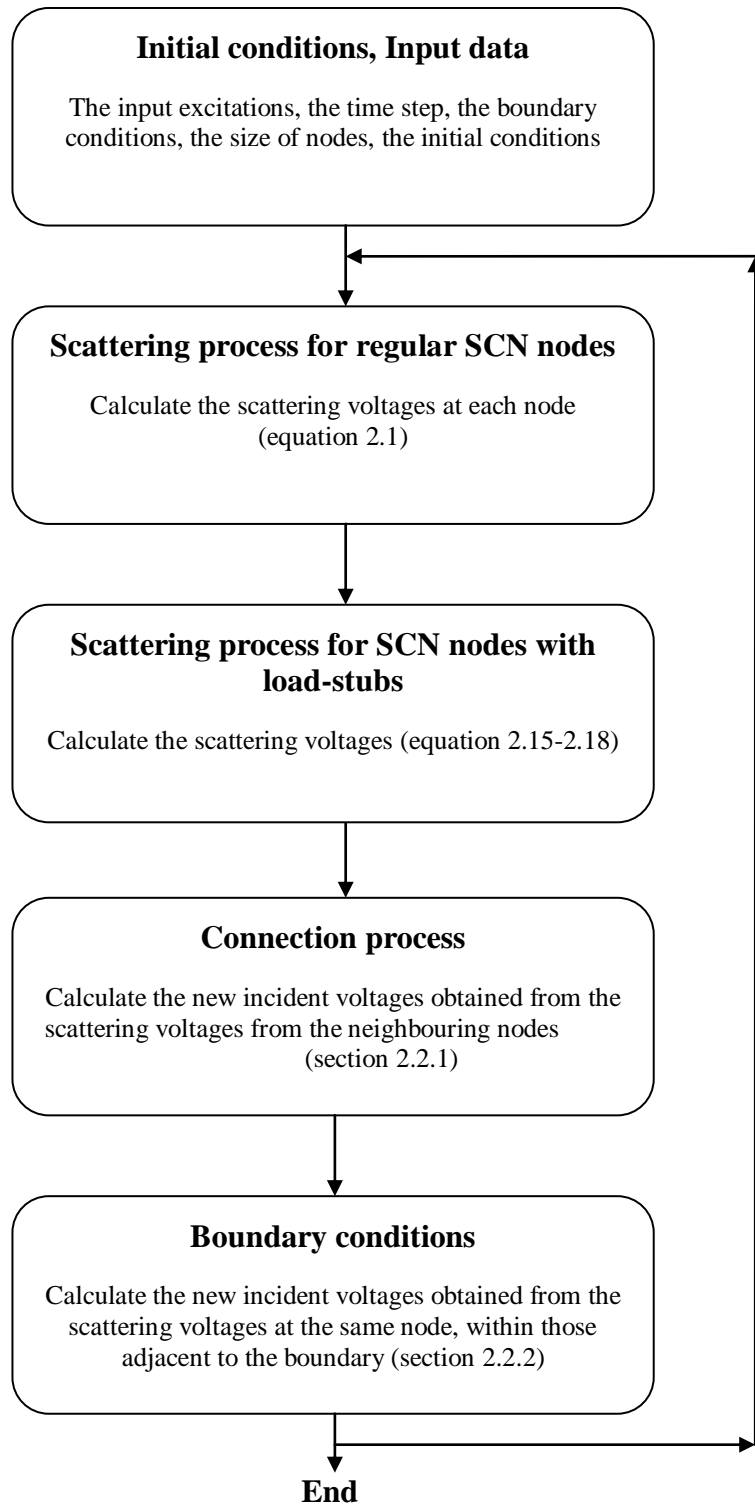
Fig.2.6 Schematic diagram of computation procedure for the SCN mesh with load-stubs.
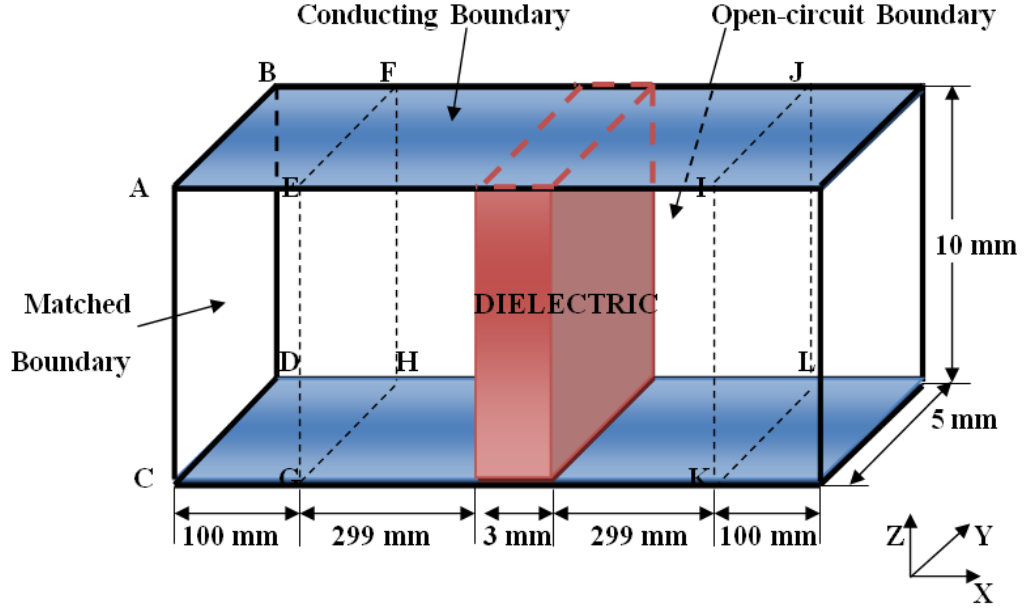
Fig.2.7 The model of the three-dimensional SCN mesh with dielectric block.

The simulation results for the model in Fig.2.7 in the time-domain were obtained by exciting a Gaussian pulse shaped input voltage (V_{in}) of 1 V peak amplitude and 85 ns temporal half-width in the Z-direction on the **ABCD** plane as defined by equation (2.19). Its propagation will be in the X-direction. The time-domain reflected and transmitted voltages (output) are obtained by observing the voltage at **EFGH** and **IJKL** planes as given in equations (2.20) and (2.21) respectively.

$$V_{in} = \frac{\sum\limits_{y=0}^{y=NY} \sum\limits_{z=0}^{z=NZ} {}_{k}V_{10}^{i}(0, y, z)}{NY} \tag{2.19}$$

$$V_{out\_plane\_EFGH} = \frac{\sum\limits_{y=0}^{y=NY} \sum\limits_{z=0}^{z=NZ} \left({}_{k}V_{10}^{i}(100, y, z) + {}_{k}V_{11}^{i}(99, y, z) \right)}{NY} \tag{2.20}$$

$$V_{out\_plane\_IJKL} = \frac{\sum\limits_{y=0}^{y=NY} \sum\limits_{z=0}^{z=NZ} \left({}_{k}V_{10}^{i}(701, y, z) + {}_{k}V_{11}^{i}(700, y, z) \right)}{NY} \tag{2.21}$$

where NY and NZ are the number of nodes in Y and Z –directions.

The output voltages on **EFGH** and **IJKL** planes are shown in Fig.2.8 and 2.9 respectively.
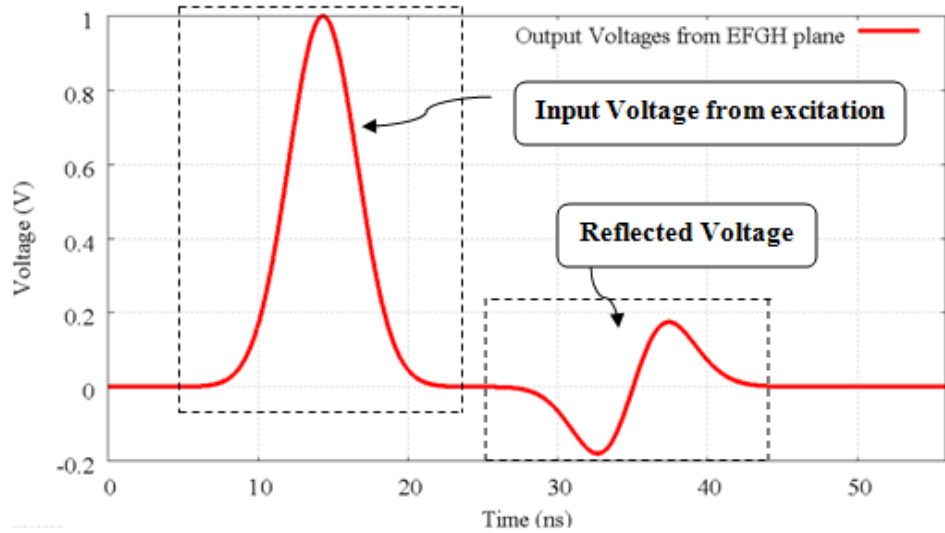
Fig.2.8 The time-domain results observed from EFGH plane, where the first pulse with magnitude of 1 V at time between 7-22 ns approximately, is the input voltage. And the second pulse at time between 26-45 ns is a reflected voltage with amplitude of 0.18 V approximately.
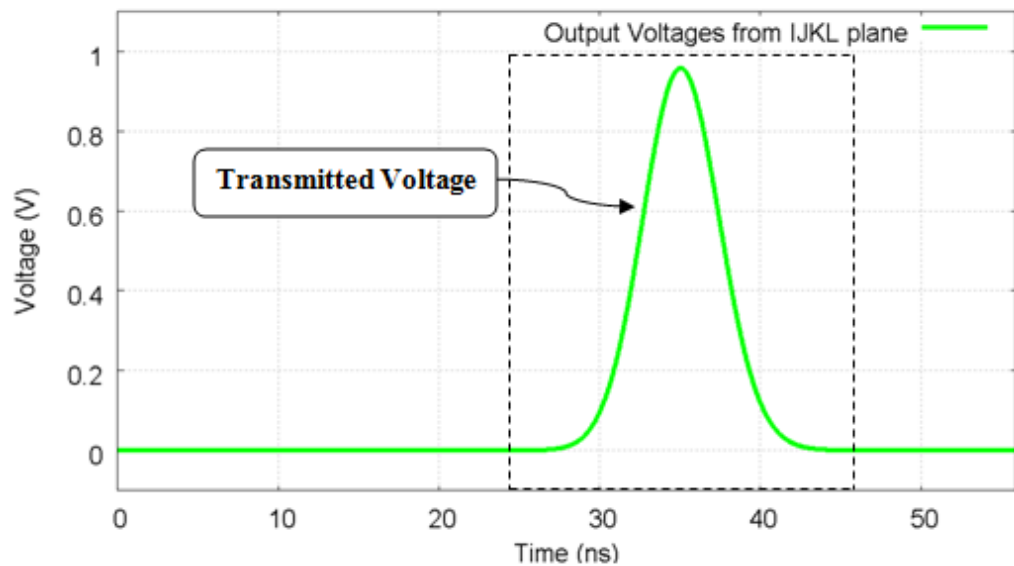
Fig.2.9 The time-domain results observed from IJKL plane where the voltage pulse between 26-45 ns is a transmitted voltage with magnitude of 0.95 V approximately.

The time-domain reflected and transmitted voltages in Fig.2.8 and 2.9 can be transformed into the discrete frequency-domain results—the reflection and transmission coefficients (S11 and S21)—by applying the Fast Fourier Transform (FFT). These frequency-domain results are compared with the analytical results, which are simply calculated by employing Fresnel's reflection formulae [2.10]-[2.11] which is summarised in (2.22)-(2.23) for the comparisons as shown in Fig. 2.10 and 2.11.

$$R = \frac{1 - \exp(-j2\delta)}{1 - R'^2 \exp(-j2\delta)} R' \tag{2.22}$$

$$T = \frac{(1 - R'^2)\exp\{-j(\delta - k_0 d)\}}{1 - R'^2 \exp(-j2\delta)} \tag{2.23}$$

where $\delta = \frac{2\pi d}{\lambda}\sqrt{m^2 - \sin^2\theta}$, $k_0 = \frac{2\pi}{\lambda}$, d is the thickness of the sample, λ is the wave-length in the free space, n is the complex refractive index of the sample, θ is the angle of the incident wave and R' is given in (2.24).

$$R' = \frac{\cos\theta - \sqrt{n^2 - \sin^2\theta}}{\cos\theta + \sqrt{n^2 - \sin^2\theta}} \tag{2.24}$$

For the model in Fig.2.7, d, n and θ are 3 mm, 4 and 0 respectively.
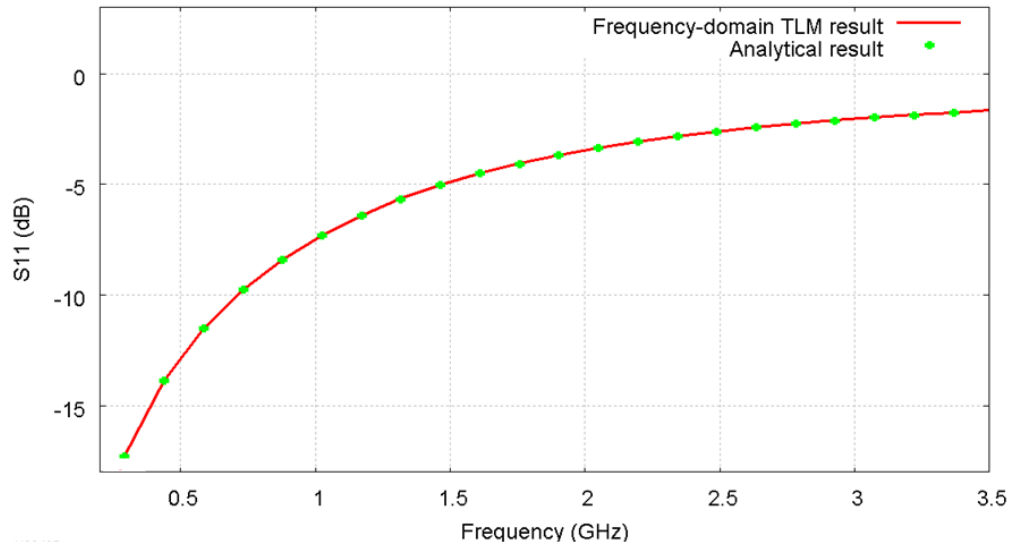
Fig.2.10 The diagram shows the comparison between the discrete frequency-domain reflected voltage (red line) obtained by applying FFT from the time-domain reflected voltage in Fig. 2.8 and the analytical result (green dots) between 0-3.5 GHz.
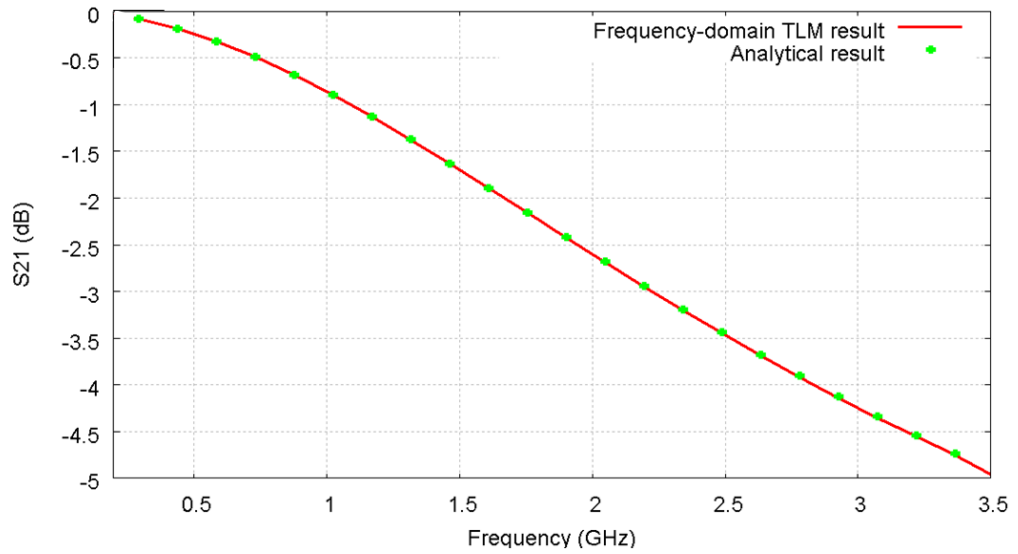
Fig.2.11 The diagram shows the comparison between the discrete frequency-domain transmitted voltage (red line) obtained by applying FFT from the time-domain transmitted voltage in Fig. 2.9 and the analytical result (green dots) between 0-3.5 GHz.

Fig.2.10 and 2.11 shows good agreement between the TLM simulation and the analytical results.

2.5 The errors and limitations in three-dimensional TLM method

There are a variety of errors that occur in three-dimensional TLM simulations. Therefore, the TLM method must be used with caution in order to obtain results of a required accuracy. The main sources of errors [2.12] include (i) the coarseness (ii) the velocity errors and (iii) the misalignment of boundaries and dielectric interfaces in inhomogeneous structures. These errors and some techniques used to minimise them are explained below.

2.5.1 Coarseness Error

The coarseness error occurs when the size of the TLM nodes used in the TLM mesh simulation is larger than the geometric features; for instance, in case of planar structures containing such regions. This error can be simply minimised by using a network with a very fine mesh instead. Nevertheless, this results in high computational costs such as large memory requirements and can be very time consuming to compute. A better solution is to apply a network with variable mesh size to obtain more accurate results [2.13]-[2.14]. Another approach proposed by Shih and Hoefer [2.15] is to use the coarse meshes with different Δl to calculate the structural response multiple times. Then, the obtained results are extrapolated to $\Delta l = 0$. Consequently, the coarseness error may be minimised.

2.5.2 Velocity error

In a TLM mesh, the propagation velocity depends on the direction of the propagation and on the frequency at which the wavelength (λ) is small compared to the mesh size Δl. In addition, when λ is large compared to Δl, it is known that the fields can propagate with the same velocity in all directions [2.1]. Typically the mesh size Δl must be smaller than a tenth of the smallest wavelength of interest. In other words, the three dimensional TLM requires the spatial sampling or space-step Δl to be at least as fine as $\lambda/10$. Consequently, the propagation in the TLM mesh can be considered as non-dispersive.

The general dispersion of the three-dimensional TLM node is given in (2.25) [2.16]

$$\det\left(PS - e^{jk_0 \Delta l} I\right) = 0 \qquad (2.25)$$

where I is the identity matrix, k_0 is the propagation constant along the transmission lines. S is a scattering matrix and P is a connection matrix which contains the plane wave propagation constants.

The dispersion of velocity of waves relative to the propagation in the TLM mesh is shown in Fig. 2.12
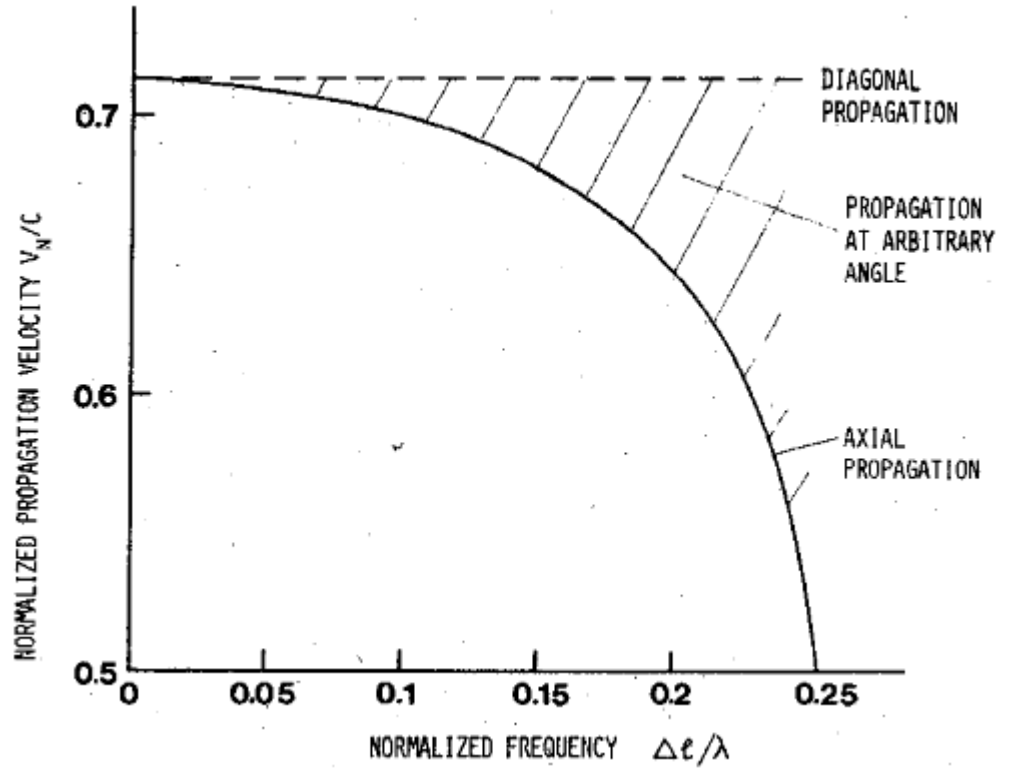
Fig. 2.12 The dispersion of the velocity of waves in the TLM mesh [2.17].

The propagation properties of the three-dimensional TLM node at 45° can be found from the distance travelled, which is $\sqrt{2}(\Delta l/2)$ and the velocity of propagation in the model u_{TLM} obtained as given in (2.26).

$$u_{TLM} = \frac{u_{TL}}{\sqrt{2}} = \frac{1}{\sqrt{2}}\left(\frac{\sqrt{2}\Delta l}{2\Delta t}\right) = \frac{\Delta l}{2\Delta t} \tag{2.26}$$

where u_{TL} is the velocity of propagation on each line.

More detail on the dispersion properties of the three-dimensional SCN without stub-loading can be found in [2.17] and [2.18] whereas for the SCN with stub-loading can be found in [2.19].

The velocity error can be prevented by selecting a suitable value for the mesh size and using equation (2.26) for the propagation without dispersion. This error can be also be eliminated by employing the same solutions discussed under the coarseness error in section 2.5.1.

2.5.3 Misalignment of boundaries and dielectric interfaces in inhomogeneous structures
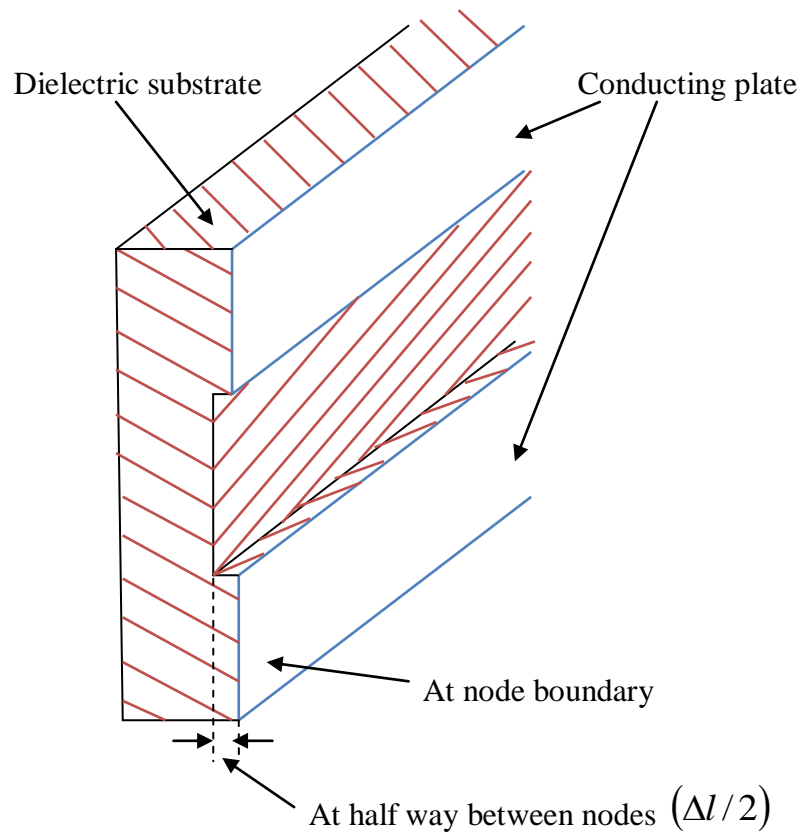
Fig.2.13 The misalignment of dielectric interfaces and conducting boundaries in the three-dimensional TLM model of a planar structure [2.17].

Some three-dimensional inhomogeneous structures such as microstrips, may have a dielectric interface located halfway between nodes $(\Delta l / 2)$ while the conducting boundaries are located across nodes as illustrated in Fig.2.13. The three-dimensional TLM method cannot be used directly to model it because the boundaries can be located either in between nodes or at the surface of nodes. One method to solve this problem is to employ a three-dimensional TLM method with an alternating node configuration as proposed by Saguet and Pic [2.20]. Another method proposed by M. Panitz [2.21] allows the placement of boundaries at non-integer space-steps places without compromising the time-step of the simulation. The advantage of this method is that it does not introduce a significant error to the simulation.

2.6 Conclusion

The three-dimensional TLM method has been introduced and the details of the three-dimensional SCN were given in this chapter. The computation procedure for the three-dimensional SCN mesh was explained and summarised in a schematic diagram. Moreover, the usage of loaded-stubs in modelling material permittivity and permeability in the SCN was shown. The demonstration of the SCN loaded-stubs in three-dimensional TLM model showed that the three-dimensional TLM program developed for the project provides acceptable when accuracy compared to an analytical result. In addition, the simulation errors and mitigation of these errors in the three-dimensional TLM method were discussed.

2.7   References

[2.1]   C. Christopoulos, The Transmission-Line Modeling Method: TLM. New York: IEEE Press, 1995.

[2.2]   S. Akhtarzad and P. B. Johns, "The solution of Maxwell's equations in three space dimensions and time by the TLM method of numerical analysis," *Proc. Inst. Elec. Eng.*, vol. 122, no. 12, pp. 1344–1348, Dec. 1975.

[2.3]   E.C. Jordan, and K.G. Balmain. Electromagnetic Waves and Radiating Systems, 2nd ed. Englewood Cliffs, NJ: Prentice Hall, pp. 513-519, 1996.

[2.4]   P. Saguet ~d E. Pie, "Utilisation d'un nouveau type de noeud clans la method TLM en 3 dimensions," *Electron. Lett.,* vol. 18, no. 11, pp. 478-480, May 1982.

[2.5]   A. Amer, "The condensed node TLM method and its application to transmission in power system," Ph.D. thesis, Nottingham University, 1980, May 1982.

[2.6]   P. B. Johns, "New symmetrical condensed node for three-dimensional solution of electromagnetic wave problems by TLM," *Electron. Lett.*, vol. 22, pp. 162-164, 1986.

[2.7]   P. B. Johns, "A Symmetrical Condensed Node for the TLM Method,"
         IEEE Trans. Microwave Theory Tech., vol. 35, no. 4, pp. 370-377, Apr.
         1987.

[2.8]   J. A. Morente, J. A. Porte, and M. Khalladi, "Absorbing boundary
         conditions for the TLM method," *IEEE Trans. Microwave Theory
         Tech*..vol. 40, no. 11, pp. 2095-2099, 1992.

[2.9]   R. Ludwig and P. Bretchko, *RF Circuit Design Theory and
         Applications*. Prentice-Hall, Upper Saddle River, NJ, 2000.

[2.10]   K. Sato, H. Kozima, H. Masuzawa, T. Manabe, T. Ihara, Y. Kasashima,
         K. Yamaki, T. Tanaka, "Measurements of Reflection Characteristics
         and Refractive Indices of Interior Construction Materials in Millimeter-
         Wave Bands," *in Proc. 45th IEEE Veh. Technol*., vol. 1, pp. 449-453,
         Jul. 1995.

[2.11]   A. Ishimaru, "Electromagnetic Wave Propagation, Radiation, and
         Scattering", Chap. 3, Prentice-Hall, Englewood Cliffs, NJ, 1991.

[2.12]   Wolfgang J. R. Hoefer, "The Transmission-Line Matrix Method-
         Theory and Applications," *IEEE Trans. Microwave Theory Tech*..vol.
         33, no. 10, pp. 882-893, Oct. 1992.

[2.13]   D.A. A1-Mukhtar and J. E. Sitch, "Transmission-line matrix method
         with irregularly graded space*," Proc. Insr. Elec. Eng*., vol. 128, no. 6,
         pp. 299–305, Dec. 1981.

[2.14]   D. A1-Mnkhtar, "A transmission line matrix with irregularly graded space," Ph.D. thesis, Univ. of Sheffield, England, Aug. 1980.

[2.15]   Y.-C. Shih and W. J. R. Hoefer, "Dominant and second-order mode cutoff frequencies in fin lines calculated with a two-dimensional TLM program," *IEEE Trans. Microwave Theory Tech.*, vol. 28, pp. 1443–1448, Dec. 1980.

[2.16]   J. Nielsen, W. Hoefer, "A complete dispersion analysis of the condensed node TLM mesh," *IEEE Trans. On Magnetics*, vol. 27, no. 5, pp. 3982-3983, Sep 1991.

[2.17]   P. B. Johns and R. L. Beurle, "Numerical solution of 2-dimensional scattering problems using a transmission-line matrix," *Proc. Inst. Elec. Eng.*, vol 118, no. 9, pp. 1203-1208, Sept. 1971.

[2.18]   P. Saguet and E. Pic, "Utilisation d'un nouveau type de noeud dans la methode TLM en 3 dimensions," *Electron. Lett.*, vol. 18, no. 11, pp. 478-480, May 1982.

[2.19]   M. Celuch-Marcysiak, and W.K. Gwarek, "On the effect of 3 bilateral dispersion in inhomogeneous symmetrical condensed node modeling", *IEEE Trans.*, vol. 42, (6), pp. 1069-1073, 1994.

[2.20]   P. Saguet and E. Pic, " Le maillage rectangulaire et le changement de maille dans la methode TLM en deux dimensions*," Electron. Lett.*, vol. 17, no. 7, pp. 277–278, Apr. 2, 1981.

[2.21] M. Panitz, J. Pual and C. Christopoulos. *"A fractional Boundary Placement Model Using the Transmission-Line Modeling (TLM) Method,"* *IEEE Trans. Microwave Theory Tech*., vol. 57, no. 3, pp. 637-646, 2009.

3. Digital Filtering Techniques with Three-Dimensional TLM Models

This chapter presents a technique based on digital filters (DF) to represent fine features in time-domain TLM simulations. It begins by introducing DF techniques for time-domain numerical simulation methods, e.g., finite-difference time-domain (FDTD) and TLM. Then, the Fast Fourier Transform (FFT), the frequency-domain Prony method and the Bilinear-Z-transform employed to estimate the DF parameters are described. Finally, this technique is demonstrated with an example of SCN loaded-stubs in this chapter.

3.1 Introduction to the DF techniques

Fine features such as thin panels, wires and complex materials with frequency dependent properties [3.1]-[3.3] require significant resources and high computational costs in a time-domain simulation. The straightforward method to describe and implement fine features in full-field solutions of electromagnetic problems such as FDTD [3.4]-[3.5] and TLM is to use a very fine mesh to adequately capture every detail of the fine features. As a result, unavoidably high computing costs are required to run the simulation. For

example, in the case of wires, the size of the TLM nodes must be significantly smaller than the diameter of the wire. Therefore, the DF technique has been developed in order to solve these problems. It has also been successfully applied to represent thin panels as given in Ref. [3.6].

The techniques used to create a DF to represent a fine feature are the Fast Fourier Transform (FFT), the frequency-domain Prony method [3.7]-[3.8] and the Bilinear-Z-transform. These techniques are employed to extract the DF parameters from the scattering data of the fine feature given in frequency-domain. The frequency-domain Prony method and the bilinear Z-transform are applied to obtain the discrete time-domain functions referred to as the DF functions are obtained. Finally, they are employed in the three-dimensional TLM mesh at the surface between nodes to represent the properties of the fine feature. The complete procedures and the related equations are described in sections 3.2 and 3.3.

3.2   Extraction of DF parameters for the fine feature

As mentioned in the previous section, the DF parameters are obtained from the scattering data of the fine feature in frequency-domain. This data can be obtained by experimental, analytical or simulation results. In addition, they may also be obtained by using an FFT to transform the discrete time-domain data to the discrete frequency-domain data. An example usage of the FFT is shown in section 3.4.

Suppose that a fine feature has a two-port scattering matrix as given in (3.1).

$$S_f(\omega) = \begin{bmatrix} R(\omega) & T(\omega) \\ T(\omega) & R(\omega) \end{bmatrix}$$
(3.1)

where $R(\omega)$ and $T(\omega)$ are the frequency-dependent reflection and transmission coefficients respectively.

Consider $R(\omega)$ and $T(\omega)$ as a frequency-dependent complex coefficient $F(s)$, which can be written in a standard Pade form as shown in (3.2).

$$F(s) = \frac{\sum\limits_{i=0}^{NP} b_i s^i}{\sum\limits_{i=0}^{NP} a_i s^i} \tag{3.2}$$

where a_i and b_i are unknown coefficients, NP is the number of poles, and s^i is the complex frequency of the ith pole.

The frequency-domain Prony method is employed to find the unknown coefficients a_i and b_i in (3.2) from a set of NS measurements of F as given in (3.3). These unknown coefficients can be obtained from (3.4) [3.6].

$$\{F(\omega_0), F(\omega_1), \ldots\ldots F(\omega_{NS-2}), F(\omega_{NS-1})\} \tag{3.3}$$

$$\begin{bmatrix} a_0 \\ a_1 \\ \vdots \\ a_{NP-1} \\ b_0 \\ b_1 \\ \vdots \\ b_{NP-1} \end{bmatrix} = -\Re\left[\underline{H}^T.\underline{H}\right]^{-1}.\Re\left[\underline{H}^T.\underline{R}\right] \tag{3.4}$$

where $\Re$ is the real part and T indicates the transpose. $\underline{H}$ and $\underline{R}$ are matrices as shown in (3.5)-(3.7).

Note that the value of NP is selected depending on the type of the transient and that the selection of NP affects the accuracy of the results.

The matrix $\underline{H} = \lfloor H_0 | H_1 \rfloor$ where

$$H_0 = \begin{bmatrix} F_0 & (j\omega_0)F_0 & \cdots & (j\omega_0)^{NP-1}F_0 \\ F_1 & (j\omega_1)F_1 & \cdots & (j\omega_1)^{NP-1}F_1 \\ \vdots & \vdots & & \vdots \\ F_{NS-1} & (j\omega_{NS-1})F_{NS-1} & \cdots & (j\omega_{NS-1})^{NP-1}F_{NS-1} \end{bmatrix} \tag{3.5}$$

$$\underline{H_1} = \begin{bmatrix} -1 & -j\omega_0 & \cdots & -(j\omega_0)^{NP} \\ -1 & -j\omega_1 & \cdots & -(j\omega_1)^{NP} \\ \vdots & \vdots & & \vdots \\ -1 & -j\omega_{NS-1} & \cdots & -(j\omega_{NS-1})^{NP} \end{bmatrix} \tag{3.6}$$

and

$$\underline{R} = \begin{bmatrix} (j\omega_0)^{NP}F_0 \\ (j\omega_1)^{NP}F_1 \\ \vdots \\ (j\omega_{NS-1})^{NP}F_{NS-1} \end{bmatrix} \tag{3.7}$$

After the unknown coefficients a_i and b_i are obtained from (3.4), $F(s)$ in (3.2) can be transformed by using Laguerre's method [3.9]-[3.11] to put it into the form

$$F(s) = \frac{b_{NP}(s - s_{z0})(s - s_{z1})\cdots(s - s_{z(NP-1)})}{(s - s_{p0})(s - s_{p1})\cdots(s - s_{p(NP-1)})} \tag{3.8}$$

where s_{z_0} and s_{p_0} are the zeros and poles.

$F(s)$ in (3.2) may be converted into the discrete time-domain by using the bilinear Z-transform as given in (3.9).

$$s \xrightarrow{\quad z \quad} \frac{2}{\Delta t} \cdot \left(\frac{1 - z^{-1}}{1 + z^{-1}} \right) \qquad (3.9)$$

where Δt is the time discretisation which can be obtained from (2.8) for three-dimensional TLM.

After some manipulation, $F(s)$ in (3.8) can be written in the form

$$F(z) = B_0 \prod_{i=0}^{NP-1} \left[\frac{1 - z^{-1} \beta_{zi}}{1 - z^{-1} \beta_{pi}} \right] \qquad (3.10)$$

where

$$B_0 = b_{NP} \prod_{i=0}^{NP-1} \left[\frac{\alpha_{zi}}{\alpha_{pi}} \right] \qquad (3.11a)$$

$$\alpha_{zi} = \frac{2 - s_{zi}\Delta t}{\Delta t} \qquad (3.11b)$$

$$\beta_{zi} = \frac{2 + s_{zi}\Delta t}{2 - s_{zi}\Delta t} \qquad (3.11c)$$

$$\alpha_{pi} = \frac{2 - s_{pi}\Delta t}{\Delta t} \qquad (3.11e)$$

$$\beta_{pi} = \frac{2 + s_{pi}\Delta t}{2 - s_{pi}\Delta t} \qquad (3.11f)$$

Equation (3.10) may be expanded into partial fractions as given in (3.12).

$$F(z) = B_0 + \frac{\sum_{i=1}^{NP} B'_i z^{-i}}{1 + \sum_{i=1}^{NP} A_i z^{-i}} \qquad (3.12)$$

where $B'_i = B_i - B_0 A_i$

The complete derivation of formulae from (3.8) to (3.12) with an example of 3 poles is given in the Appendix.

$F(z)$ in (3.12) is the time-dependent complex coefficient. It will be employed as the DF in the three-dimensional TLM mesh as described in the next section.

3.3   The use of DF for three-dimensional TLM mesh

As mentioned, the digital filters (DFs) are placed at the surface between nodes in a three-dimensional TLM mesh to represent the properties of a fine feature. This also means that they are accounted as part of the "connection" process in TLM. In the other words, in the computational procedure of the three-dimensional TLM mesh with DFs, the DF functions are employed to calculate new incident voltage $\left(_{k+1}V_n^{\ i}\right)$ after the "connection" process of the regular SCN nodes and before the "boundary condition" process. This can be simply summarised in a schematic diagram as illustrated in Fig. 3.1.

Suppose that $F(z)$ in (3.12) is the reflection coefficient $R(z)$ at the surface between the three-dimensional TLM nodes. The relationship between $R(z)$ and TLM voltages is given by $R(z) = {}_{k+1}V^i(z)\big/{}_kV^r(z)$. Therefore, (3.12) can be expressed in the form

$$V^i = B_0\left(V^r\right) + \frac{\left(V^r\right)\sum_{i=1}^{NP}B'_i\,z^{-i}}{1+\sum_{i=1}^{NP}A_i z^{-i}} = B_0\left(V^r\right) + \sum_{i=1}^{NP}B'_i\,X_i \tag{3.13}$$

where X_i are the state variables of the system.

Initial conditions, Input data

The input excitations, the time steps, the boundary conditions, the size of nodes, the initial conditions

Scattering process

Calculate the scattering voltages at each node (equation 2.1)

Connection process for regular SCN nodes

Calculate the new incident voltages obtained by the scattering voltages from the neighbouring nodes (section 2.2.1)

Connection process for DFs

Calculate the new incident voltages obtained from DF functions with the scattering voltages from the neighbouring nodes (equation 3.13 or 3.14)

Boundary conditions

Calculate the new incident voltages obtained by the scattering voltages at the same node, within those adjacent to the boundary (section 2.2.2)

End

Fig.3.1 Schematic diagram of the computation procedure for the three-dimensional TLM mesh with DFs.

Equation (3.13) can be put into matrix form

$$V^i = B_0\left(V^r\right) + \underline{B}' \cdot \underline{X} \tag{3.14}$$

where

$$X = z^{-1} \underline{\underline{A}}' \cdot \underline{X} + z^{-1} \underline{1}' V^r \tag{3.15}$$

where

$$\underline{\underline{A}}' = \begin{bmatrix} -A_1 & -A_2 & -A_3 & \cdots & -A_{NP-1} & -A_{NP} \\ 1 & & & & & \\ & 1 & & & & \\ & & 1 & & & \\ & & & \ddots & & \\ & & & & 1 & \end{bmatrix} \tag{3.16a}$$

and

$$\underline{1}' = \begin{bmatrix} 1 & 0 & 0 & \cdots & 0 \end{bmatrix}^T \tag{3.16b}$$

Moreover, Equations (3.13) and (3.14) can be put in a compact form

$$V^i = DF\left(V^r\right) \tag{3.17}$$

where $DF(\ )$ is the DF transfer function.

Equation (3.17) can also be implemented as an internal boundary with no features present in the three-dimensional TLM mesh. The simulation example demonstrating the DF techniques applied to the three-dimensional load-stub model is presented in the next section.

3.4 Example of the DF techniques for the three-dimensional TLM mesh with load-stubs.

The section presents an example of the three-dimensional TLM mesh of a structure with dielectric material modelled with load-stubs as illustrated in Fig.3.2. It also shows how to extract the DF parameters from time-domain simulation results of a TLM model in Fig.3.2. The method of obtaining the frequency-dependent coefficients by using an FFT is presented. The comparisons of the results in time- and frequency- domains, against the analytical results are given with the associated computational costs.

3.4.1 Example of the DFs extraction
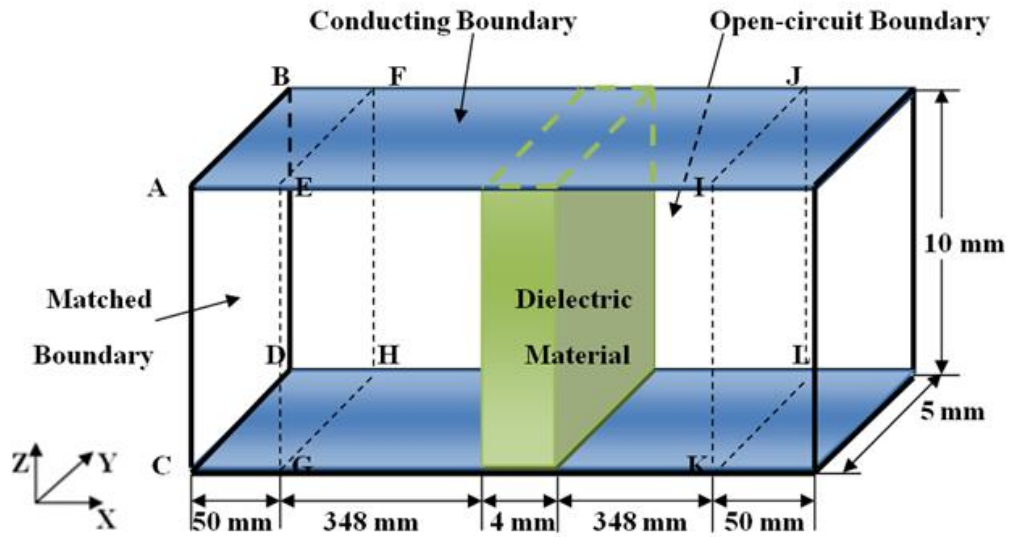
Fig.3.2 The model of the three-dimensional SCN mesh with a dielectric block of $\varepsilon_r = 30$. The space-step of the model is 1 mm. $\left(\Delta l_f = 1mm\right)$

The model in Fig.3.2 is a 4 mm x 5 mm x 10 mm (thickness x width x height) dielectric block with ε_r of 30 placed in a problem space of 800 mm x 5 mm x 10 mm. The space step of the model $\left(\Delta l_f\right)$ is 1 mm. The external boundary conditions are matched for Xmin-Xmax, open-circuited for Ymin-Ymax and conducting for Zmin-Zmax. Note that, conducting boundaries are represented as metals or as conducting plates (blue plates in Fig.3.2) at the top and the bottom of the models.

The time-domain simulation results are obtained by exciting the input voltage $\left(V_{in}\right)$ with a Gaussian pulse of 1 V in Z-direction, with half-width of 7.5 ns and X-directional propagation on the ABCD plane by using the same equation (2.19). The results are observed at planes EFGH and IJKL in the Z-direction, by using equations similar to (2.20) and (2.21), as illustrated in Fig.3.3 and 3.4 respectively.

0.440967
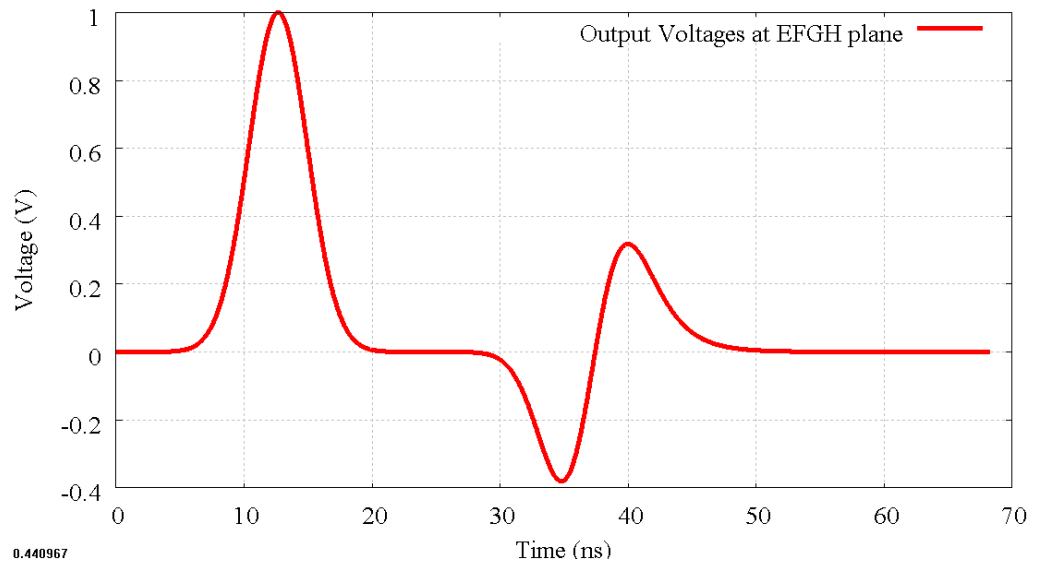
Fig.3.3 The time-domain results in Z-direction observed at EFGH plane where the first pulse with magnitude of 1 V at time between 5-21 ns approximately is the input

voltage and the second pulse at time between 30-50 ns is a reflected voltage

$(V_{reflect})$**with magnitude of 0.32 V and -0.37 approximately.**
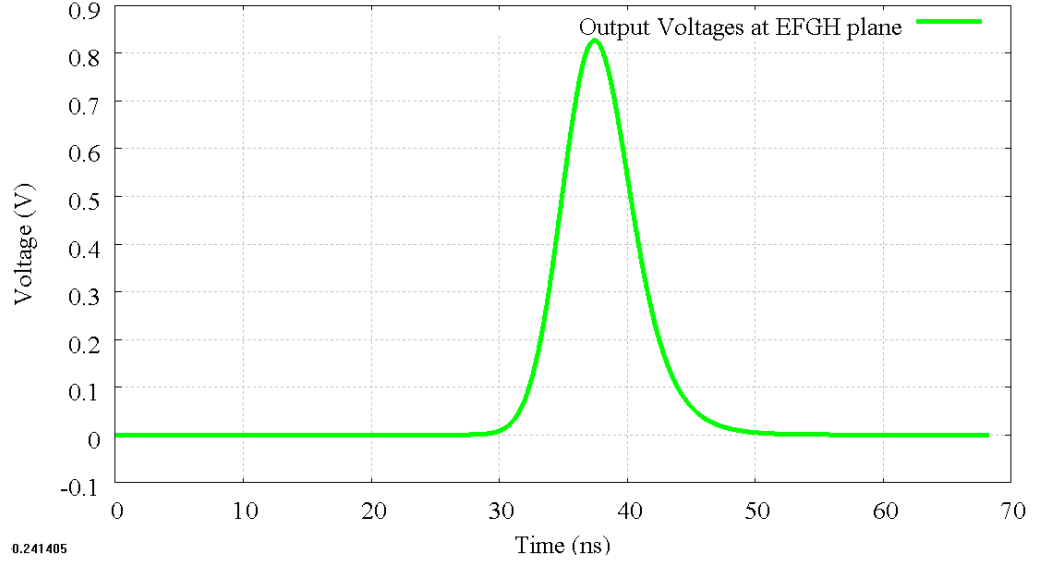
Fig.3.4 The time-domain results in Z-direction observed at IJKL plane where the voltage pulse between 30-50 ns is a transmitted voltage (V_{trans})**with magnitude of 0.83 V.**

The time-domain voltage results in Fig.3.3 and 3.4 can be transformed to frequency-dependent reflection and transmission coefficients by applying an FFT as below.

First, the reflected and input voltages ($V_{reflect}$ and V_{in}) in Fig.3.3 must be separated by assuming that the input voltage has a magnitude of zero. The alternative method is to observe only the incident voltage that is opposite to the X-directional propagation as given in (3.18a). Consequently, the reflected voltage is obtained as shown in Fig.3.5.

$$V_{reflected\_plane\_EFGH} = \frac{\sum_{y=0}^{y=NY}\sum_{z=0}^{z=NZ}\left({}_kV_{11}^i(x,y,z)\right)}{NY} \qquad (3.18a)$$

63

$$V_{input\_plane\_EFGH} = \frac{\sum\limits_{y=0}^{y=NY} \sum\limits_{z=0}^{z=NZ} \left({}_k V_{10}^i (x+1, y, z) \right)}{NY} \tag{3.18b}$$

$$V_{output\_plane\_EFGH} = \frac{\sum\limits_{y=0}^{y=NY} \sum\limits_{z=0}^{z=NZ} \left({}_k V_{11}^i (x, y, z) + {}_k V_{10}^i (x+1, y, z) \right)}{NY} \tag{3.18C}$$

Note that, in general, the output voltage observed on plane EFGH is considered as the sum of the incident voltages in the opposite (3.18a) and the same direction as the X-directional propagation (3.18b) on plane EFGH. As mentioned, the reflected voltage can be obtained directly from (3.18a). The input voltage is also obtained directly from (3.18b). Therefore, the sum of both voltages (3.18c) will give the result as shown in Fig.3.3.

Secondly, the input voltage must be obtained separately for it to propagate the same distance as the reflected and transmitted voltages in order to achieve the correct phase angle for the reflection and transmission coefficients correspondingly.

In this example, it can be simply obtained by removing the dielectric block in the model in Fig.3.2, and observing the input voltage at plane IJKL. It has now travelled the same distance as the transmitted and reflected voltages, because this model is symmetrical and the distance from the voltage source to the observed plane IJKL (750 mm) is equal to the sum of the distances from the voltage source to the centre and from the centre to the observed plane EFGH (400 mm+350 mm = 750 mm). Consequently, the result is obtained as shown in Fig. 3.6.

Lastly, the FFT is applied to the reflected, transmitted and input voltages in Fig.3.5, 3.4 and 3.6 respectively. The reflection and transmission coefficients, $R(s)$ and $T(s)$, can be obtained as given in (3.19) and (3.20)

$$R(s) = \frac{FFT\left[V_{reflect}(k)\right]}{FFT\left[V_{in}(k)\right]}$$
(3.19)

$$T(s) = \frac{FFT\left[V_{trans}(k)\right]}{FFT\left[V_{in}(k)\right]}$$
(3.20)

0.519341
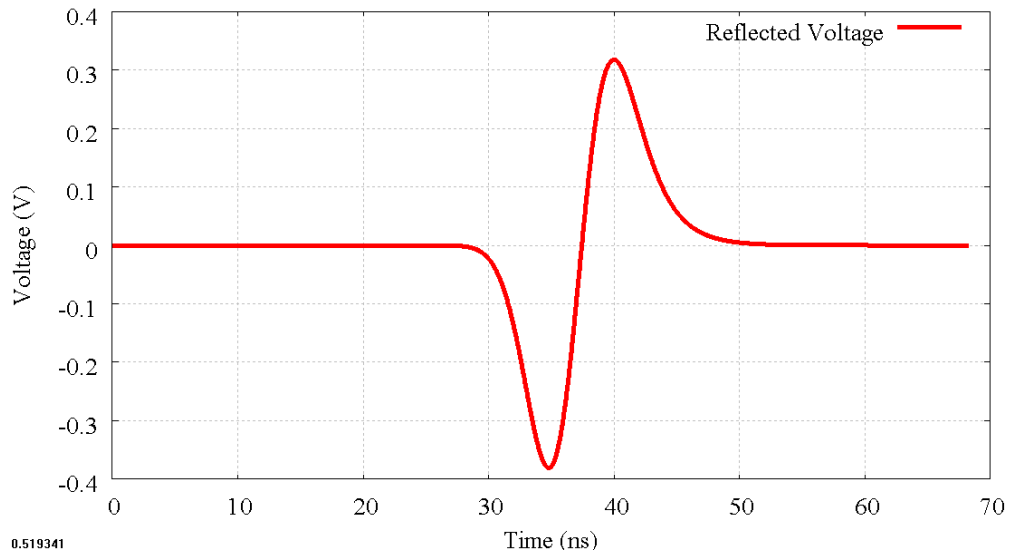
Fig.3.5 The time-domain reflected voltage occurred at time 30-50 ns.
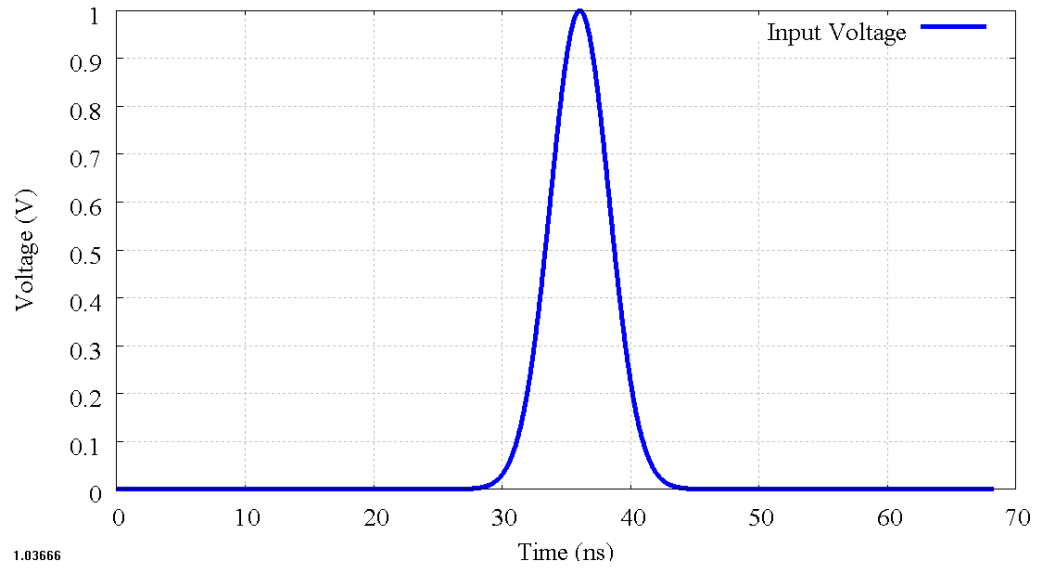
Fig.3.6 The time-domain input voltage occurred at time 30-50 ns.

Hence, the magnitudes of reflection and transmission coefficients are obtained as shown in Fig. 3.7 and 3.8.
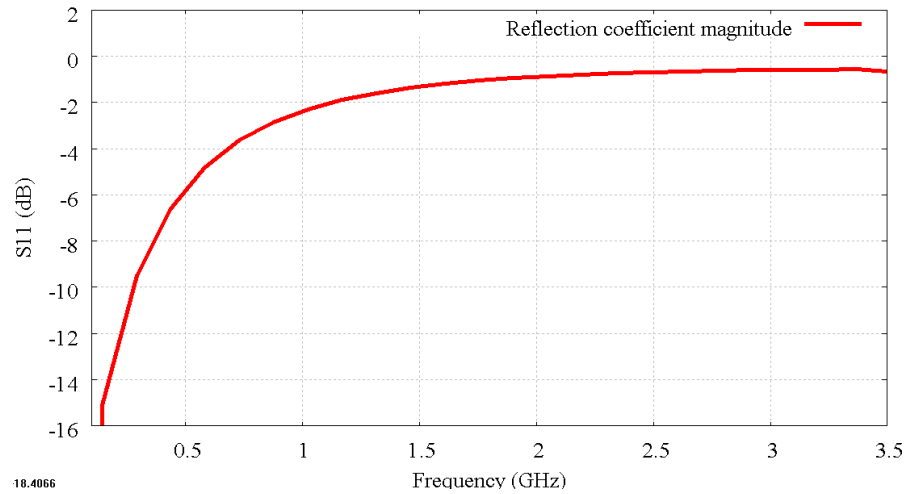
Fig.3.7 The frequency-dependent reflection coefficients magnitude $R(s)$ **at the frequency 0-3.5 GHz.**

66
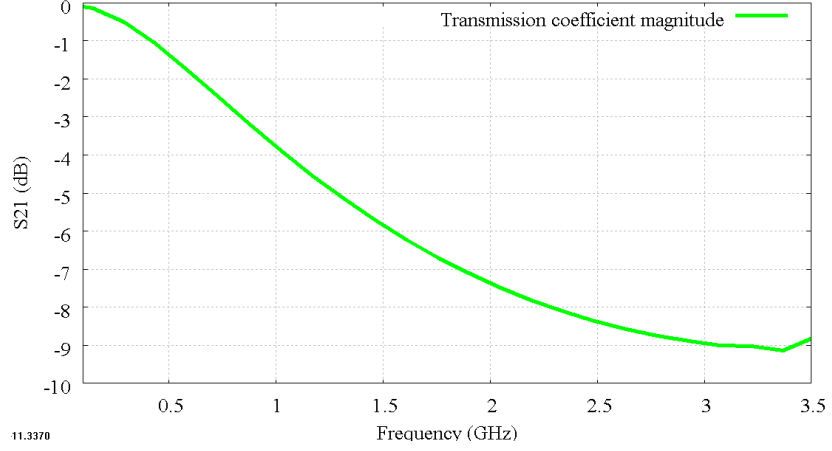
Fig.3.8 The frequency-dependent transmission coefficients magnitude $T(s)$ at the frequency 0-3.5 GHz.

Then, $R(s)$ and $T(s)$ as shown by their magnitudes in Fig.3.7 and 3.8 respectively, are employed to extract the DF parameters by following the equations (3.3)-(3.12). From this, $R(z)$ and $T(z)$ are obtained.

For this model, the approximation of DF parameters are based on three and four poles ($NP=3$ and $NP=4$) for $T(s)$ and $R(s)$ respectively. The time-step (Δt) used in the equations (3.9) and (3.11) can be calculated by substituting the space-step of a designed model (Δl_{DF}) in Fig.3.9 into the equation (2.8) as given in (3.21).

$$\Delta t = \frac{\Delta l_{DF}}{2c} \tag{3.21}$$

where c is speed of light.

Both $R(z)$ and $T(z)$ are used in the three-dimensional TLM mesh, as DFs or DF transfer functions as given in (3.17), by embedding at the surfaces between adjacent nodes to represent the properties of the dielectric block with ε_r of 30.

67

3.4.2 Comparison and results

As mentioned before, the original space step of the TLM model with load-stubs in Fig.3.2 is 1 mm $\left(\Delta l_f = 1mm\right)$. Let us consider that the designed model has the same physical properties, the observation places and boundary conditions but with a coarser mesh than the model in Fig.3.2 with a space-step of 5 mm $\left(\Delta l_{DF} = 5mm\right)$. The digital filters (DFs) or the internal boundary which contain the information of the dielectric block with ε_r of 30.00 are embedded into the designed model instead of an explicit dielectric block as shown in Fig. 3.9.
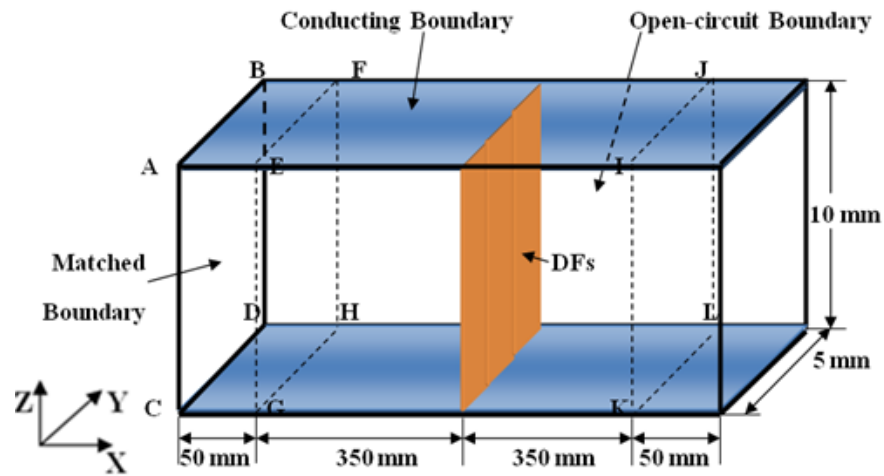
Fig.3.9 The model of the three-dimensional SCN mesh with the DFs or an internal boundary. The space-step of the model is 5 mm $\left(\Delta l_{DF} = 5mm\right)$**.**

A comparison between the finely meshed model in Fig.3.2 and the coarsely meshed model with the DFs in Fig.3.9 can be made by exciting with the same Gaussian pulse of 1 V in the Z-direction on the ABCD plane. The propagation

is along the X-direction. Then, the time-domain output voltages, reflected and transmitted voltages in the Z-direction, can be observed on the planes EFGH and IJKL as illustrated in Fig. 3.10 and 3.11 respectively. Then, an FFT is applied to them in order to obtain the frequency-domain results as shown in Fig. 3.12 and 3.13. Moreover, the frequency-domain results can be compared with the analytical results which are calculated from the Fresnel's reflection formulae as given in (2.22) and (2.23).
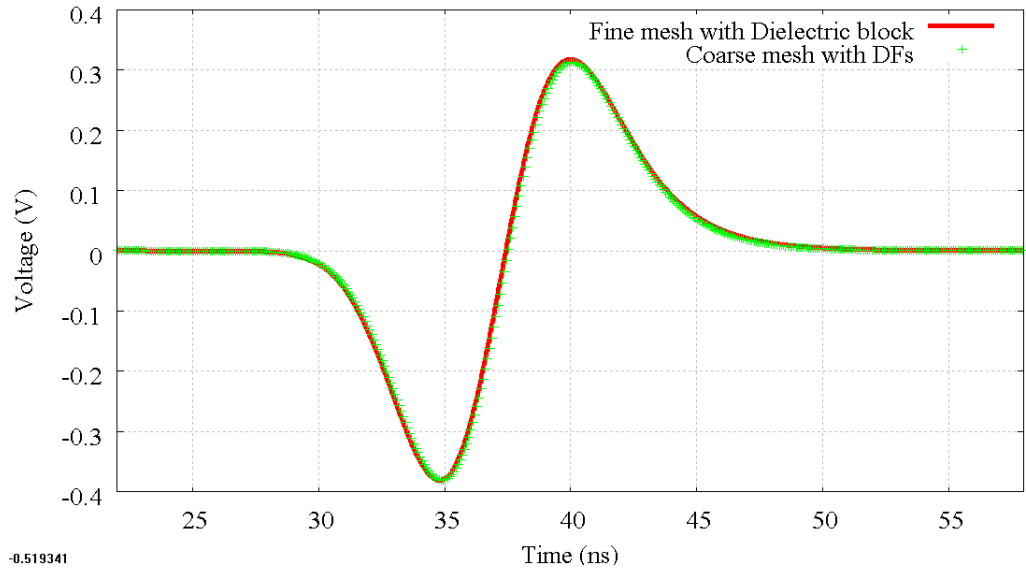
Fig.3.10 The time-domain reflected voltages observed on the plane EFGH in the fine mesh with dielectric block model in Fig. 3.2 (red line) and the coarse mesh with DF model in Fig.3.9 (green dot).
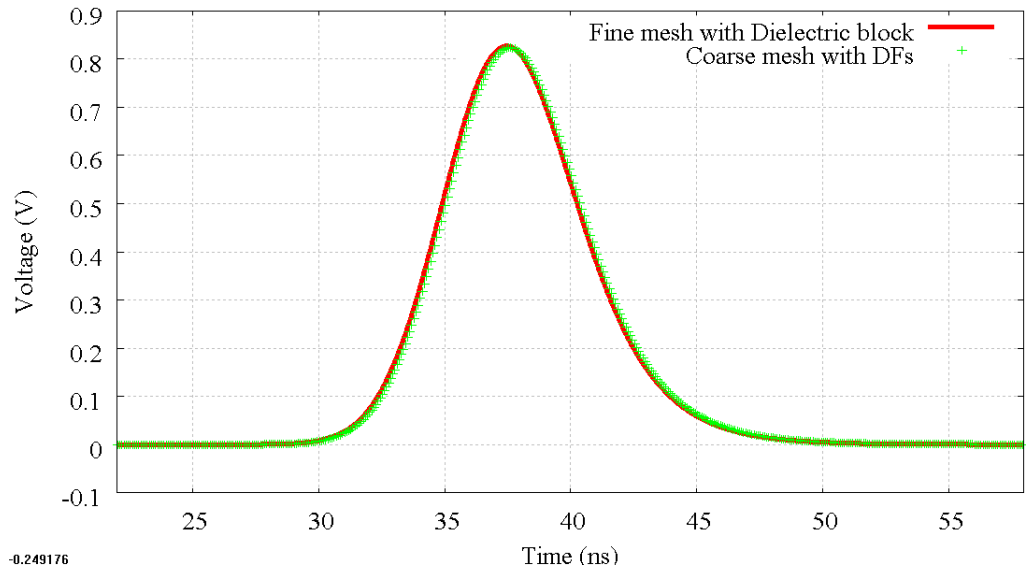
Fig.3.11 The time-domain transmitted voltages observed on the plane IJKL in the fine mesh with dielectric block model in Fig. 3.2 (red line) and the coarse mesh with DF model in Fig.3.9 (green dot).
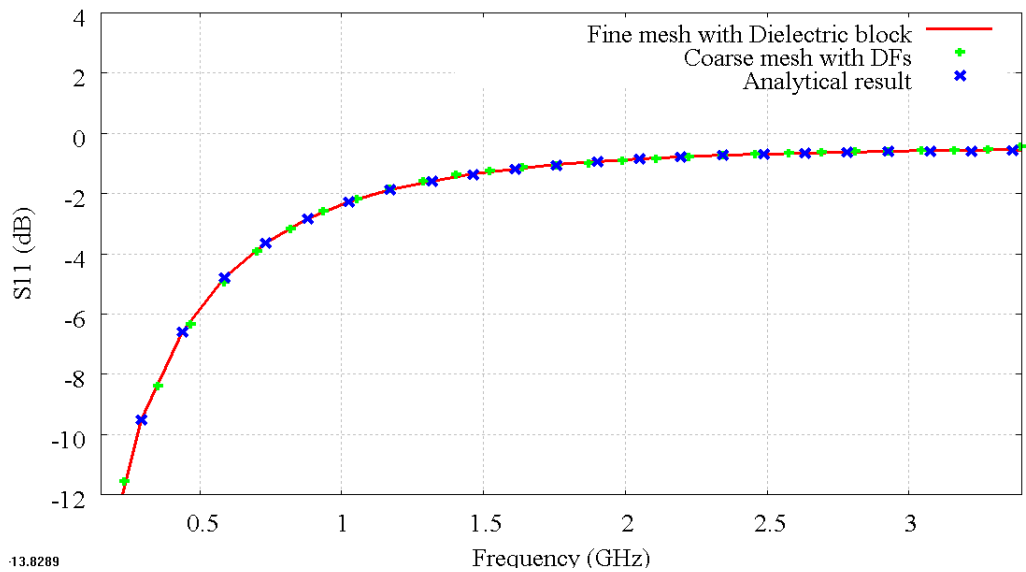
Fig.3.12 The frequency-domain reflected voltages observed on the plane EFGH in the fine mesh with dielectric block model in Fig. 3.2 (red line) and the coarse mesh with DF model in Fig.3.9 (green dot) compared with the analytical result (blue cross).
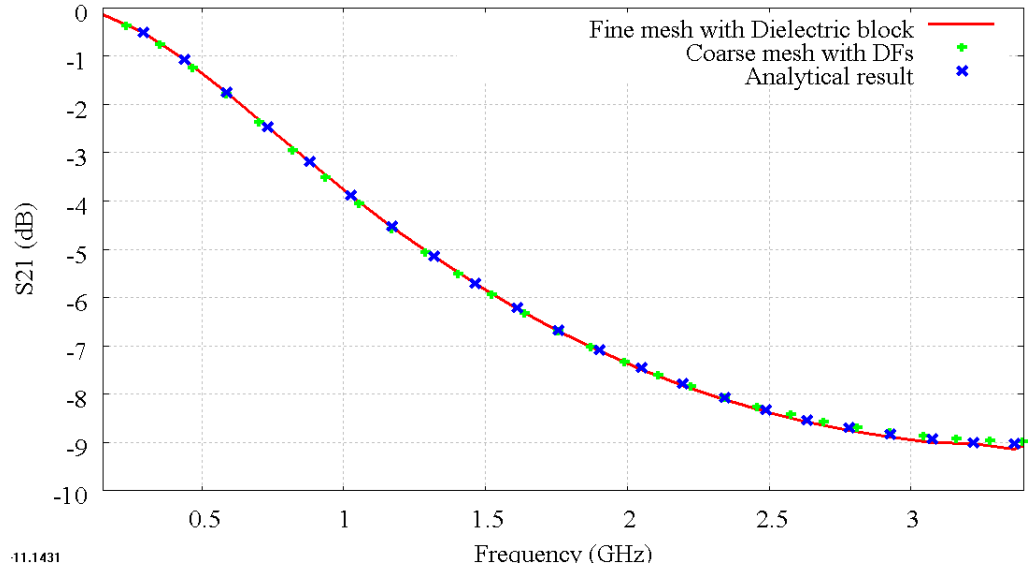
Fig.3.13 The frequency-domain transmitted voltages observed on the plane IJKL in the fine mesh with dielectric block model in Fig. 3.2 (red line) and the coarse mesh with DF model in Fig.3.9 (green dot) compared with the analytical result (blue cross).

The results in time- and frequency- domains show a good agreement between the two methods and the analytic results. Note that the maximum frequency for these comparisons is around 6 GHz because of the mesh dispersion in the TLM coarse mesh model. However, the maximum frequency shown in Fig. 3.12 and 3.13 is 3.5 GHz because the bandwidth and energy of the input voltage in the Gaussian form is limited at 3.5 GHz.

The computational requirements for both models are compared in Table 3.1.

71

TABLE 3.1

The comparison of computational requirements between two models in Fig.3.2 and 3.9.

Model	Number of nodes (NX)x(NY)x(NZ)	Number of time-steps	Memory (kB)	CPU Time (s)
Fine mesh with a dielectric block model in Fig. 3.2 $\left(\Delta l_f = 1mm\right)$	800 x 5 x 10	4096	12,276	67.73
Coarse mesh with DFs model in Fig. 3.9 $\left(\Delta l_{DF} = 5mm\right)$	160 x 1 x 2	1024	2,532	0.84

The computer used for the TLM simulation has an Intel®Core ™ i7 CPU clocked at 1.60 GHz and has an installed memory (RAM) of 4.00 GB.

3.5   Conclusion

This chapter introduced the DF techniques. It first explained how to extract the DF parameters from fine features. The FFT, the frequency-domain Prony method and the bilinear z-transform were used in the procedure to apply the DF techniques to the three-dimensional TLM mesh. This technique for the three-dimensional TLM mesh with load-stubs was demonstrated with an example. The comparison showed that the digital filters can replicate the properties of a fine feature producing good agreement and comparable accuracy to the simulation results in both time- and frequency- domains with much lower computational requirements as shown in Table 3.1.

However, the technique is limited to the internal boundary or plane in the three-dimensional TLM mesh. In the other words, only the responses of single node faces could be considered. The next chapter develops the DF techniques in order to be able to apply it to the problem of small three-dimensional structures.

3.6 References

[3.1]   J. Paul, C. Christopoulos, and D. W. P. Thomas, "Generalized material models in TLM—Part 1: Materials with frequency-dependent properties," *IEEE Trans. Antennas Propagat.*, vol. 47, pp. 1528–1534, Oct.1999.

[3.2]   J. Paul, C. Christopoulos, and D. W. P. Thomas, "Generalized material models in TLM—Part 2: Materials with anisotropic properties," *IEEE Trans. Antennas Propagat.*, vol. 47, pp. 1535–1542, Oct. 1999.

[3.3]   J. Paul, C. Christopoulos, and D. W. P. Thomas, "Generalized material models in TLM—Part 3: Materials with nonlinear properties," *IEEE Trans. Antennas Propagat.*, vol. 50, pp. 997–1004, July 2002.

[3.4]   A. Taflove and S. C. Hagness, Computational Electrodynamics, *The Finite-Difference Time-Domain Method*, 2nd ed., Norwell, MA: Artech House, 2000.

[3.5]   K. S. Yee, "Numerical solution of initial boundary value problems involving Maxwell's equations in isotropic media," *IEEE Trans. Antennas Propagat..,* vol. 14, pp. 302-307, 1966.

[3.6]   J. Paul, V. Podlozny, and C. Christopoulos, "The use of digital filtering techniques for the simulation of fine features in EMC problems solved in the time domain," *IEEE Trans. Electromagn. Compat.,* vol. 45, no. 2, pp. 238-244, May 2003.

[3.7]   J. N. Brittingham, E. K. Miller, and J. L. Willows, "Pole extraction from real-frequency information," *Proc. IEEE*, vol. 68, pp. 263-273, Feb. 1980.

[3.8]   J.-H. Lee and H.-T. Kim, "Selection of sampling interval for least squares Prony method", *Electron. Lett.*, vol. 41, pp. 47-49, Jan. 2005.

[3.9]   A. Ralston and P. Rabinowitz, A First Course in Numerical Analysis, 2nd ed., New York: Dover, 2001.

[3.10] W.H. Press, S.A. Teukolsky, W.T. Vetterling and B.P. Flannery, Numerical Recipes: The Art of Scientific Computing, 3rd ed., New York: Cambridge University Press, 2007.

[3.11] D.A. Adams, "A Stopping Criterion for Polynomial Root Finding," Communications of the ACM, vol. 10, pp. 655-658.

4. Development of Digital Filtering Techniques within Three-Dimensional TLM Models

The previous chapter has illustrated the technique based on digital filters (DF) to represent fine features in time-domain three dimensional TLM simulations for planes and boundaries. This chapter develops the DF technique for small three-dimensional structures. In detail, the method to construct a DF node from an arbitrarily shaped object is described. The TLM fine mesh with thin-wire model is used as an example to illustrate the technique and demonstrate the significant computational saving. This chapter also discusses the limitations of this technique, the solutions to which are fully described in chapter 5.

4.1 The purpose of the development DF techniques

The main problem of the DF techniques described in chapter 3 is that the DF can only represent a fine feature as a plane or as an internal boundary as shown in Fig.3.9. In the other words, this internal boundary can represent the electromagnetic properties of the fine feature in one dimension or in two directions (direct forward and backward). However, a fine feature can be three-dimensional and the previously described technique is unable to provide its

electromagnetic properties in other dimensions. Therefore, a three dimensional DF technique is developed in order to apply digital filters to represent the properties of three dimensional fine features.

This chapter describes the initial development of a DF node which can replicate the properties of a fine feature in the three-dimensional TLM mesh. However, there are conditions and limitations to this technique as described in the next section.

4.2   The method to construct the DF node from a fine feature

Chapter 3 shows that DF transfer functions can be embedded at the surface between three-dimensional TLM nodes. For the initial development of the DF technique, the DF transfer functions are now embedded inside an SCN node similar to the scattering matrix as shown in (2.17). This also means that they are accounted as part of the "Scattering" process in three dimensional TLM simulations. Moreover, the SCN node with DF transfer functions is now referred to as a "DF node". The procedure of the DF nodes' creation is described as below.

A fine feature such as a thin wire is modelled by employing DF embedded into a coarse mesh node under the following steps.

The steps are; (i) the fine feature must be first modelled in a TLM fine mesh with some cubical volume as a TLM coarse mesh node in order to construct the DF node. The relationship between the space steps of the cubical volume containing the fine feature in a fine mesh Δl_f and the coarse DF node Δl_{DF} is given in (4.1) and is illustrated in Fig. 4.1.

$$\Delta l_{DF} = n\Delta l_f \qquad\qquad (4.1)$$

where n is a ratio of the space steps between the fine mesh and coarse DF-node.

(ii) The fine feature must be placed between two metal surfaces. Note that, this condition will be removed at a later stage in development of DF techniques.
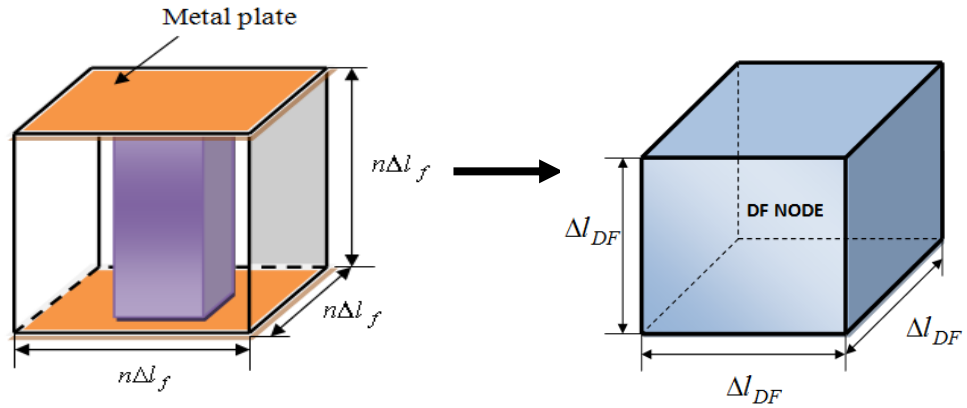
Fig.4.1 A fine feature with space step Δl_f will be transformed to a DF node with space step Δl_{DF} .

(iii) Each face of the fine mesh is excited by a voltage pulse between the conducting plates and the scattered voltages are recoded.

Generally, the cubical volume containing the fine feature is considered as a single coarse mesh node (DF node). This can be done by using the average

scattered and incident voltages $\left(\sum_n \sum_n V_f^r(n,n) \big/ n, \sum_n \sum_n V_f^i(n,n) \big/ n \right)$ at each of the boundary faces of the cubical volume of fine cells containing the feature, except the boundary faces attached with metal plates, to be the scattered and incident voltages of the ports of the equivalent coarse TLM cell $\left(V_{DF}^r, V_{DF}^i \right)$ respectively. These relations are,

$$V_{DF}^r = \frac{\sum_n \sum_n V_f^r(n,n)}{n} \tag{4.2}$$

$$V_{DF}^i = \frac{\sum_n \sum_n V_f^i(n,n)}{n} \tag{4.3}$$

$V_{DF}^r(k)$ and $V_{DF}^i(k)$ obtained by (4.2) and (4.3) in the discrete time-domain are converted to the discrete frequency-domain by applying the Fast Fourier Transform (FFT). Then, the frequency-dependent complex filter coefficients $F(s)$ are obtained from (4.4) below.

$$F(s) = \frac{FFT\left[V_{DF}^r\left(k - (n-1) \right) \right]}{FFT\left[V_{DF}^i(k) \right]} \tag{4.4}$$

where s is the complex frequency and $\left(k - (n-1) \right)$ indicates the time shift of the scattered voltage. This time shift is required in order to represent the responses of the fine mesh and coarse mesh TLM nodes in synchronism. Further detail on the time shifting of $\left(k - (n-1) \right)$ is given in section 4.3.1.

Then, the frequency-dependent complex filter coefficients $F(s)$ in (4.4) are used to find the DF transfer functions $DF()$ by applying the frequency-domain Prony method [4.1]-[4.4] and the Bilinear-Z-transform as described in chapter 3 using equations (3.2)-(3.17).

As mentioned in chapter 2, the three dimensional SCN node is represented by a scattering matrix (S) relating the vector of scattered voltages $\left({}_k\vec{V}^r\right)$ to the vector of incident voltages $\left({}_k\vec{V}^i\right)$ as given in (4.5).

$${}_k\vec{V}^r = S\,{}_k\vec{V}^i \tag{4.5}$$

where k is time-step.

Therefore, a DF node is constructed to relate the vectors of scattered and incident voltages $\left(\vec{V}_{DF}{}^r, \vec{V}_{DF}{}^i\right)$ in the form of a DF-node scattering matrix DFS as given in (4.6).

$${}_k\vec{V}_{DF}{}^r = DFS\,{}_k\vec{V}_{DF}{}^i \tag{4.6}$$

For this initial DF technique, consider the DF node as a three dimensional SCN node with twelve ports indexed as shown in Fig. 4.2 with the condition that the fine feature is placed between two metal plates as illustrated in Fig. 4.1. Therefore, DFS of this DF node is obtained in the form shown in (4.7).
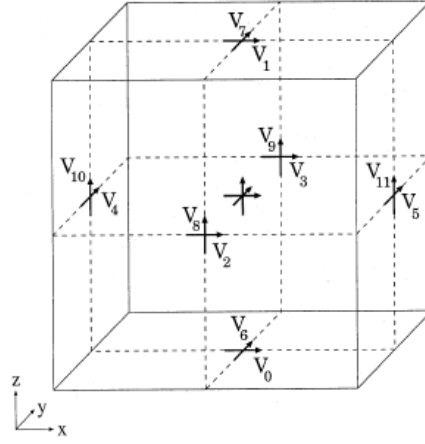
Fig.4.2 A three-dimensional symmetrical condensed TLM node [4.5].

$$DFS \;=$$

Port	0	1	2	3	4	5	6	7	8	9	10	11
0												
1												
2			$DF_{ij}()$	$DF_{ij}()$	$DF_{ij}()$	$DF_{ij}()$			$DF_{ij}()$	$DF_{ij}()$	$DF_{ij}()$	$DF_{ij}()$
3			$DF_{ij}()$	$DF_{ij}()$	$DF_{ij}()$	$DF_{ij}()$			$DF_{ij}()$	$DF_{ij}()$	$DF_{ij}()$	$DF_{ij}()$
4			$DF_{ij}()$	$DF_{ij}()$	$DF_{ij}()$	$DF_{ij}()$			$DF_{ij}()$	$DF_{ij}()$	$DF_{ij}()$	$DF_{ij}()$
5			$DF_{ij}()$	$DF_{ij}()$	$DF_{ij}()$	$DF_{ij}()$			$DF_{ij}()$	$DF_{ij}()$	$DF_{ij}()$	$DF_{ij}()$
6												
7												
8			$DF_{ij}()$	$DF_{ij}()$	$DF_{ij}()$	$DF_{ij}()$			$DF_{ij}()$	$DF_{ij}()$	$DF_{ij}()$	$DF_{ij}()$
9			$DF_{ij}()$	$DF_{ij}()$	$DF_{ij}()$	$DF_{ij}()$			$DF_{ij}()$	$DF_{ij}()$	$DF_{ij}()$	$DF_{ij}()$
10			$DF_{ij}()$	$DF_{ij}()$	$DF_{ij}()$	$DF_{ij}()$			$DF_{ij}()$	$DF_{ij}()$	$DF_{ij}()$	$DF_{ij}()$
11			$DF_{ij}()$	$DF_{ij}()$	$DF_{ij}()$	$DF_{ij}()$			$DF_{ij}()$	$DF_{ij}()$	$DF_{ij}()$	$DF_{ij}()$

(4.7)

where $DF_{ij}()$ is a DF transfer function relating an incident voltage into the port

i to a scattered voltage from port j .

Note that there is no $DF_{ij}()$ at ports 0, 1, 6 and 7 in (4.7) because these ports

contain the metal plates. Therefore, they are considered to be zero as there is

no incident pulse or a scattered pulse.

81

4.3   The application of the initial DF technique.

In this example, a three dimensional TLM fine mesh with a thin-wire model as shown in Fig. 4.3 is investigated. It is a thin-wire or a conducting post of 3 mm x 3 mm x 5 mm placed in an air-space of 5 mm x 5 mm x 5mm. In addition, the top and bottom of the thin-wire are attached to metal plates of 5 mm x 5mm. This also means that the external boundary conditions at the top and bottom (Zmin, Zmax) are conducting. The boundary conditions at Xmin, Xmax, Ymin and Ymax are matched. The space step of the model is 1 mm $\left(\Delta l_f = 1mm \right)$.
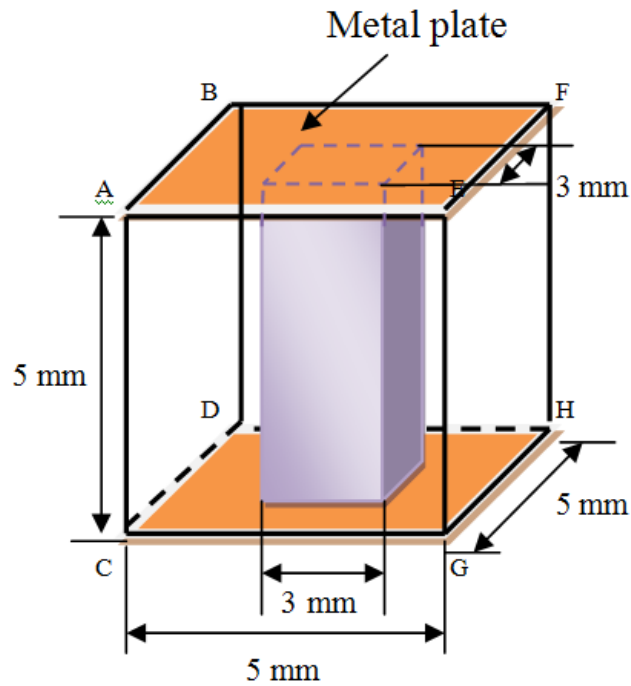
Fig.4.3 A fine mesh with thin-wire model. The space step is 1 mm $\left(\Delta l_f = 1mm \right)$.

The DF node can be constructed from the thin-wire model in Fig.4.3 by first obtaining each coefficient $DF_{ij}()$ by exciting the input or incident voltage $\left(\sum_n \sum_n V_f^i(n,n) \big/ n \right)$ by a Gaussian pulse of 1 V peak and 0.11 ns half-width in the Z-direction, with X-directional propagation at the ABCD plane as illustrated in Fig4.4. The outputs or scattering the Z-directed voltages $\left(\sum_n \sum_n V_f^r(n,n) \big/ n \right)$ are observed at planes ABCD and EFGH in Xmin and Xmax planes. The Z-directed voltages are also observed at planes AECG and BFDH. These voltages are considered as the scattered and incident voltages of the ports of an equivalent single coarse mesh node (DF node with space step of 5 mm) $\left(V_{DF}^r, V_{DF}^i \right)$ by using equations (4.2) and (4.3) respectively. The outputs are observed in time-domain as shown in Fig. 4.5-4.7.
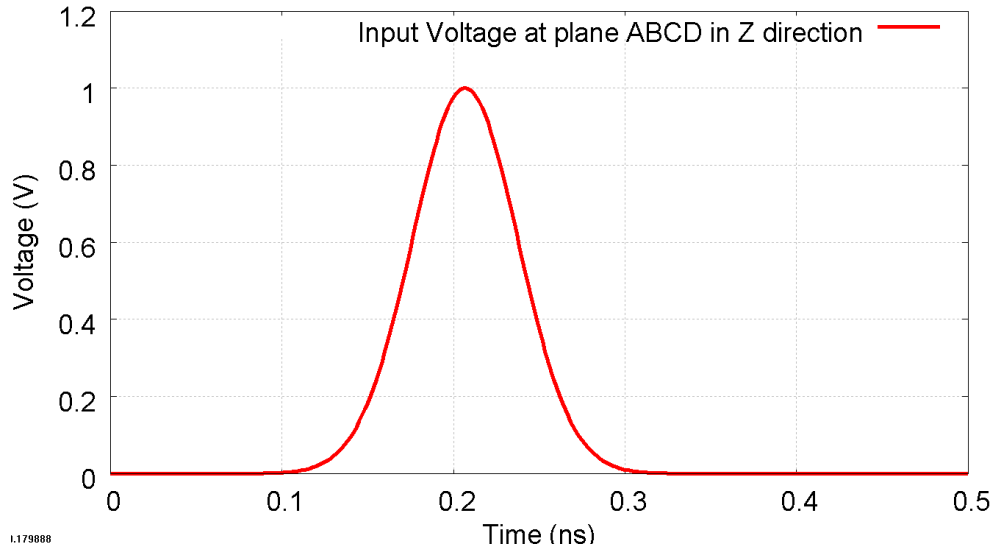
Fig.4.4 The time-domain input or incident voltage of 1 V in Z-direction on plane ABCD.
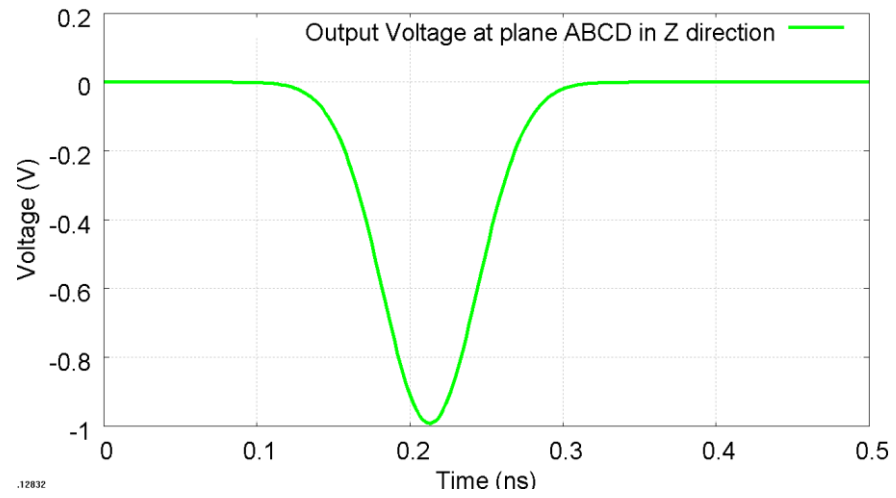
Fig.4.5 The time-domain output or scattering voltage in Z-direction on plane ABCD.
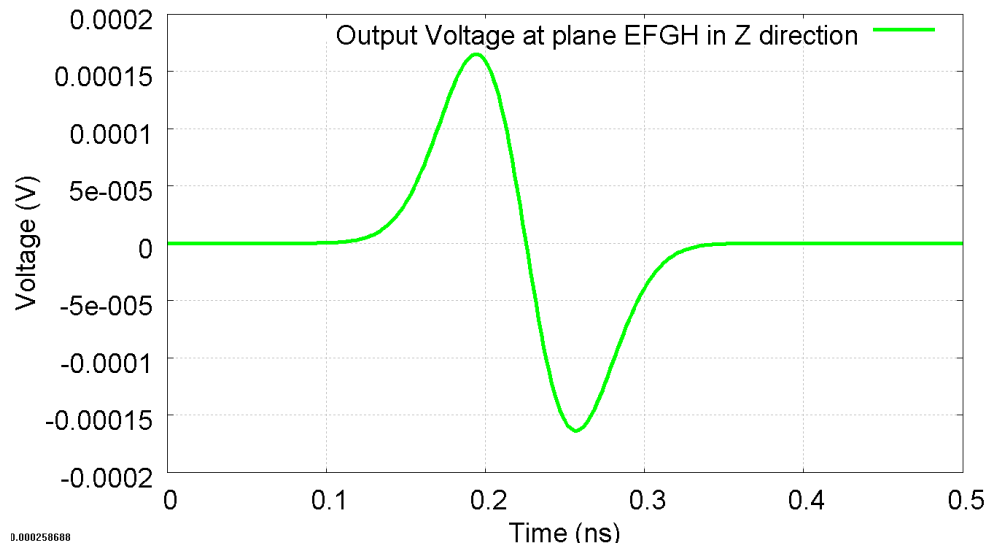
Fig.4.6 The time-domain output or scattering voltage in Z-direction on plane ABCD.

).0485547
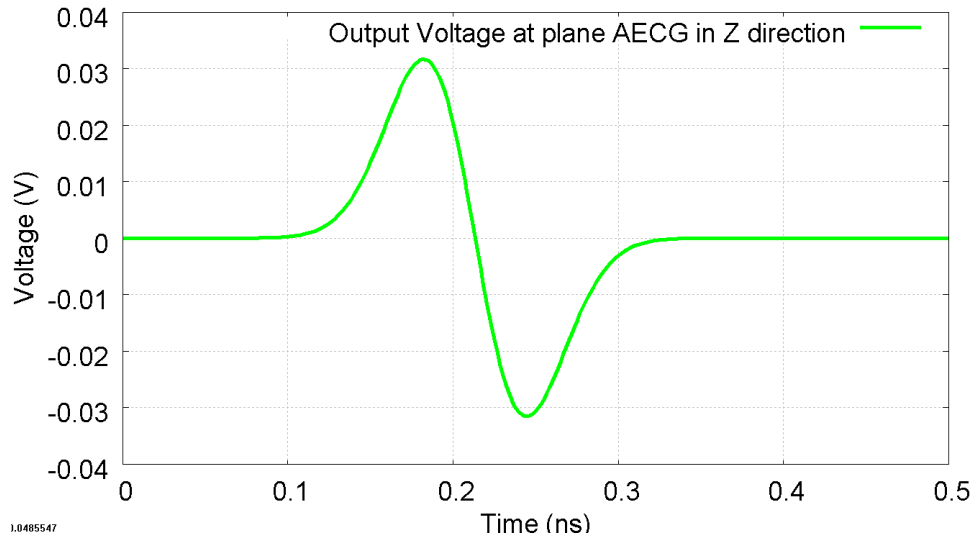
Fig.4.7 The time-domain output or scattering voltage in Z-direction on plane AECG.

Note that the output voltage in the Z-direction on plane BFDH is the same as that on plane AECG as illustrated in Fig.4.7. The rest of the output voltages in the X and Y-directions are zero.

The next step is to shift the magnitude of the output voltages in Fig. 4.5-4.7 by $(k-(n-1))$ time-steps where n is 5 in this case. For example, the new output voltage in Z-direction at plane ABCD is obtained as illustrated in Fig. 4.8.
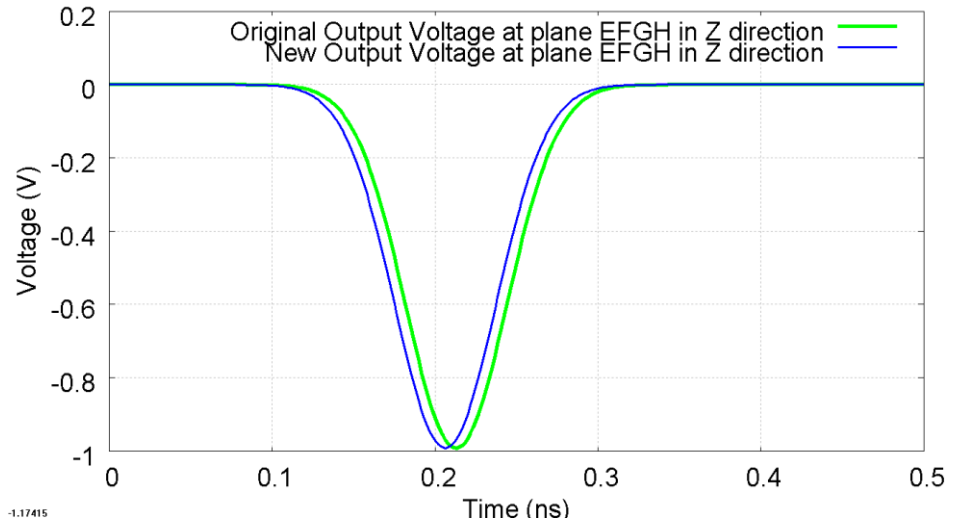
**Fig.4.8 The comparison between original and time-shifted output voltages in Z-direction
at plane ABCD.**

The frequency-dependent complex filter coefficient $F(s)$ can be now determined by dividing each time-shifted Fourier transformed output voltage by the Fourier transformed input voltage as given in equation (4.4). Then, the DF transfer functions are obtained by following equations (3.2)-(3.17). For example, the DF transfer functions obtained by exciting 1 V in the Z-direction with X-directional propagation on plane ABCD in the Model in Fig. 4.3 will be $DF_{i=10, j=10}()$, $DF_{i=10, j=11}()$, $DF_{i=10, j=8}()$ and $DF_{i=10, j=9}()$.

The other coefficients $DF_{ij}()$ can be found by repeating the above process by exciting the input voltage on different faces of the cube. Consequently, the DF node of dimension 5 mm x 5 mm x 5mm for the thin-wire model in Fig.4.3 was obtained with DF filters on each of the X, Y faces.

4.3.1 Explanation of the time shift for determining the coefficients DF function.

This section explains why the magnitudes of the scattering or output voltages as illustrated in Fig. 4.5-4.7 are required to be shifted $n-1$ time-steps in determining the DF transfer functions.

Assuming that; (i) the size of the cubical volume of the fine mesh model **A** and **B** are the same as the coarse mesh nodes **A** and **B** (DF nodes) as illustrated in Fig.4.9. In Fig.4.9, these models are shown in two dimensions (X and Z views). For the fine mesh model A and B, each model contains 5 x 5 TLM nodes at the surface. For the coarse mesh model A and B, each model contains only 1 TLM node. Consequently, the ratio of the space step between the fine mesh and the coarse mesh node is 5; (ii) the average incident and scattering voltages $\left(V_{av}^{i}, V_{av}^{r}\right)$ between the fine mesh model and the coarse mesh node model are the same values as given in equations (4.2) and (4.3).

The fine mesh model **A** and the coarse mesh node **A** are excited by the same characteristic shape and the magnitude of the average incident voltages at the left surface as shown in Fig.4.10. The field propagation for both models is in the X-direction.
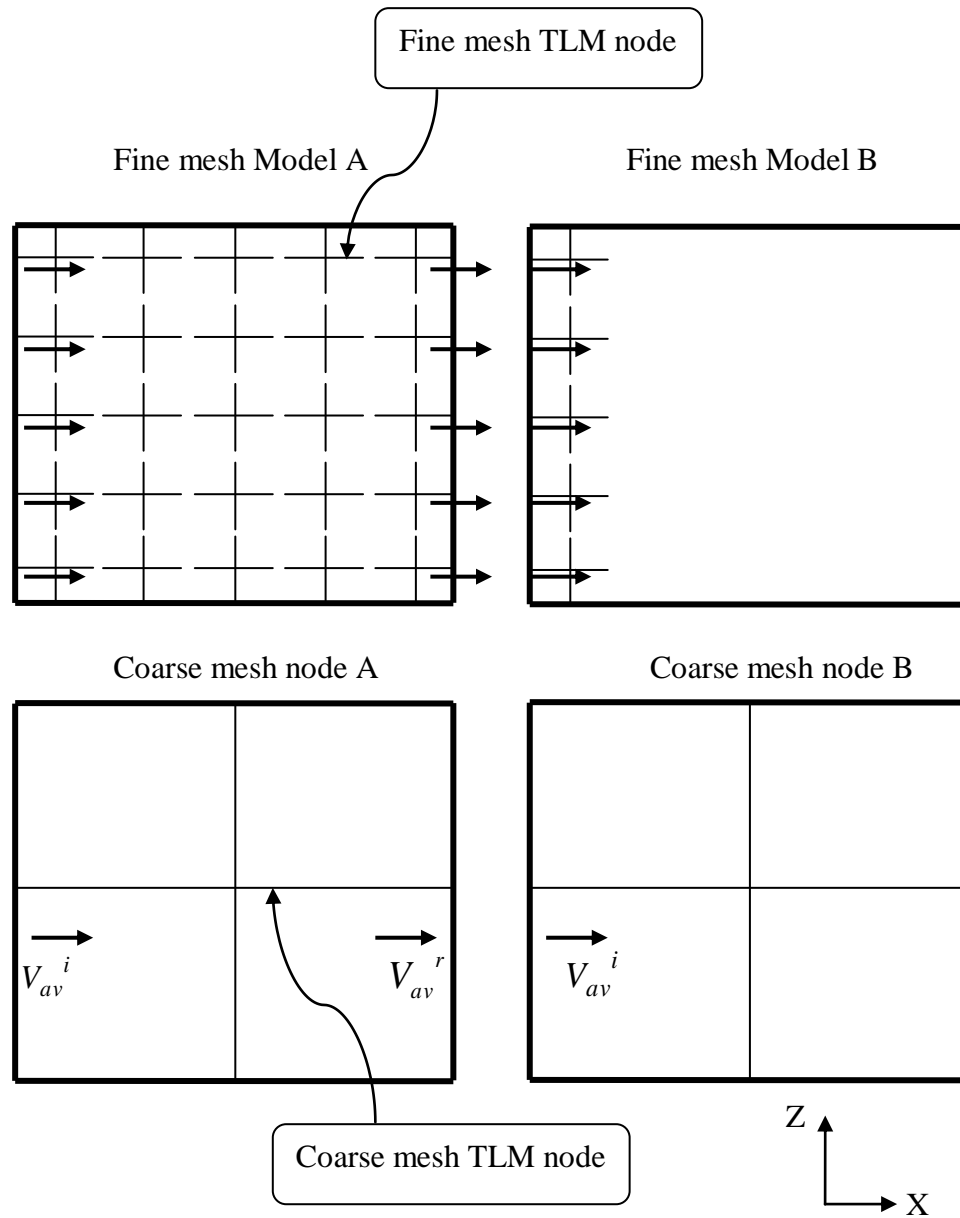
Fig.4.9 The fine and coarse mesh models in X and Z view.

Magnitude
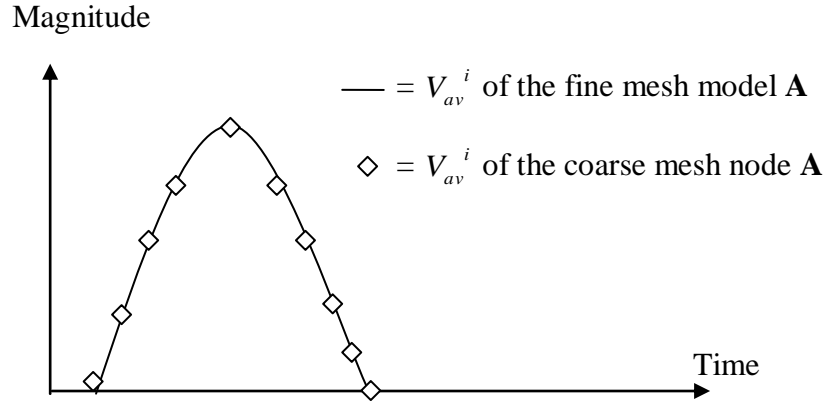
Fig.4.10 The average incident voltages $\left(V_{av}{}^{i}\right)$ at the left surface of the fine mesh model A and coarse mesh node A.

Then, let us assume that the average scattering voltages $\left(V_{av}{}^{r}\right)$ at the right surface of the fine mesh model **A** and the coarse mesh node **A** in Fig.4.9 are obtained from the propagation of $V_{av}{}^{i}$ with the same magnitude and shape as shown in Fig.4.11.

In general, $V_{av}{}^{r}$ in Fig.4.11 will yield new incident voltages to the left surface of the fine mesh model **B** and the coarse mesh node **B** at the next time step as illustrated in Fig.4.9. Both magnitudes in time are shown in Fig.4.12.

Fig.4.12 shows that the new incident voltages at the left surface of the fine mesh model **B** and the coarse mesh node **B** have the same magnitude but have a difference in time occurred due to the difference in the time-steps between the fine mesh and the coarse mesh.

To obtain the new incident voltages for both models at the correct time-step, the magnitude of $V_{av}{}^{r}$ of the coarse mesh node **A** is shifted back $n-1$ steps as shown in Fig.4.13. Consequently, the new $V_{av}{}^{i}$ at the coarse mesh node **B** will be the same as that at the fine mesh model **B** as illustrated in Fig. 4.14.

Magnitude

—— $= V_{av}{}^{r}$ of the fine mesh model **A**

◇ $= V_{av}{}^{r}$ of the coarse mesh node **A**
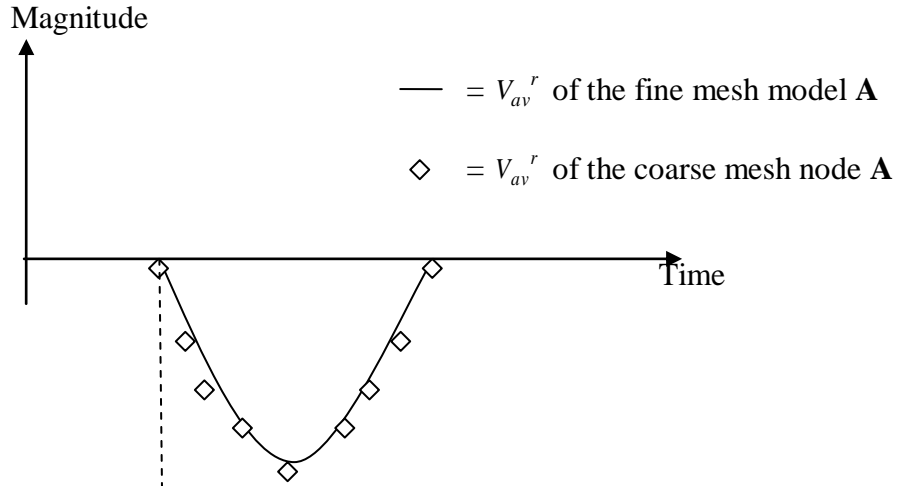
Time

Fig.4.11 The average scattering voltages $\left(V_{av}{}^{r}\right)$ at the right surface of the fine mesh model

A and coarse mesh node A.

—— $= V_{av}{}^{i}$ of the fine mesh model **B**

◇ $= V_{av}{}^{i}$ of the coarse mesh node **B**

Magnitude

Time

1 time fine step

Fig.3

1 time coarse step
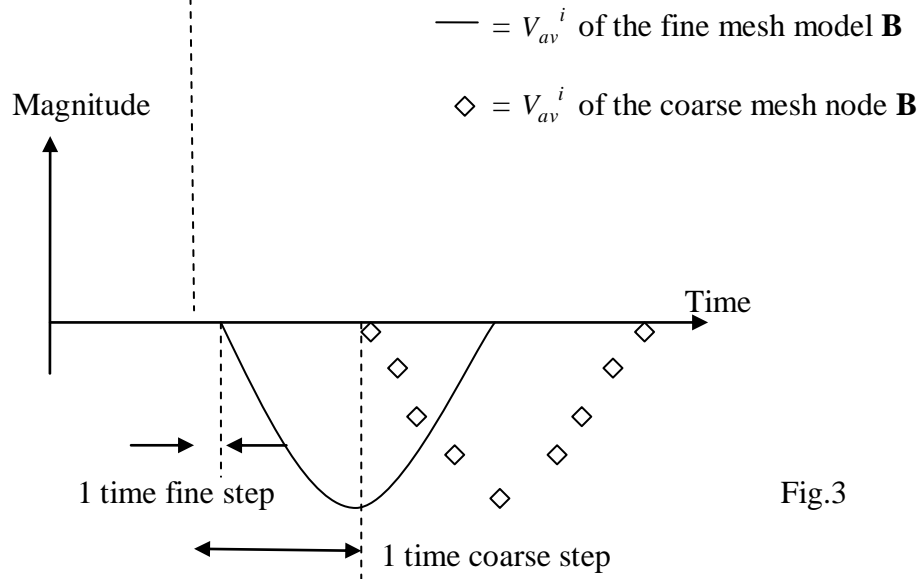
Fig.4.12 The average incident voltages $\left(V_{av}{}^{i}\right)$ at the left surface of the fine mesh model B

and coarse mesh node B at the next time-step.

Magnitude

—— $V_{av}{}^r$ of the fine mesh model **A**

◇ $V_{av}{}^r$ of the coarse mesh node **A**

Time

$n-1$ time Fine steps
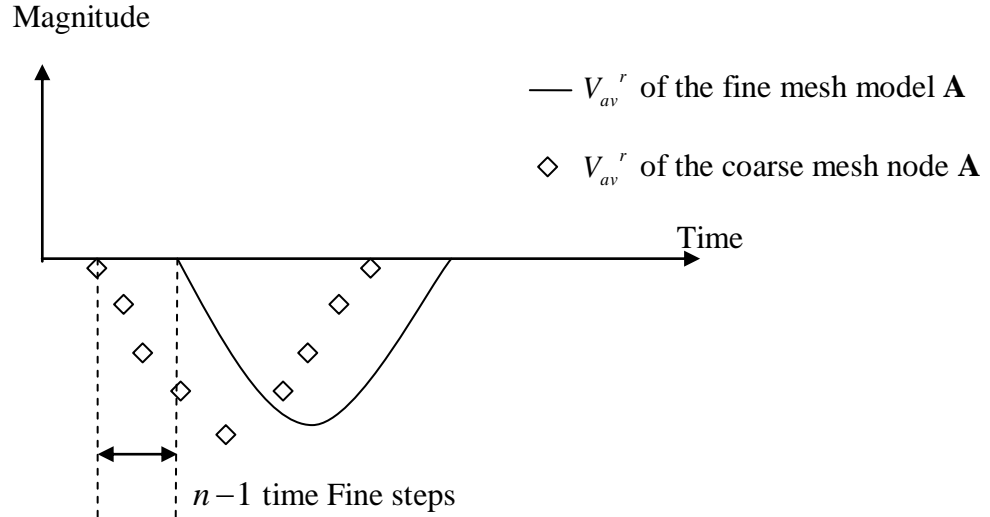
Fig.4.13 The average scattering voltages $\left(V_{av}{}^r\right)$ at coarse mesh node A is time shifted $n-1$

steps.

Magnitude

—— $V_{av}{}^i$ of the fine mesh model **B**

◇ $V_{av}{}^i$ of the coarse mesh node **B**

Time

1 time Fine step

1 time Coarse step $= n$ time Fine steps
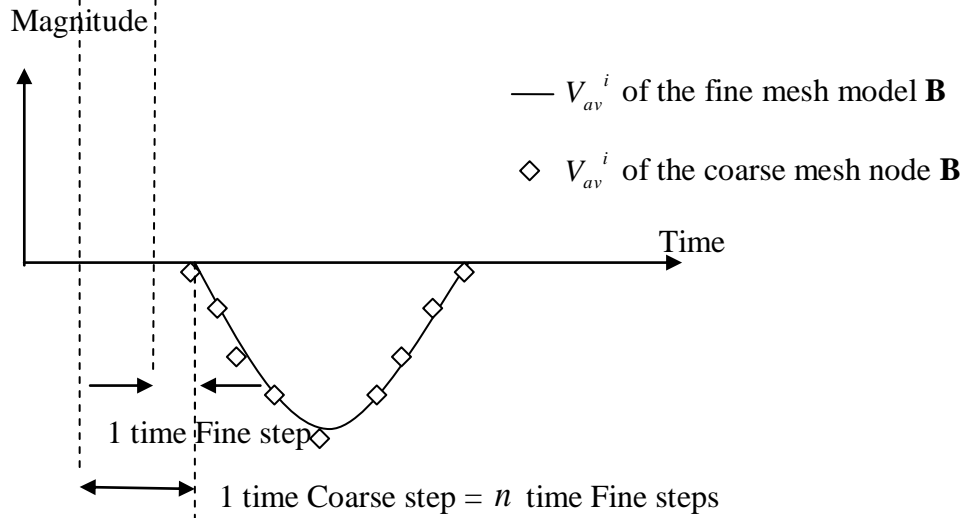
Fig.4.14 The result of time shift $n-1$ steps is new $V_{av}{}^i$ at the coarse mesh node B will be

the same as the fine mesh models B.

The explanation in this section implies that the frequency-dependent complex filter coefficients $F(s)$ for each DF transfer function require the time shift of the scattered voltage in order to obtain responses of the fine mesh and the coarse mesh TLM nodes synchronously.

4.3.2 Comparison of the results

To compare a fine mesh with a thin-wire model in Fig.4.3 and a DF coarse mesh node, a 3 mm x 3 mm x 5 mm thin-wire was embedded into a larger problem which contains long interconnects with a conduction post as shown in Fig. 4.15.
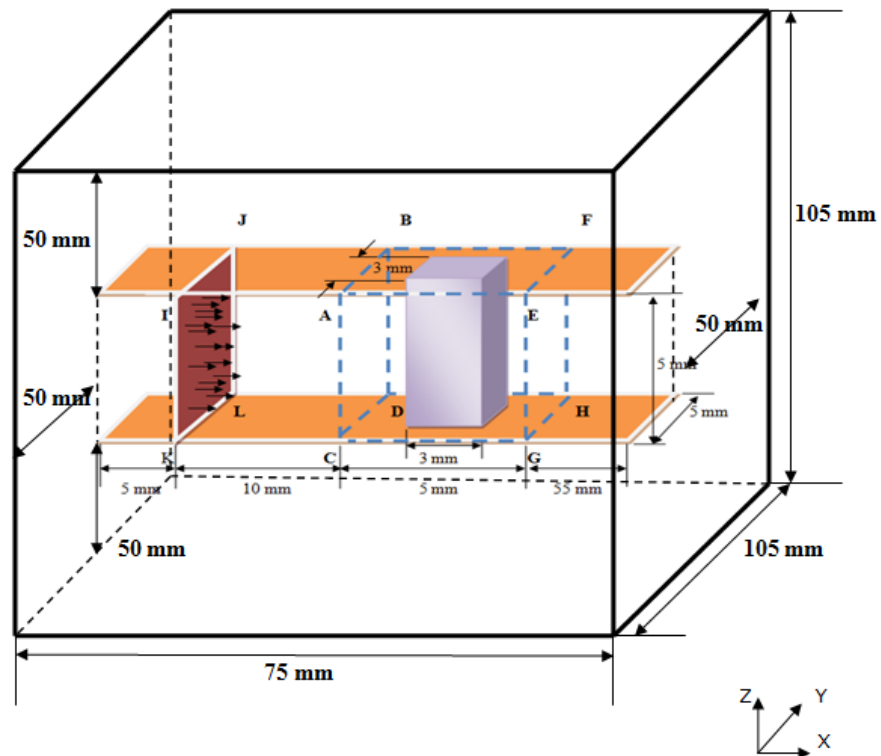
Fig.4.15 A matched boundaries box consists of a thin-wire of 3 mm x 3 mm x 5 mm placed between two long metal plates. The space step of the model is 1 mm.

The model in Fig.4.15 is a large box with a size of 75 mm x 105 mm x 105 mm. Its space-step is 1 mm $(\Delta l_f = 1mm)$ and all boundary conditions are matched. Moreover, the DF coarse mesh node, whose DF parameters are obtained by using three poles $(NP = 3)$ is placed between the two parallel metal plates at the same position as the thin-wire in the large coarse mesh model with a space step of 5 mm $(\Delta l_{DF} = 5mm)$ as shown in Fig. 4.16.
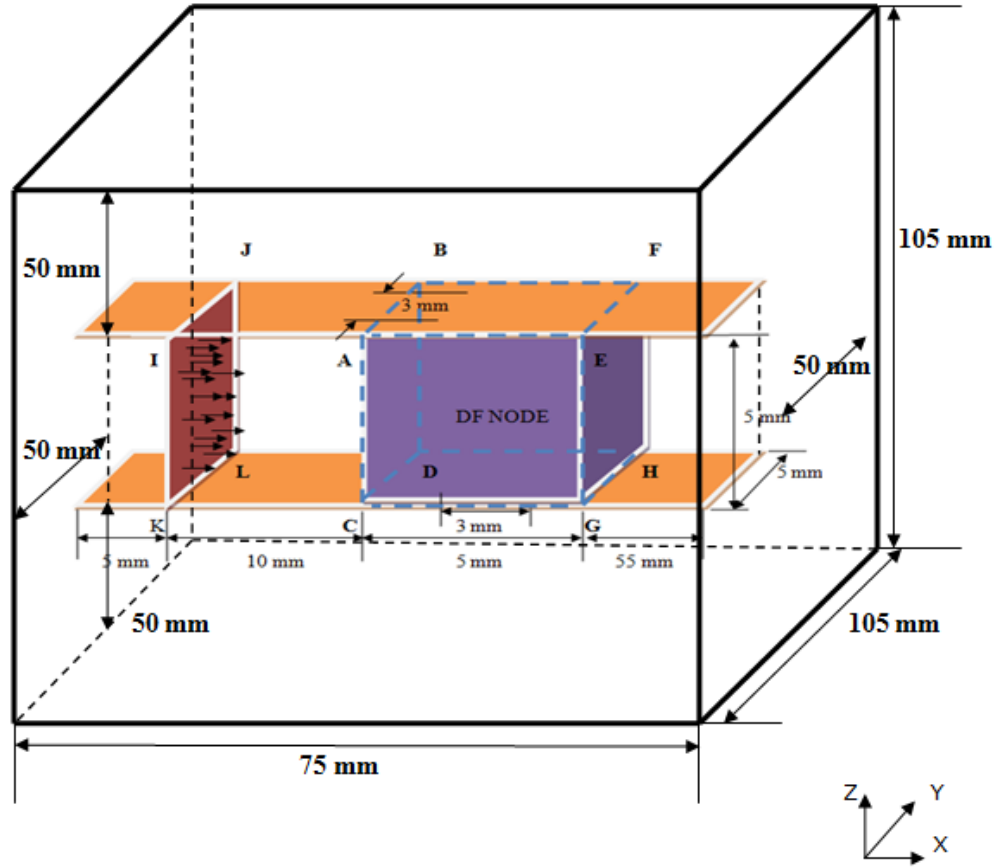
Fig.4.16 A matched boundaries box consists of a 5 mm x 5 mm x 5 mm DF node embedded between two long metal plates. The space step of the model is 5 mm.

Both models have the same voltage sources (red plane IJKL). They generate the same average input voltages of 1 V in the Gaussian form with a half-width of 0.2 ns at the IJKL plane. These input voltages are also excited between the nodes in the Z-direction with an X-directional propagation.

A comparison between the models shown in Fig. 4.15 and 4.16 can be made by observing the average output voltages as follows; (i) the average reflected voltage at the plane ABCD; (ii) the average transmitted forward voltages at the plane EFGH; (iii) the average transmitted voltage to the front at the plane AECG; (iv) the transmitted voltage to the back at the plane BFDH. These comparisons are shown in Fig.4.17-4.24 in both the time and frequency domains.
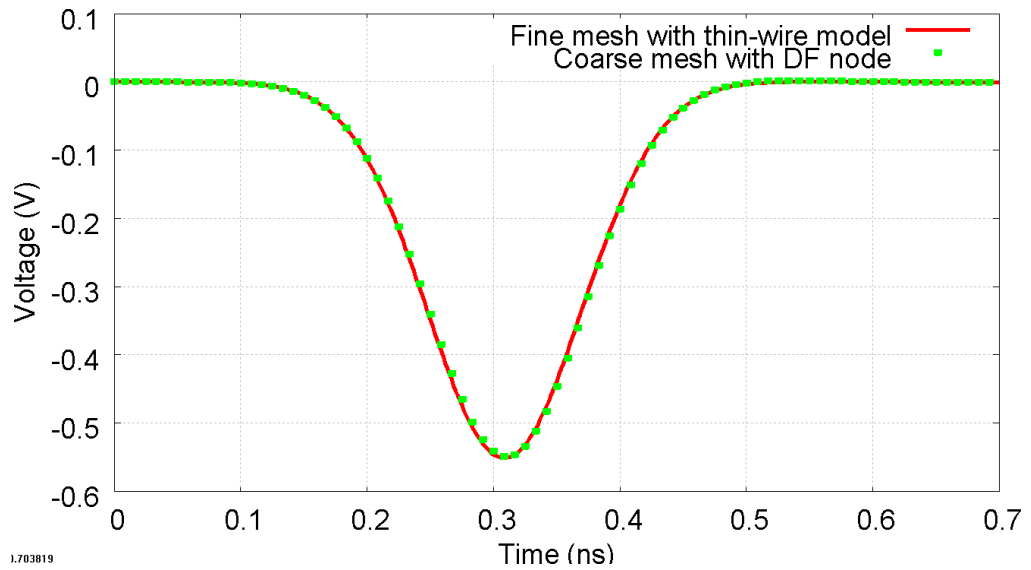
Fig.4.17 The time-domain average reflected voltages observed at the plane ABCD in the fine mesh with thin-wire model in Fig. 4.15 (red line) and the coarse mesh with DF node model in Fig.4.16 (green dot).

94
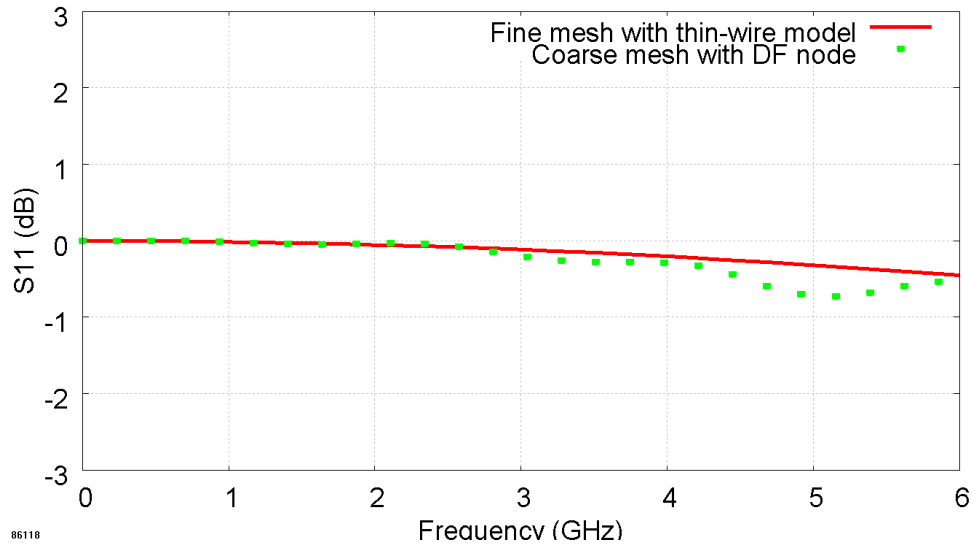
Fig.4.18 The frequency-domain average reflected voltages observed at the plane ABCD in the fine mesh with thin-wire model in Fig. 4.15 (red line) and the coarse mesh with DF node model in Fig.4.16 (green dot).
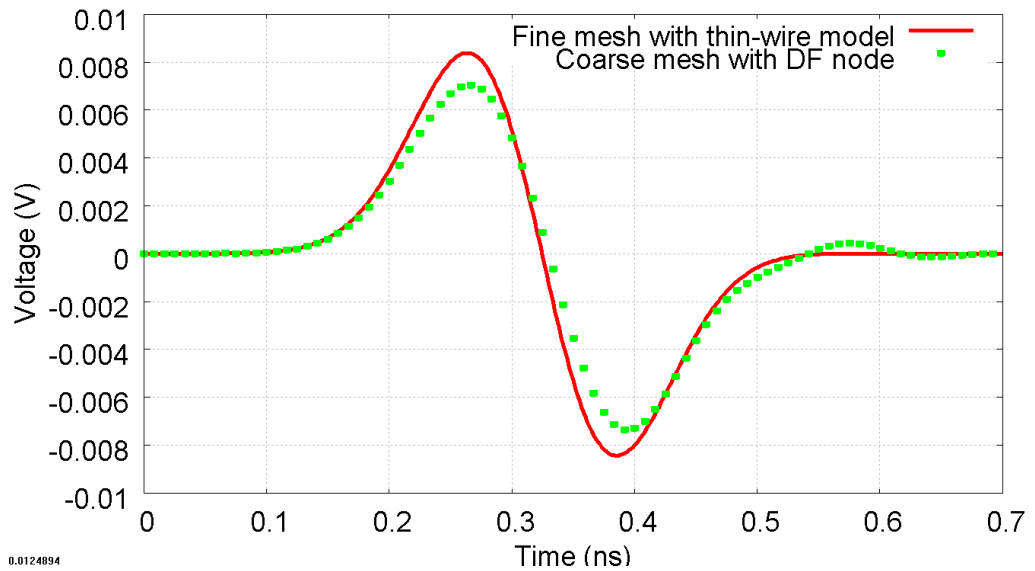
Fig.4.19 The time-domain average transmitted forward voltages observed at the plane EFGH in the fine mesh with thin-wire model in Fig. 4.15 (red line) and the coarse mesh with DF node model in Fig.4.16 (green dot).
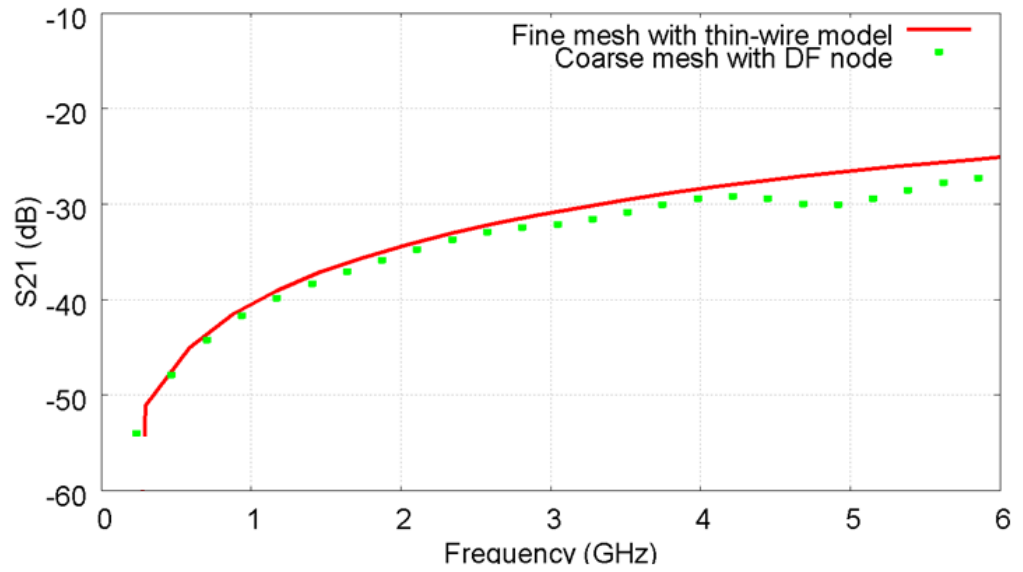
Fig.4.20 The frequency-domain average transmitted forward voltages observed at the plane EFGH in the fine mesh with thin-wire model in Fig. 4.15 (red line) and the coarse mesh with DF node model in Fig.4.16 (green dot).
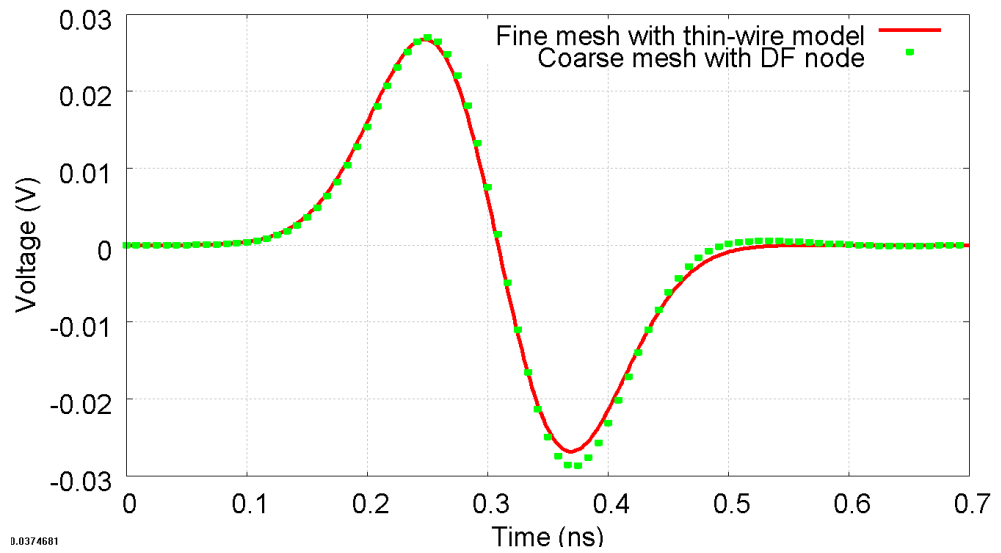
Fig.4.21 The time-domain average transmitted voltages to the front observed at the plane AECG in the fine mesh with thin-wire model in Fig. 4.15 (red line) and the coarse mesh with DF node model in Fig.4.16 (green dot).

96
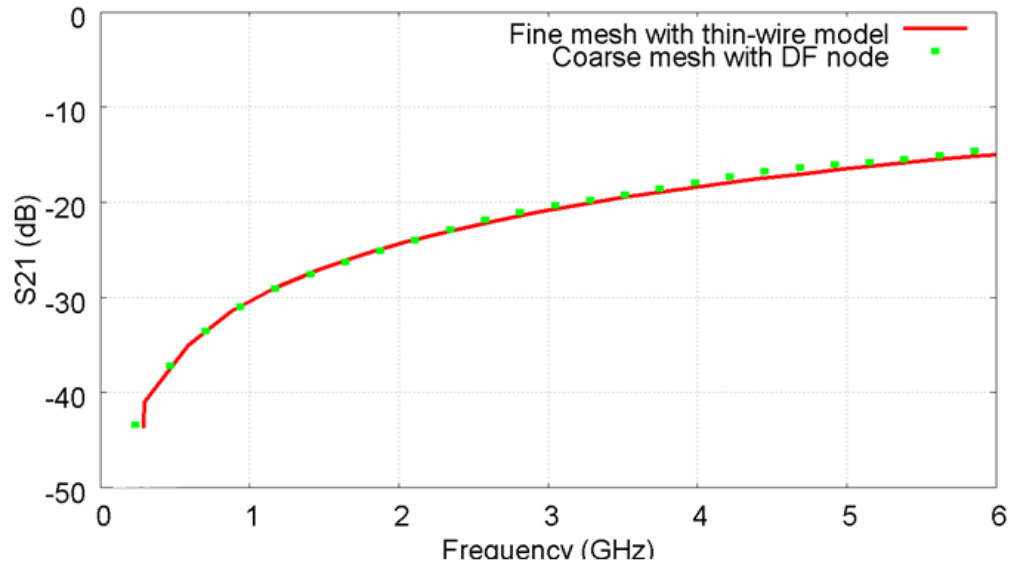
Fig.4.22 The frequency-domain average transmitted voltages to the front observed at the plane AECG in the fine mesh with thin-wire model in Fig. 4.15 (red line) and the coarse mesh with DF node model in Fig.4.16 (green dot).
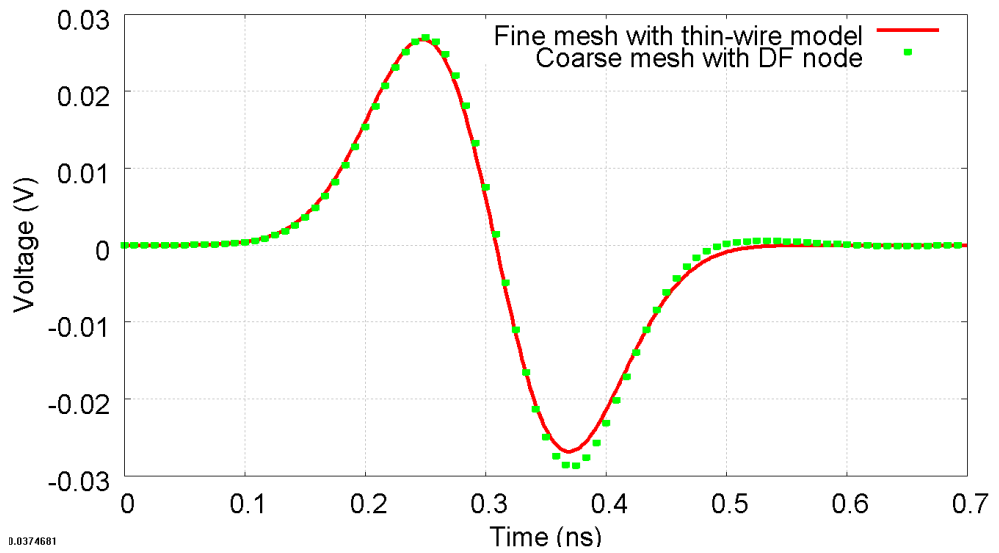
Fig.4.23 The time-domain average transmitted voltages to the back observed at the plane BFDH in the fine mesh with thin-wire model in Fig. 4.15 (red line) and the coarse mesh with DF node model in Fig.4.16 (green dot).
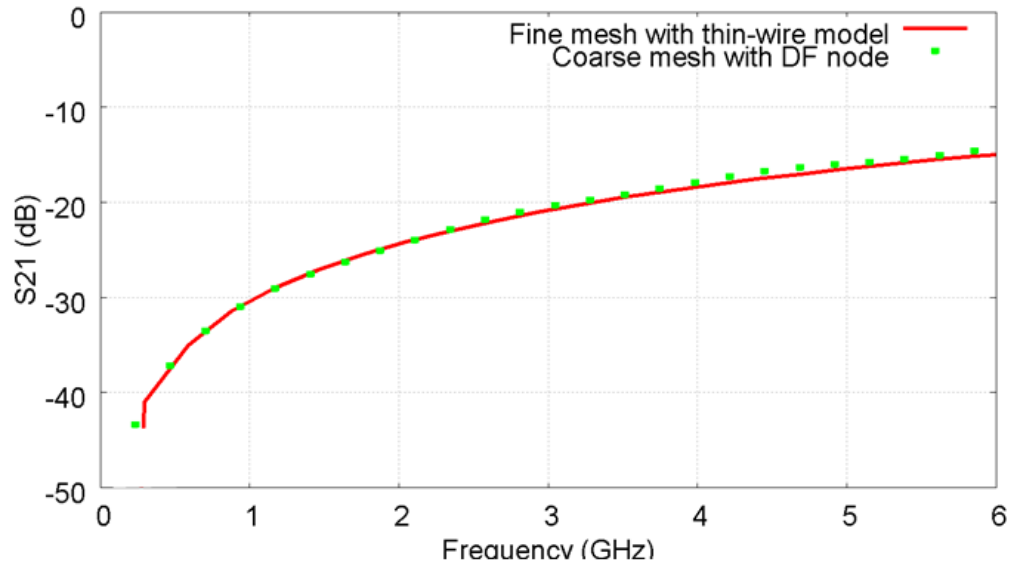
Fig.4.24 The frequency-domain average transmitted voltages to the back observed at the plane BFDH in the fine mesh with thin-wire model in Fig. 4.15 (red line) and the coarse mesh with DF node model in Fig.4.16 (green dot).

From Fig.4.17-4.24, the results obtained by employing the coarse mesh with the DF node model in Fig. 4.16 are close to the ones obtained by the fine mesh with a thin-wire in Fig. 4.15. The results agree up to 6 GHz, which is the limit for the coarse grid mesh dispersion.

Note that the results show that the average transmitted voltage to the back at the plane BFDH is the same as the one to the front at the plane AECG in the time and frequency domains, because of the symmetry of the matched boundary box.

The highest relative difference in the magnitude of the results can be found in Fig.4.19 because the magnitudes considered are very small. However, the absolute errors are still small, when compared with the 1 V excitation.

The computational requirements for both models are compared in Table 4.1.

TABLE 4.1

The comparison of computational requirements between two models in Fig.4.16 and 4.17.

Model	Number of nodes (NX)x(NY)x(NZ)	Number of time-steps	Memory (MB)	CPU Time (s)
Fine mesh with thin wire model $(\Delta l_f = 1mm)$	75 x 105 x 105	2048	156	567.62
Coarse mesh with DF node model $(\Delta l_{DF} = 5mm)$	15 x 21 x 21	512	48	6.24

The computer used for the TLM simulation has an Intel®Core ™ i7 CPU clocked at 1.60 GHz and an installed memory (RAM) of 4.00 GB.

Moreover, Fig.20 shows that the magnitude of the result obtained from the coarse mesh model with the DF node (green dots) swings after 3 GHz. Consequently, this produces the largest deviation in magnitude when compared with that of the fine mesh model (red line) at approximately 5 GHz. As mentioned, the DF node in this example is built using three poles $(NP = 3)$ and the number of samples used in determining the DF parameters from the fine mesh model in Fig.4.3 was around 200 $(NS = 200)$ containing the sampling points between 0-15 GHz. This result can be improved by recreating the DF node with an increased number of poles as shown in Fig.4.25.

-0.356104
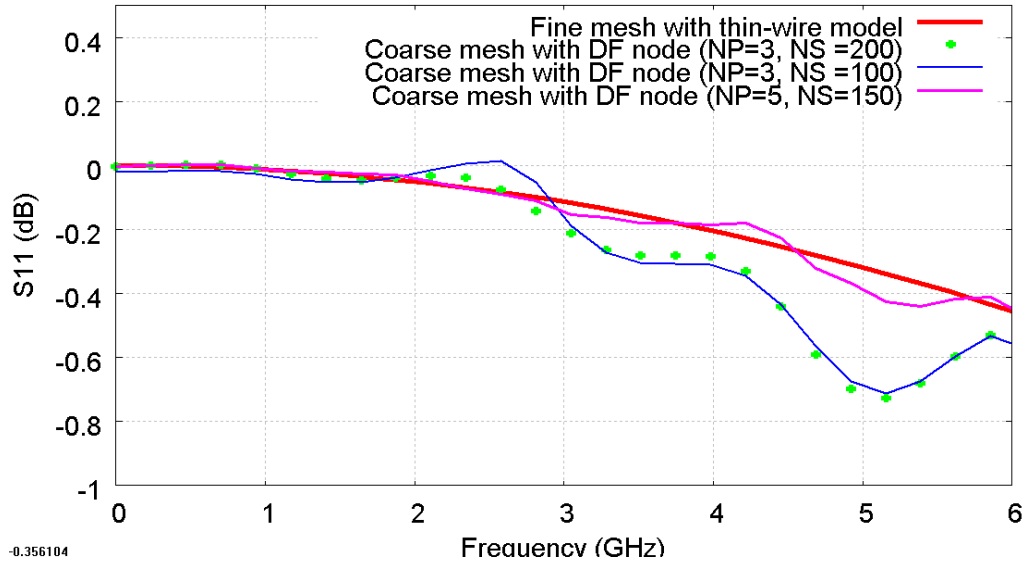
Fig.4.25 The diagram shows the reflected voltages obtained from a fine mesh model (red line) and coarse mesh with DF node models with different number of poles and sampling points for constructing the DF node.

In Fig.4.25, the results obtained from the fine mesh and the coarse mesh with the DF node $(NP = 3, NS = 200)$ models (red line and green dots) are the same as that shown in Fig. 4.18. The new result obtained from the coarse mesh with a new DF node $(NP = 3, NS = 100)$ (blue line) produces more swing and is worse than the result with the same number of poles but with a higher number of sampling points (green dots). Moreover, the new result with the higher number of poles $(NP = 5, NS = 150)$ (pink line) is better than the others when compared with the result obtained from the fine mesh model (red line). However, the model with the higher number of poles requires more memory and CPU time for the simulation (it requires 62MB in memory and 10.2s in simulation time).

4.4 Conclusion

This chapter has described the initial development of the DF technique. This technique can duplicate small three-dimensional structures and provide the electromagnetic properties for more than one dimension correctly. The main difference between this technique and the previous one described in chapter 3 is "the use of the time-shift" to determine the coefficients of the DF functions as described in section 4.3. The limitations and the conditions of this technique were also explained. These limitations can be minimised by further developments of the DF technique as shown in the next chapter. The demonstration of a thin-wire model in the three-dimensional model is used as an example to confirm the initial DF technique by comparing the results between a fine mesh thin-wire model and a coarse mesh DF node model as illustrated in Fig. 4.15 and 4.16 respectively. Moreover, the comparison of the computational requirements of both models in Table 4.1 show that the time and frequency results obtained by the coarse mesh DF node model require much lower requirements than that obtained by the fine mesh thin-wire model. This example also shows that selecting the number of poles (NP) affects the magnitude and the characteristics of the results. A higher number of poles produces better results but requires more computational effort.

The initial development of the DF technique applied to the three-dimensional TLM simulation can be summarised in Fig.4.26.
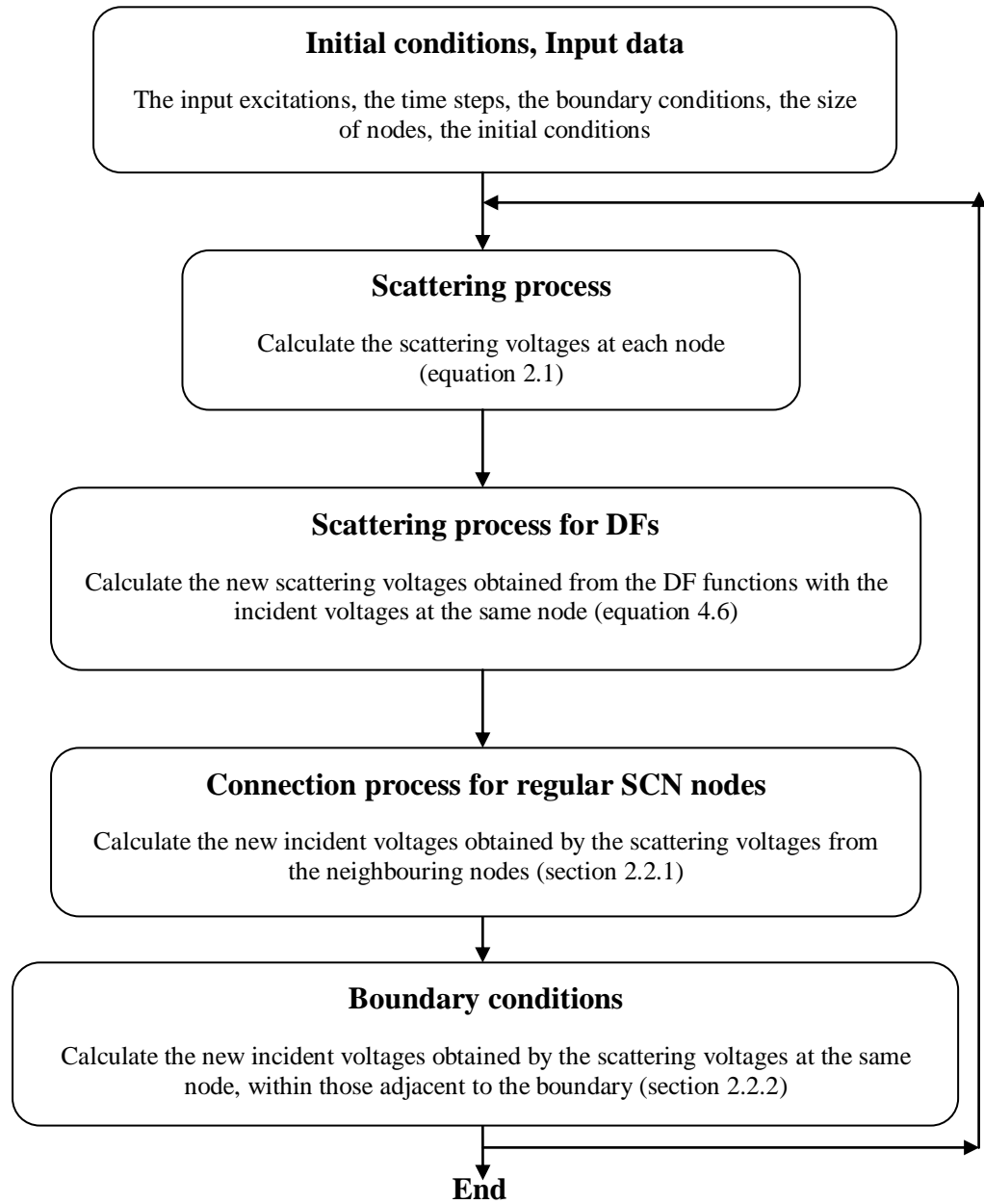
Fig.4.26 Schematic diagram of the computation procedure for the initial development DF technique applied with three-dimensional TLM simulation

4.5   References

[4.1]   S.M. Kay, Modern Spectral Estimation: Theory and Application, Prentice Hall, Englewood Cliffs, 1988.

[4.2]   R. J. Mulholland, J. R. Cruz and J. Hill, "State variable canonical forms for Prony's method", *Int. J. Systems Sci.*, vol. 17, pp. 55-64, 1986

[4.3]   J. N. Brittingham, E. K. Miller, and J. L. Willows, "Pole extraction from real-frequency information," *Proc. IEEE*, vol. 68, pp. 263-273, Feb. 1980.

[4.4]   J.-H. Lee and H.-T. Kim, "Selection of sampling interval for least squares Prony method", *Electron. Lett.*, vol. 41, pp. 47-49, Jan. 2005.

[4.5]   P. B. Johns, "A Symmetrical Condensed Node for the TLM Method," *IEEE Trans. Microwave Theory Tech.*, vol. 35, no. 4, pp. 370-377, Apr. 1987.

5 Further Development of the DF Technique

This chapter develops the initial DF technique in order to represent the three dimensional fine feature's properties and provide the electromagnetic fields in every dimension correctly. It also presents how DF nodes may be combined to represent a complicated fine feature spanning across a number of coarse nodes. Then, some simulation examples with comparisons in the frequency and the time domain with analytical results and associated computational requirements are demonstrated.

5.1 Introduction

The DF technique applied to the problem of an arbitrarily shaped object embedded into a three-dimensional TLM node requires consideration of the responses or the electromagnetic fields at all surfaces surrounding the object embedded in order to construct a coarse mesh DF node. The DF nodes can also be combined to represent a larger object as fully described in section 5.2.

As mentioned in the previous chapter, the object must be first modeled in a three-dimensional TLM fine mesh with the same cubical volume as the TLM coarse mesh node in order to construct the DF node from the relations given in

(4.1). The main advantage of the further DF technique is that it can be applied to any unknown object with the responses at the surface of the fine mesh required to create the DF node.

The DF node for this technique can be constructed by applying the similar procedures as given in chapter 4 but the responses from every surface of the fine mesh in the cube volume must be determined to estimate the coefficients for DF function. This also implies the condition that the fine feature must be placed between two metal surfaces, as used, in the initial DF technique is taken out. The procedure to obtain the DF node can be summarized in the following steps.

(i)   The DF parameters of a DF node are obtained by first accurately simulating the immediate region containing the object using a suitably fine mesh and extracting the time dependence of the scattering parameters from the surfaces surrounding the fine nodes representing the embedded objects.

(ii)   These time-dependent scattering parameters are then time-shifted as described in section 4.3.

(iii)   The frequency-dependent scattering parameters are then found by Fourier Transforming the time domain responses obtained from (ii) and subsequently applying the Prony's method to obtain the equivalent Poles and Zero's.

(iv)   These frequency-domain responses are then transformed by applying the bilinear Z-transform in order to obtain the DF parameters for the DF transfer functions $DF(\ )$.

(v)   As mentioned in chapter 2, a three-dimensional TLM scattering matrix s relates the vector of scattered voltages $\left(\vec{v}_{DF}{}^{r}\right)$ to the vector of incident voltages

$\left(\vec{V}_{DF}{}^{i}\right)$. As a result, the DF-node is constructed to relate between $\vec{V}_{DF}{}^{r}$ and $\vec{V}_{DF}{}^{i}$ with $DF(\ )$s in the form of a DF-node scattering matrix DFS as given by (4.6).

5.2 Demonstration of constructing a DF node for a fine embedded feature

To demonstrate the construction of a DF node for a fine embedded feature, a 3 mm x 3 mm x 3 mm metal conductor placed inside a cubical volume of 5 mm x 5 mm x 5mm with matched-boundary conditions as illustrated in Fig.5.1 is used as an example. Note that the RH side face of the conductor touches the volume boundary.
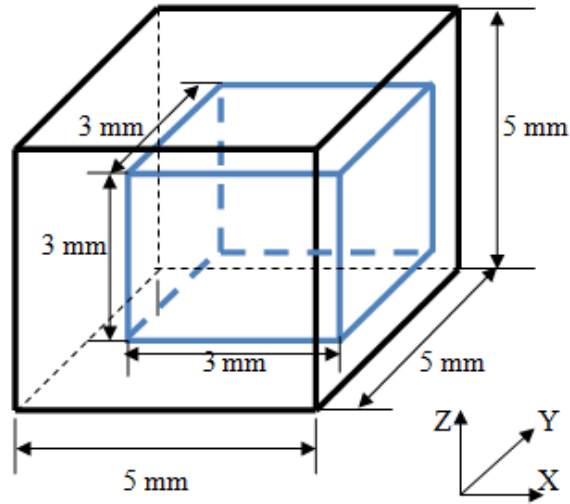
Fig.5.1 A 3 mm x 3 mm x 3 mm metal conductor placed inside the cubical volume of 5 mm x 5 mm x 5 mm with match-boundary condition. The space-step for this model is 1 mm $\left(\Delta l_{f} = 1mm\right).$

The model in Fig. 5.1 is excited by an average incident voltage $\left(\sum_n \sum_n V_f^i(n,n)/n\right)$ on the ABCD plane as illustrated in Fig. 5.2. Then, the average scattered voltages $\left(\sum_n \sum_n V_f^r(n,n)/n\right)$ can be determined by observing the average voltage at each boundary surface, ABCD, ABEF, AECG, CDGH and BFDH planes, except the boundary surface which touches the conductor—EFGH plane. Moreover, the DF parameters for each port in the DF node can be obtained from these voltages by following the steps described in section 5.1. Then, the scattering matrix DFS can be obtained by similarly exciting the remaining boundary surfaces in turn except the surface, which contains the conductor area.
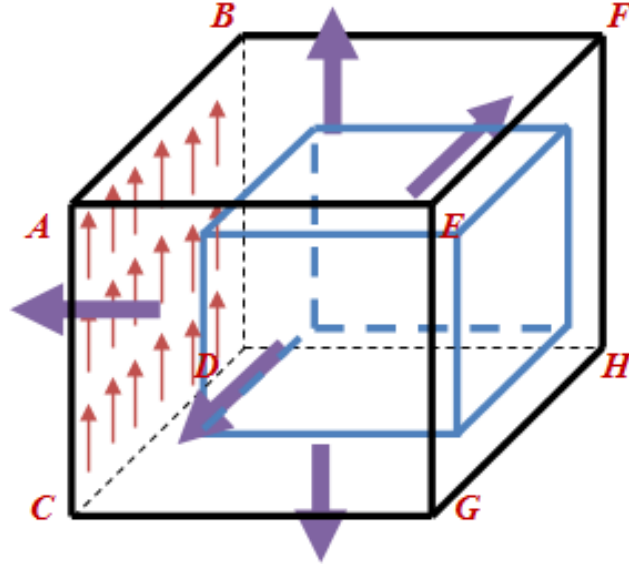
Fig.5.2 A fine mesh with metal conductor model is excited by an average incident voltage (red arrows on plane ABCD) to achieve the average scattered voltages (purple arrows) at each boundary surface except plane EFGH.

For the boundary face, which contains the conducting face (the EFGH plane), the average incident voltage is applied over the EFGH plane except the conducting area. Then, the average scattered voltages can be obtained by observing the average voltage on each boundary surface—ABCD, ABEF, AECG, CDGH and BFDH planes—except the EFGH plane as illustrated in Fig. 5.3.
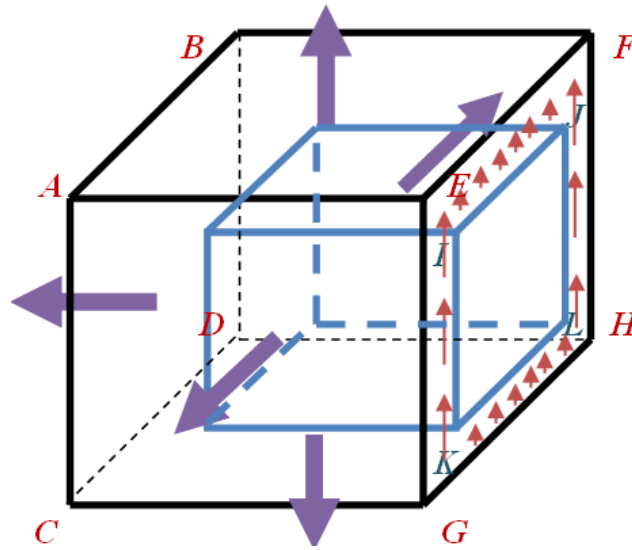
Fig.5.3 The boundary area containing the conductor face is excited by an average incident voltage (red arrows) to achieve the average scatted voltage (purple arrows) at each boundary surface except plane EFGH.

The average scattered voltages at plane EFGH are obtained differently from the others by first inserting an extra layer of TLM fine mesh nodes as shown in Fig. 5.4. Then, the average incident voltage is excited on the extended boundary area as usual, but the average scattered voltage is now obtained at plane E'F'G'H' instead of EFGH as illustrated in Fig.5.5.
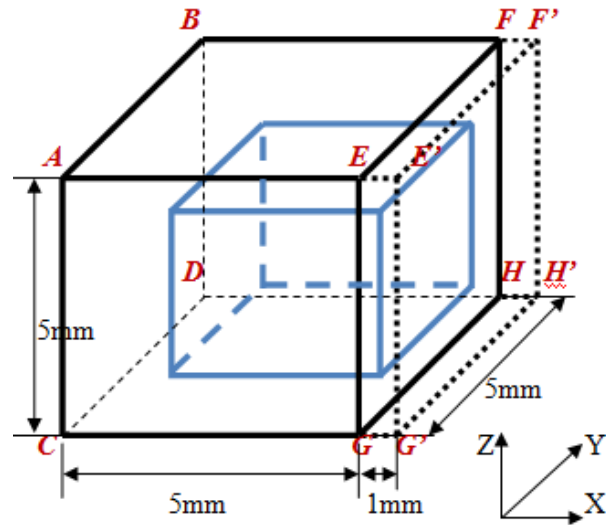
Fig.5.4 A fine mesh with metal conductor model has extra TLM nodes between planes EFGH and E'F'G'H'.
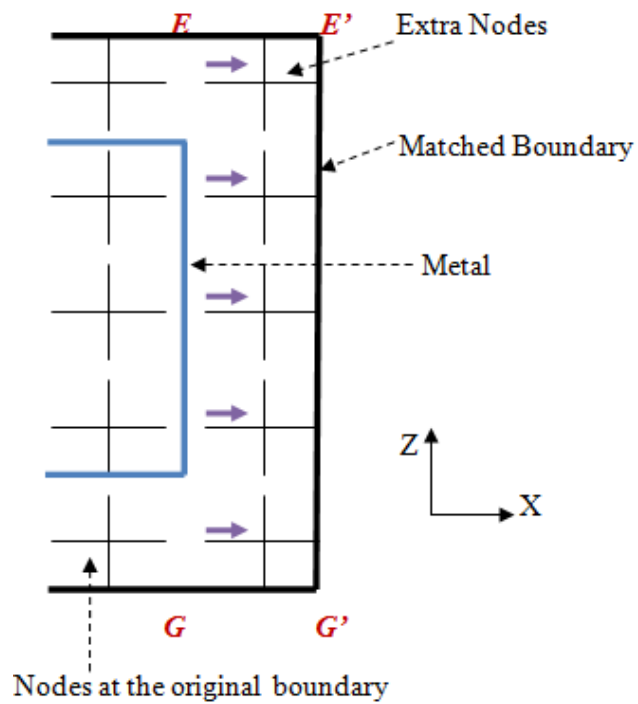
Fig.5.5 The extra TLM nodes between planes EFGH and E'F'G'H' observed in X and Z directions.

After all average scattered and incident voltages except the scattered voltages at plane EFGH are observed, they are substituted into (4.2) and (4.3) to obtain the scattered and incident voltages of the ports of the equivalent coarse DF node $\left(V_{DF}^r, V_{DF}^i\right)$ respectively. Then, these voltages are converted into the discrete frequency-domain $F(s)$ using (4.4). The average scattered and incident voltages at plane EFGH can be obtained from (5.1) and (4.3) respectively.

$$V_{DF}^r = \frac{\sum_n \sum_n V_f^{i\_extra}(n,n)}{n} \tag{5.1}$$

where i_extra indicates a port at the extra nodes. $F(s)$ for this case is given by (5.2).

$$F(s) = \frac{FFT\left[V_{DF}^r(k-n)\right]}{FFT\left[V_{DF}^i(k)\right]} \tag{5.2}$$

Note that, (5.1) and (5.2) are only used when the cubical volume's boundary surface coincides with the embedded metal conductor.

Then, $F(s)$ obtained from these voltages is substituted into the procedure outlined in (3.2)-(3.17) and (4.6). As a result, all the required parameters of the DF node are obtained from all the surfaces.

5.3   Examples of the connection of DF nodes

This section contains three simulation examples of the DF technique extension. (i) The first example is a metal conductor model. It shows that DF nodes can be combined to build up a more complicated model. (ii) The second example is a model of a silicon structure placed between two metal conductors. This example has a more complex configuration than the first example. The comparisons in the time and the frequency domains with analytical results are presented. (iii) The third example is a two-layer via model, which contains a dielectric substrate of ε_r between the layers. In addition, each layer is placed between conducting plates. There is also a conducting via, connected between top and bottom of the model, passed through a square hole between layers.

5.3.1 The first example

In this example, a 6 mm x 3 mm x 3 mm metal conductor placed inside a matched-boundary box of 10 mm x 5 mm x 5mm as illustrated in Fig. 5.6 is investigated.
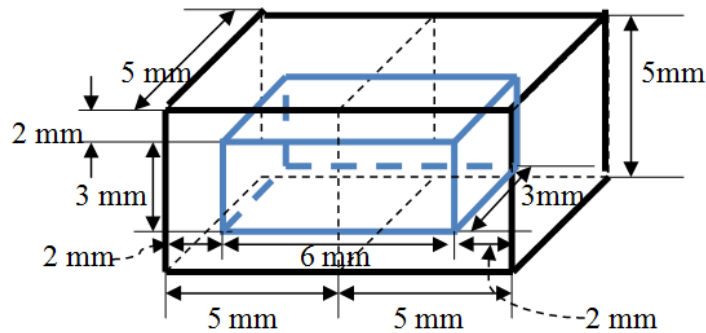
Fig.5.6 A TLM fine mesh with a 6 mm x 3 mm x 3 mm of metal conductor model. The space-step for this model is 1 mm $\left(\Delta l_f = 1mm\right).$

The model in Fig.5.6 can be also constructed by joining two TLM fine meshes—the metal conductor models in Fig.5.1 (LH side) and Fig.5.7 (RH side)—together.
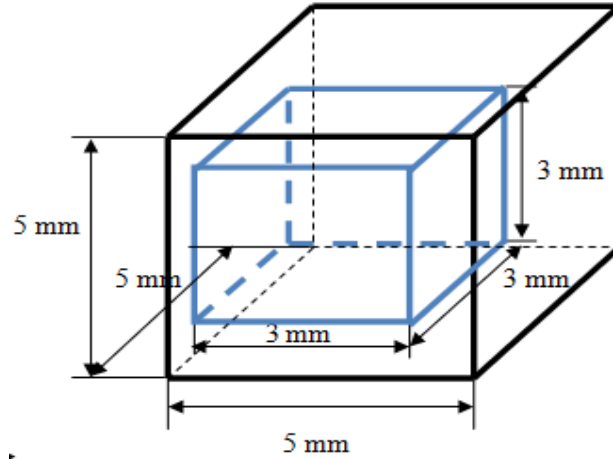
Fig.5.7 A 3 mm x 3 mm x 3 mm metal conductor placed inside the cubical volume of 5 mm x 5 mm x 5 mm with all match-boundary conditions. The space-step for this model is 1 mm $\left(\Delta l_f = 1mm\right)$.

The DF **A** and **B** nodes are constructed by applying this technique to the fine mesh metal conductor models shown in Fig. 5.1 and Fig. 5.7 respectively. Therefore, a TLM coarse mesh model combining the DF **A** node (LH side) and the DF **B** node (RH side) as illustrated in Fig. 5.8 can represent the same characteristics and properties of the TLM fine mesh metal conductor model in Fig. 5.6.
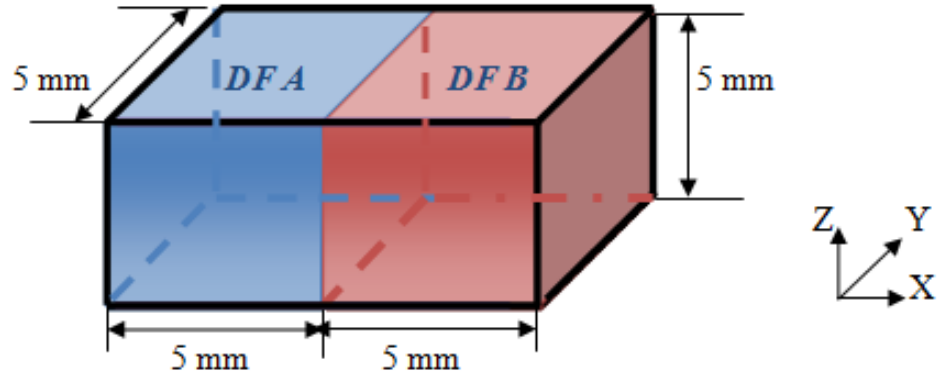
Fig.5.8 A TLM coarse mesh with DF A and B nodes model. The space-step for this model is 5 mm $\left(\Delta l_{DF} = 5mm\right)$.

5.3.2 Comparison of the results

To compare the TLM fine mesh with a metal conductor in Fig. 5.6 and the TLM coarse mesh with two joining DF nodes in Fig.5.8, a metal conductor of 6 mm x 3 mm x 3 mm is embedded into a 20 mm x 5 mm x 5 mm problem space with space step of 1 mm $\left(\Delta l_f = 1mm\right)$ as shown in Fig.5.9. The external boundaries conditions of this problem space are all matched. Furthermore, two DF nodes, DF A and B nodes, are constructed by the procedures described in the previous section. The DF A and B nodes represent the fine mesh with a metal conductor models as shown in Fig. 5.1 and Fig. 5.7 respectively. Consequently, the TLM coarse mesh with two joining DF nodes model is obtained as shown in Fig. 5.10.
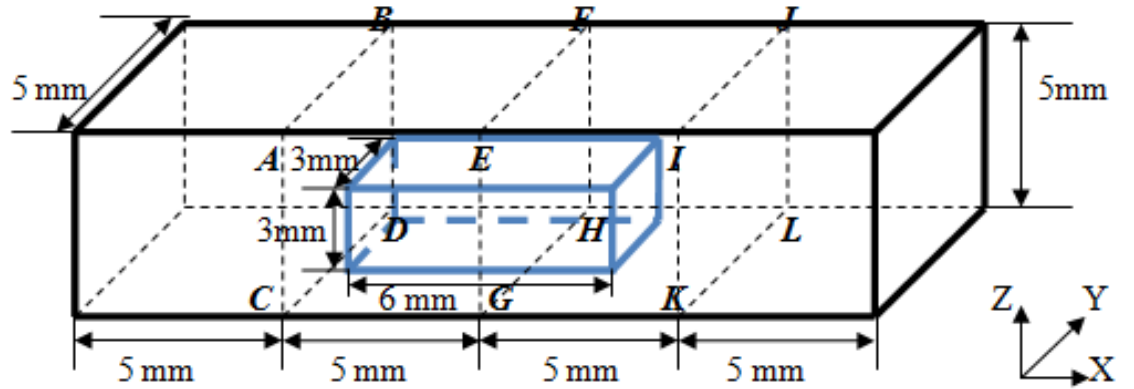
Fig.5.9 A TLM fine mesh with a 6 mm x 3 mm x 3 mm of metal conductor model. The space-step for this model is 1 mm $(\Delta l_f = 1mm)$.
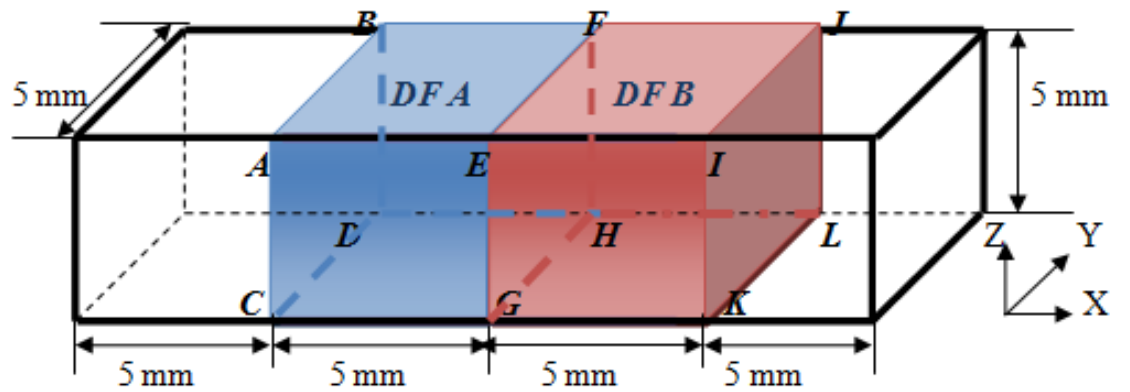
Fig.5.10 A TLM coarse mesh with DF A and B nodes model. The space-step for this model is 5 mm $(\Delta l_{DF} = 5mm)$.

The comparisons can be made by first exciting the average incident or input Y-directed voltage of 1 V with a Gaussian form with half-width of 0.35 ns at plane ABCD for both models (the positions X = 5 mm, Ymin-Ymax = 0 mm -5 mm and Zmin-Zmax = 0 mm - 5 mm) as shown in Fig. 5.11. The propagation is along X-direction. After that, the average scattering or output voltages are observed and compared between both models. These consist of;

(i)   The average reflected Y-directed voltages at the plane ABCD

(ii)   The average transmitted Y-directed voltages to the bottom
         boundary of the problem spaces at the plane CDGH

(iii)   The average transmitted Y-directed voltages to the top
         boundary of the problem spaces at the plane ABEF

(iv)   The average transmitted X-directed voltages to the front
         boundary of the problem spaces at the plane AECG

(v)   The average transmitted X-directed voltages to the back
         boundary of the problem spaces at the plane BFDH

(vi)   The average transmitted Y-directed voltages to the bottom
         boundary of the problem spaces at the plane GHKL

(vii)   The average transmitted Y-directed voltages to the top
         boundary of the problem spaces at the plane EFIJ

(viii)   The average transmitted X-directed voltages to the front
         boundary of the problem spaces at the plane EIGK

(ix)   The average transmitted X-directed voltages to the back
         boundary of the problem spaces at the plane FJHL

(x)   The average transmitted forward Y-directed voltages at the
         plane IJKL.

These comparisons are illustrated in Fig.5.12-5.31 in both the time and frequency domains.
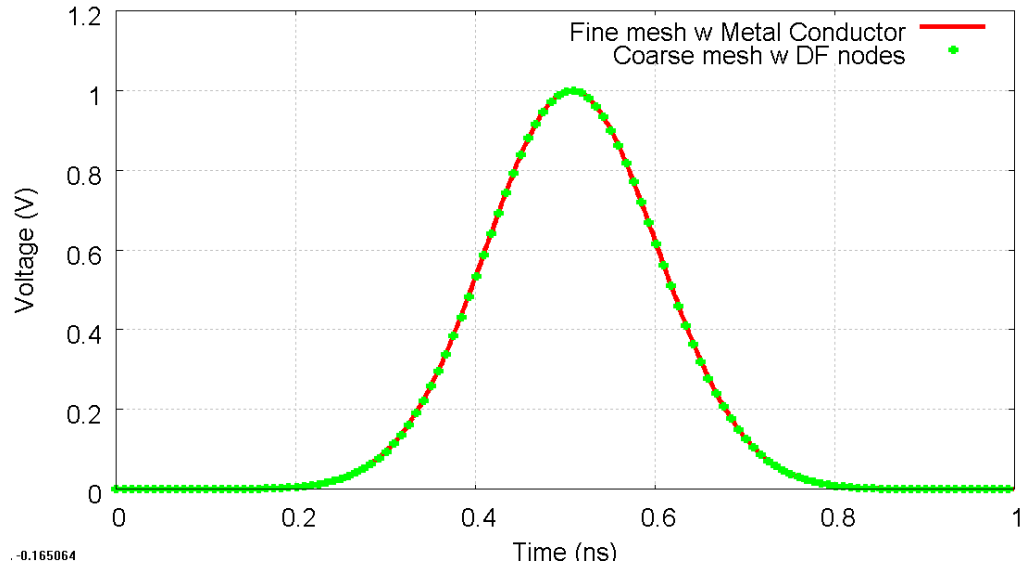
Fig.5.11 The time-domain average input Y-directed voltages at the plane ABCD.
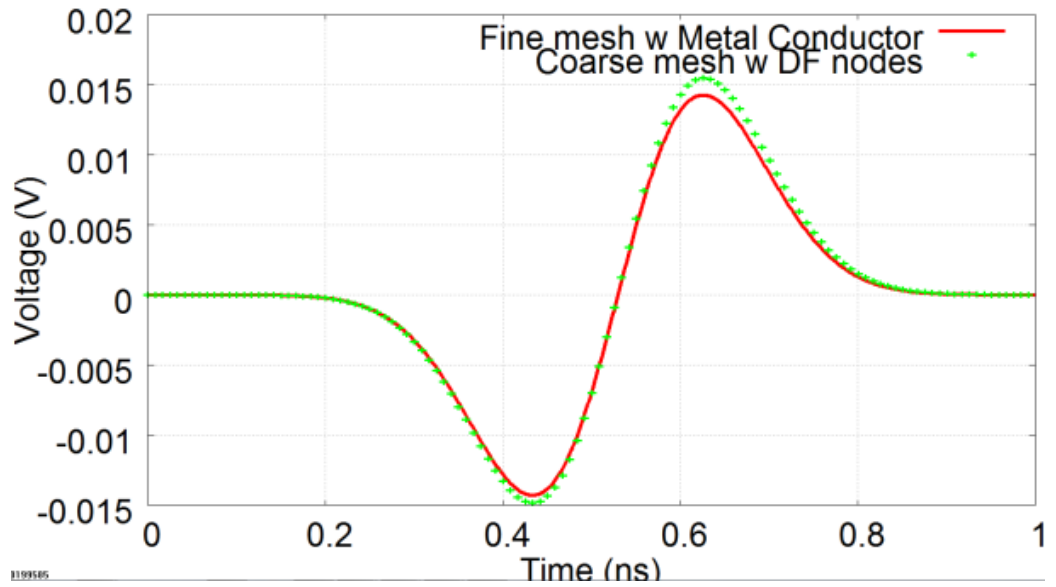
Fig.5.12 The time-domain average reflected Y-directed voltage at plane ABCD.

116
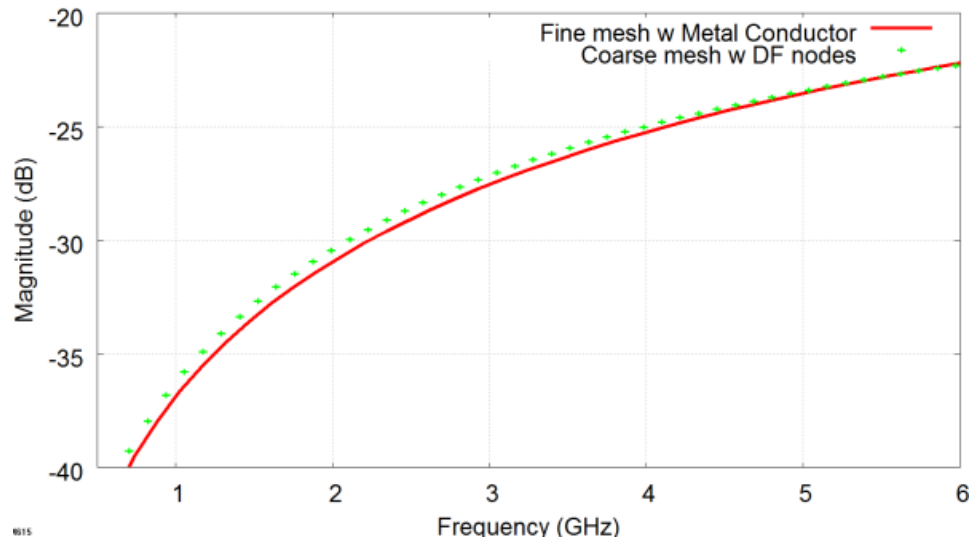
Fig.5.13 The frequency-domain average reflected Y-directed voltage at plane ABCD. Mean squared error (MSE) of the fine mesh with metal conductor model's result with respect the coarse mesh with DF nodes model's result between 0-6 GHz is 0.1687 dB.
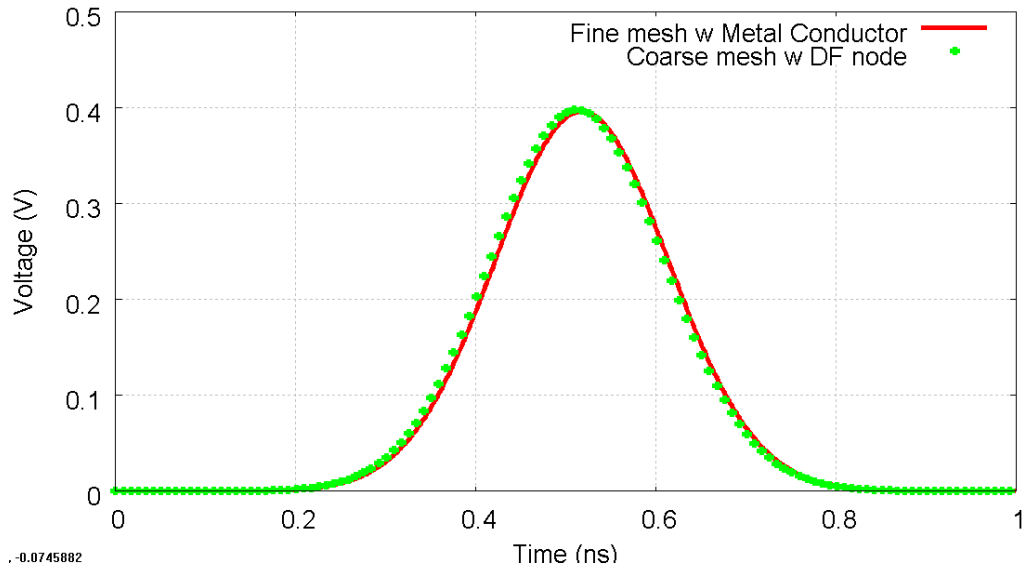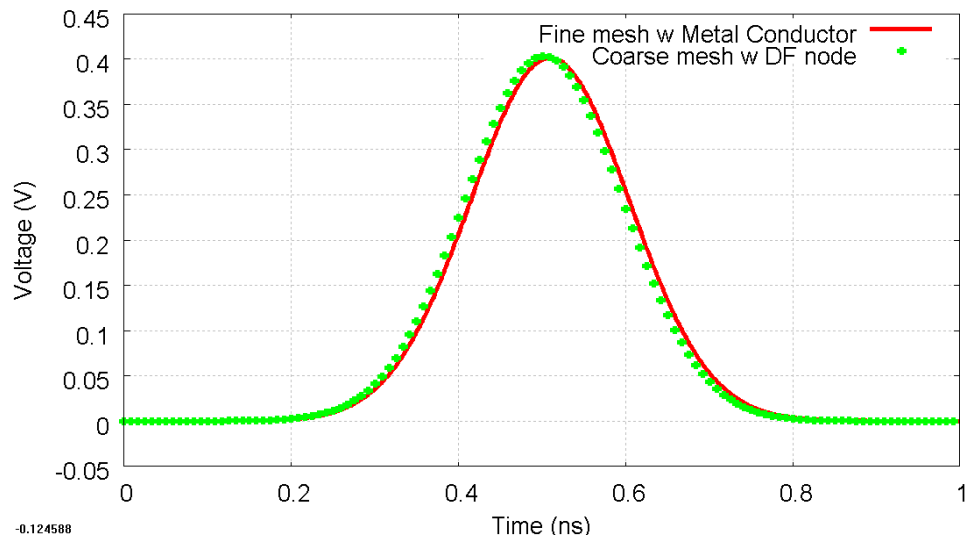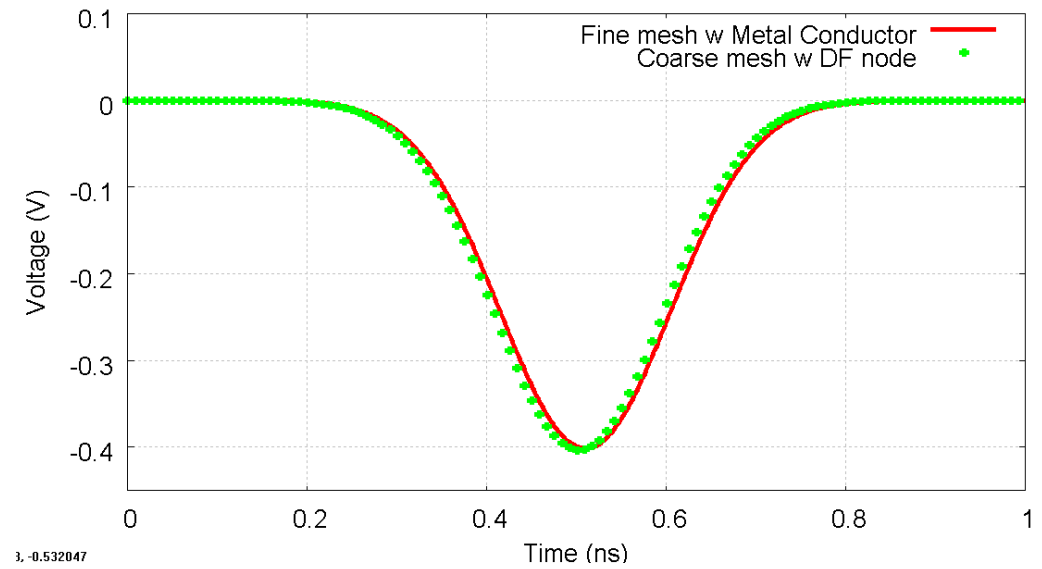

Fig.5.14 The time-domain average transmitted Y-directed voltages to the bottom boundary of the problem spaces at the plane CDGH.
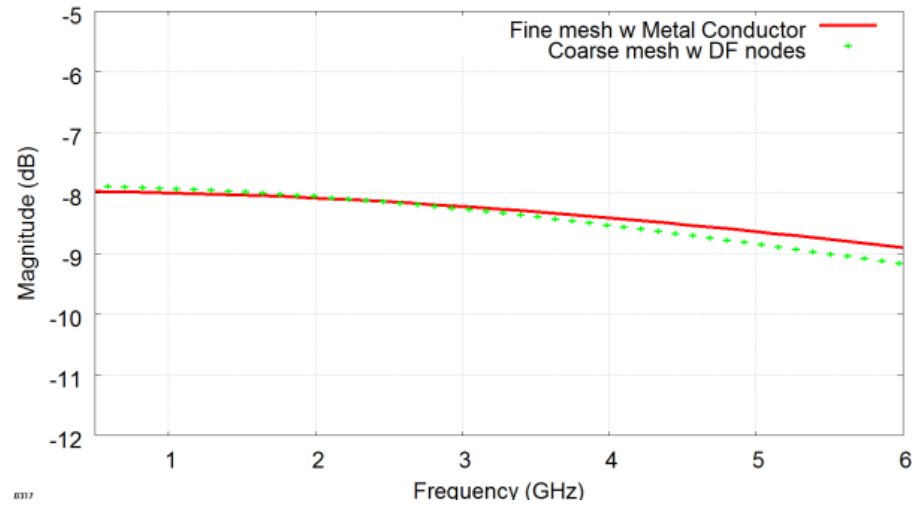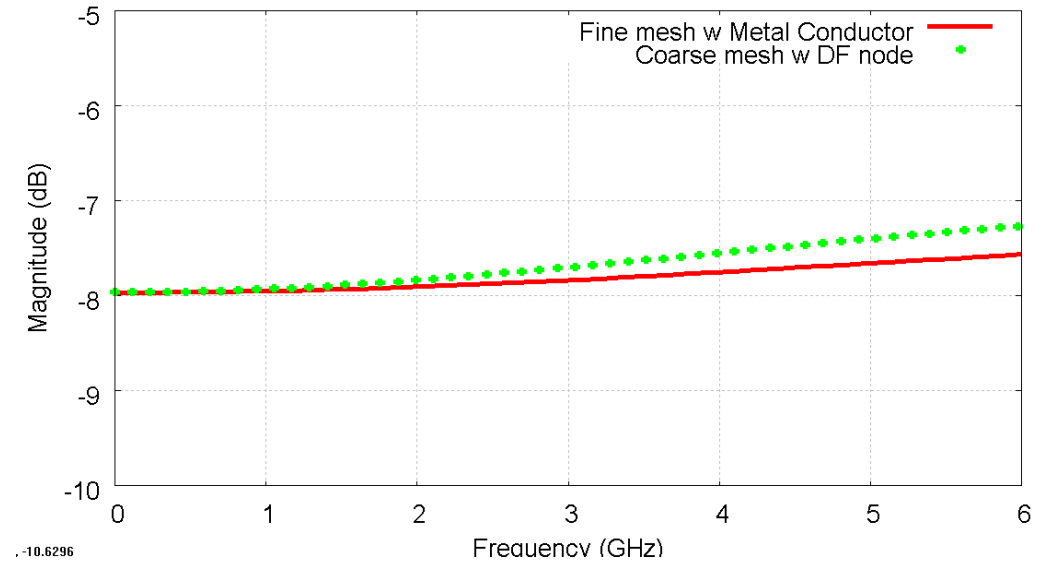
Fig.5.15The The frequency-domain average transmitted Y-directed voltages to the bottom boundary of the problem spaces at the plane CDGH. Mean squared error (MSE) of the fine mesh with metal conductor model's result with respect the coarse mesh with DF nodes model's result between 0-6 GHz is 0.019 dB.
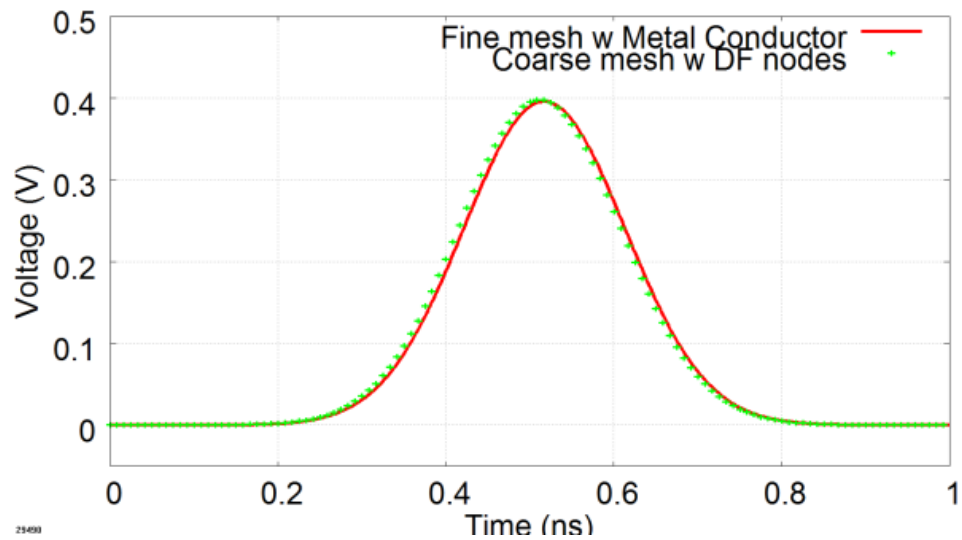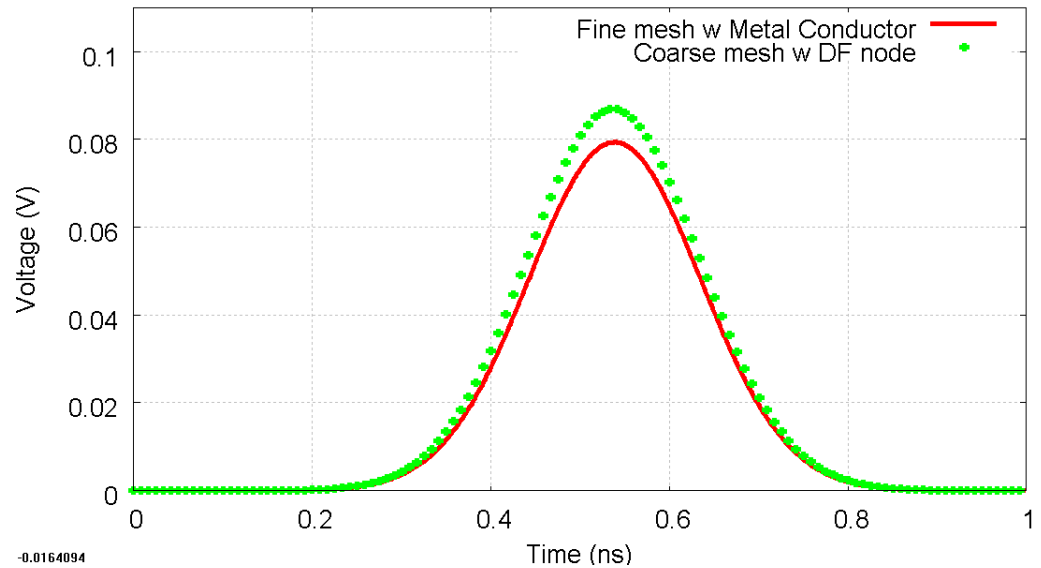

Fig.5.16 The time-domain average transmitted Y-directed voltages to the top boundary of the problem spaces at the plane ABEF.
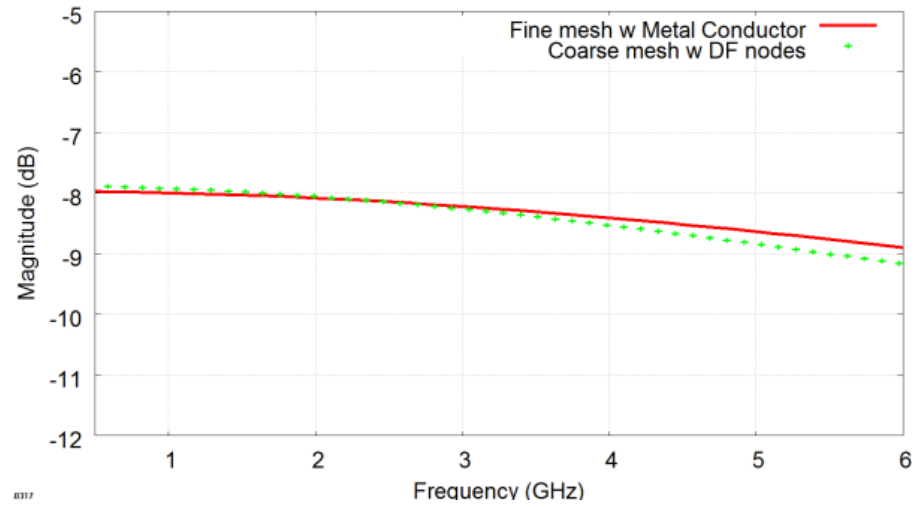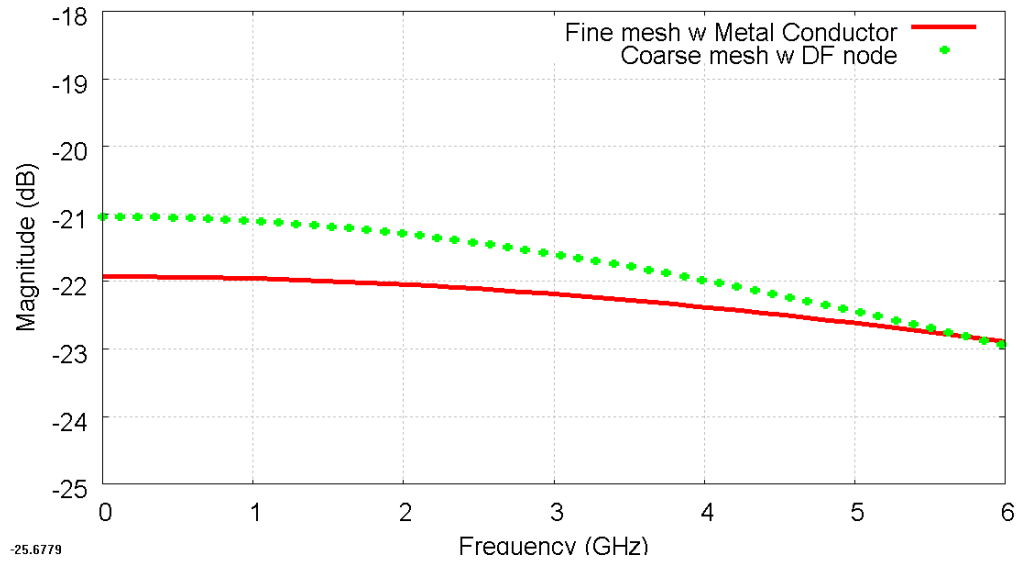
Fig.5.17 The frequency-domain average transmitted Y-directed voltages to the top boundary of the problem spaces at the plane ABEF. Mean squared error (MSE) of the fine mesh with metal conductor model's result with respect the coarse mesh with DF nodes model's result between 0-6 GHz is 0.019 dB.
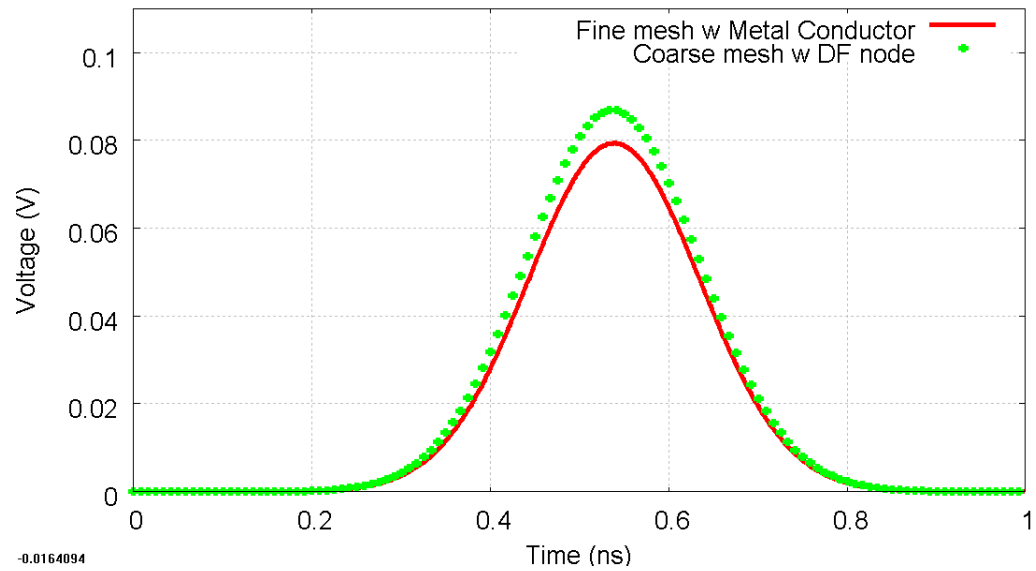

Fig.5.18 The time-domain average transmitted X-directed voltages to the front boundary of the problem spaces at the plane AECG.
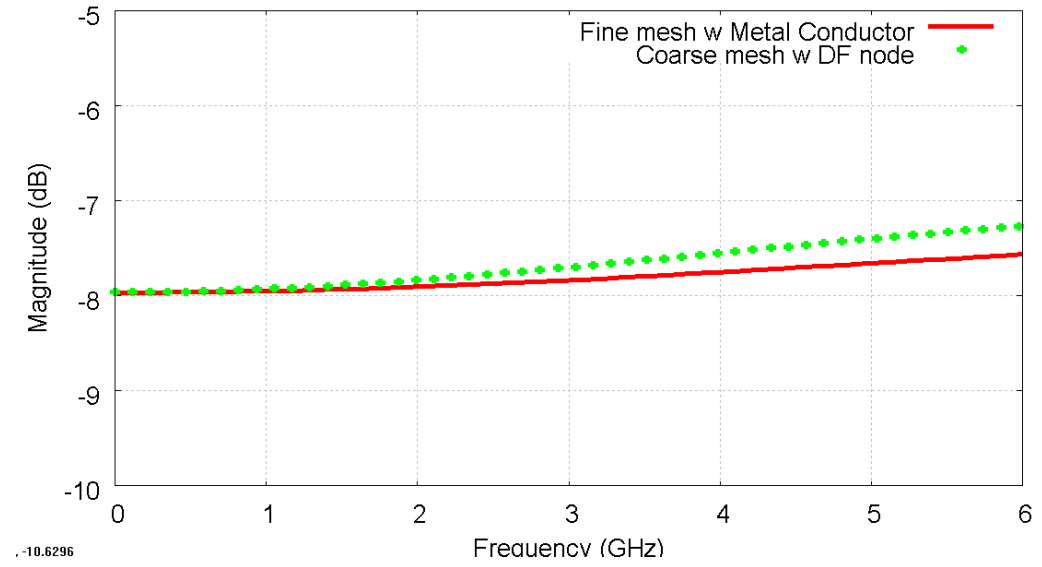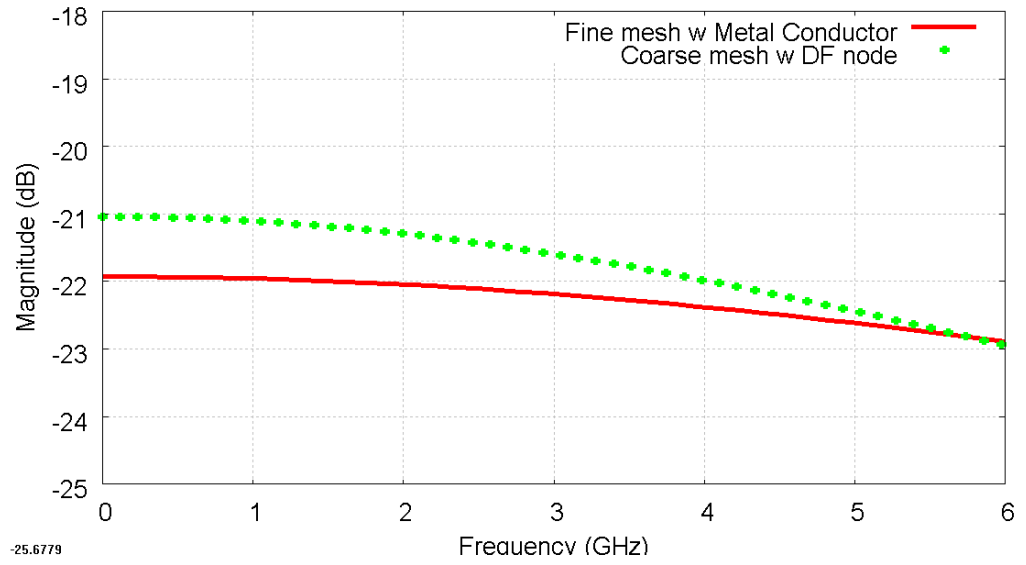
Fig.5.19 The frequency-domain average transmitted X-directed voltages to the front boundary of the problem spaces at the plane AECG. Mean squared error (MSE) of the fine mesh with metal conductor model's result with respect the coarse mesh with DF nodes model's result between 0-6 GHz is 0.0325 dB.

Fig.5.20 The time-domain average transmitted X-directed voltages to the back boundary of the problem spaces at the plane BFDH.

Fig.5.21 The frequency-domain average transmitted X-directed voltages to the back boundary of the problem spaces at the plane BFDH. Mean squared error (MSE) of the fine mesh with metal conductor model's result with respect the coarse mesh with DF nodes model's result between 0-6 GHz is 0.0325 dB.
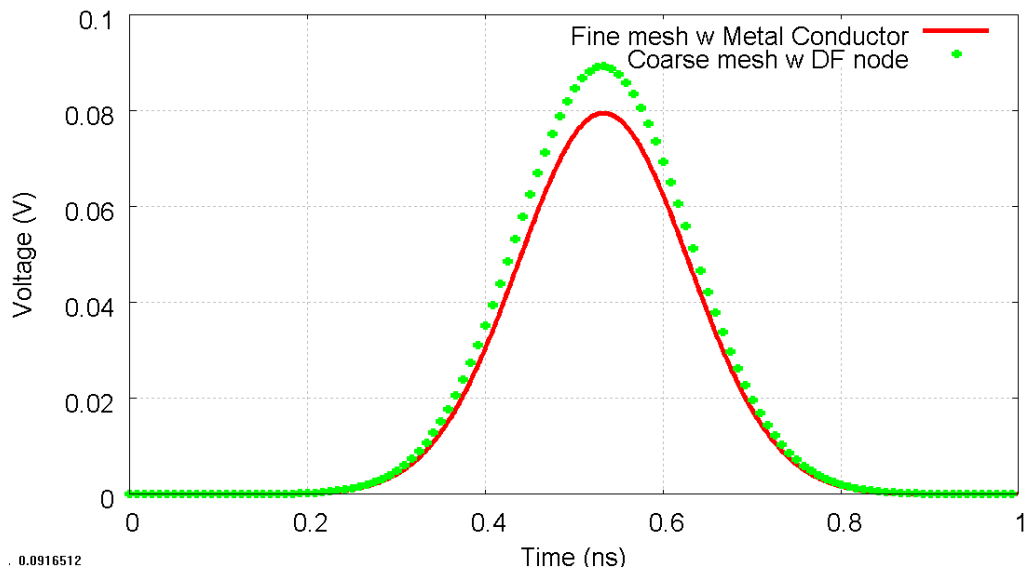

Fig.5.22 The time-domain average transmitted Y-directed voltages to the bottom boundary of the problem spaces at the plane GHKL.
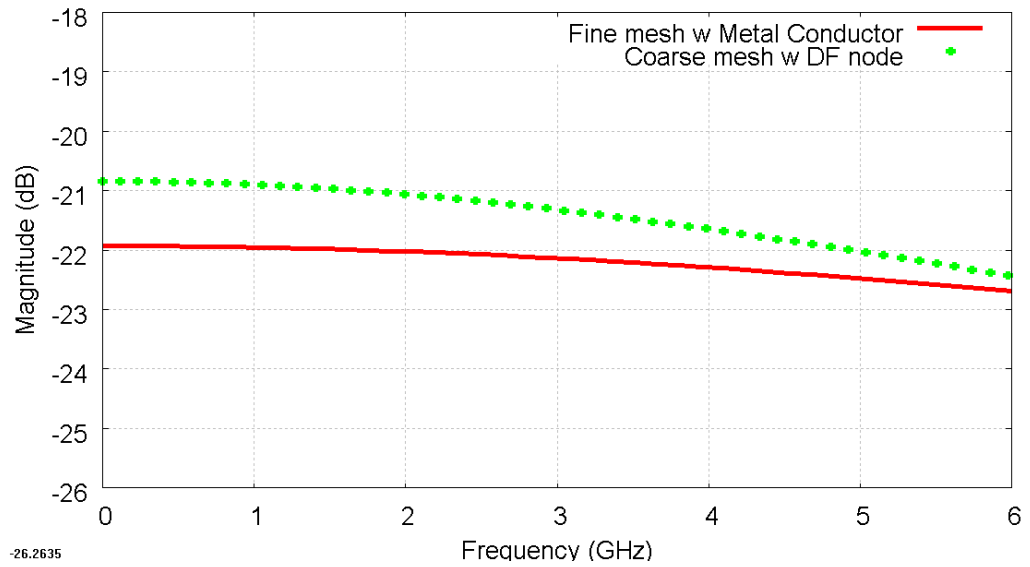
Fig.5.23 The frequency-domain average transmitted Y-directed voltages to the bottom boundary of the problem spaces at the plane GHKL. Mean squared error (MSE) of the fine mesh with metal conductor model's result with respect the coarse mesh with DF nodes model's result between 0-6 GHz is 0.3404 dB.

Fig.5.24 The time-domain average transmitted Y-directed voltages to the top boundary of the problem spaces at the plane EFIJ.

Fig.5.25 The frequency-domain average transmitted Y-directed voltages to the top boundary of the problem spaces at the plane EFIJ. Mean squared error (MSE) of the fine mesh with metal conductor model's result with respect the coarse mesh with DF nodes model's result between 0-6 GHz is 0.3404 dB.
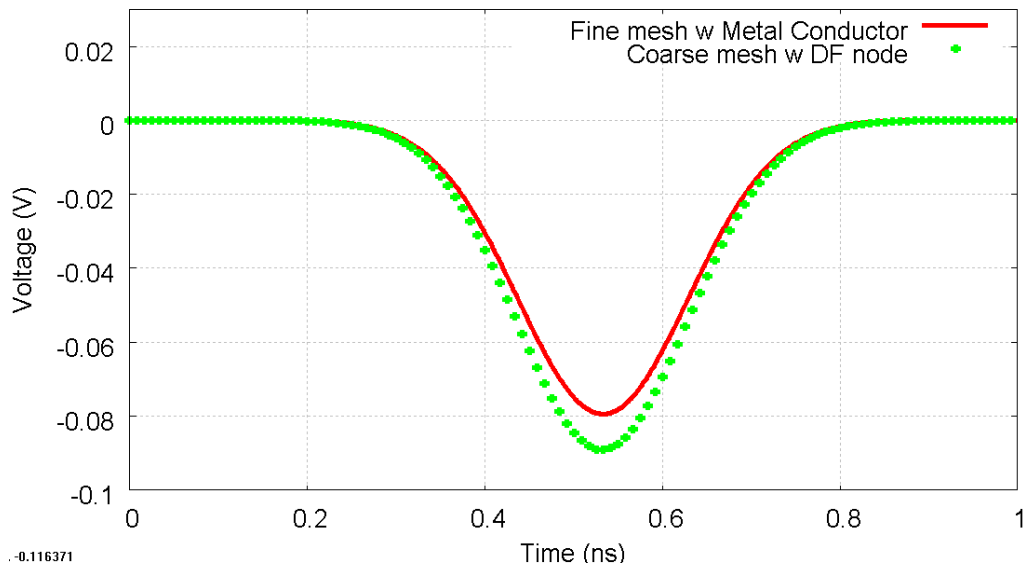

Fig.5.26 The time-domain average transmitted Y-directed voltages to the front boundary of the problem spaces at the plane EIGK.

Fig.5.27 The frequency-domain average transmitted Y-directed voltages to the front boundary of the problem spaces at the plane EIGK. Mean squared error (MSE) of the fine mesh with metal conductor model's result with respect the coarse mesh with DF nodes model's result between 0-6 GHz is 0.6187 dB.

Fig.5.28 The time-domain average transmitted Y-directed voltages to the back boundary of the problem spaces at the plane FJHL.
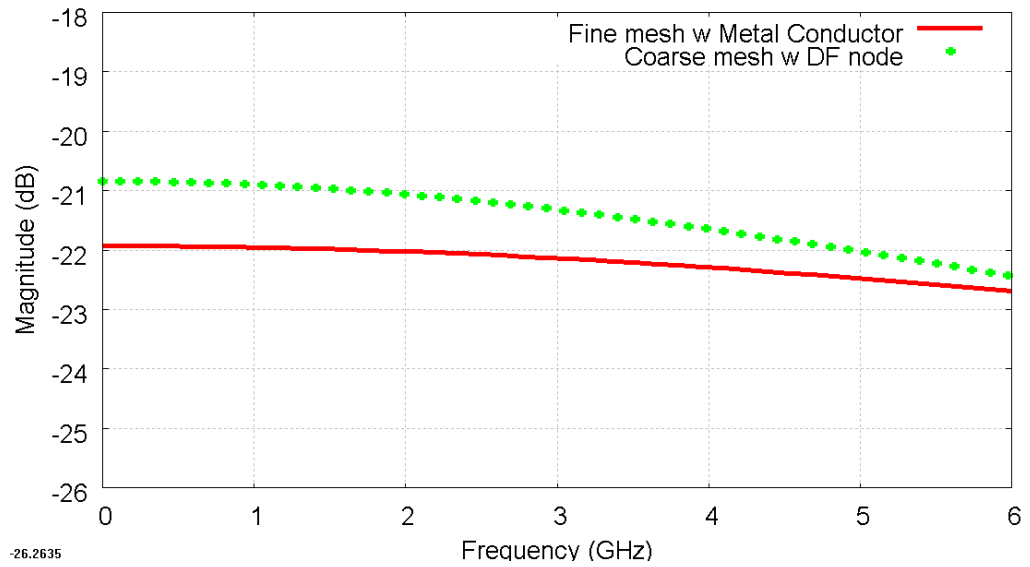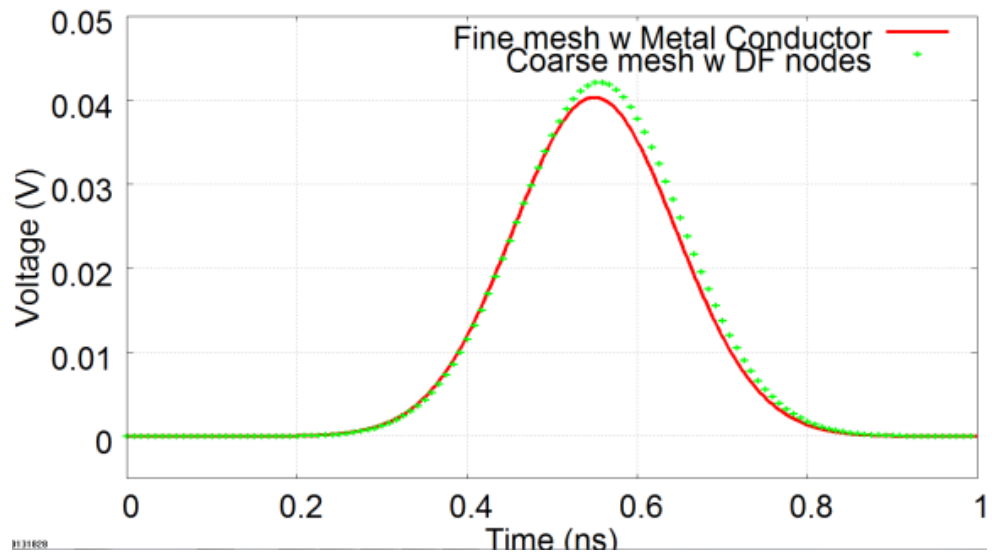
124

-26.2635

Fig.5.29 The frequency-domain average transmitted Y-directed voltages to the back boundary of the problem spaces at the plane FJHL. Mean squared error (MSE) of the fine mesh with metal conductor model's result with respect the coarse mesh with DF nodes model's result between 0-6 GHz is 0.6187 dB.

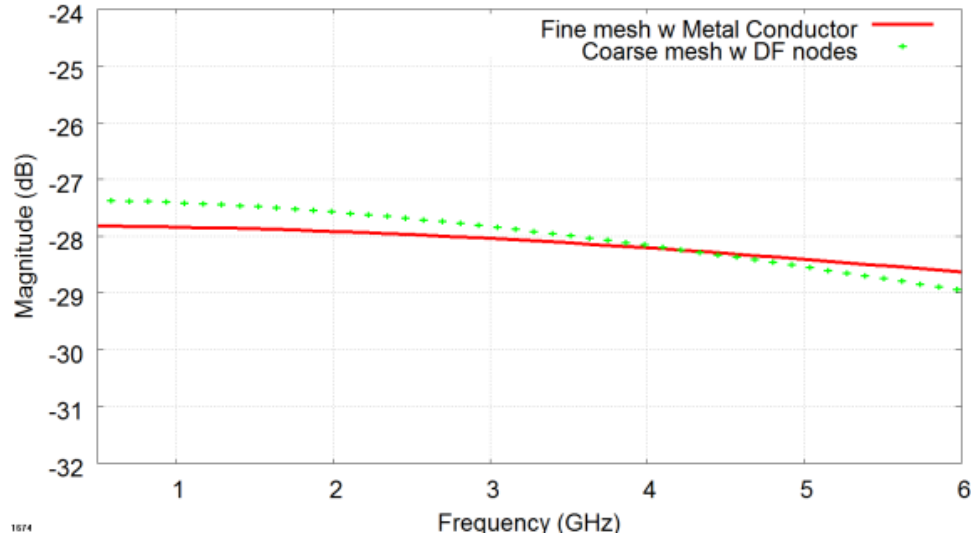**Fig.5.30 The time-domain average transmitted forward Y-directed voltage at plane IJKL.**

125

Fig.5.31 The frequency-domain average transmitted forward Y-directed voltage at plane IJKL. Mean squared error (MSE) of the fine mesh with metal conductor model's result with respect the coarse mesh with DF nodes model's result between 0-6 GHz is 0.0800 dB.

In Fig.5.12-5.31, the mean squared error (MSE) and the maximum error are used to quantify the differences between the frequency-domain results of the two methods. Along with the maximum error, MSE provides a measure of the error distribution. The highest value of MSE between the two methods was found to be 0.6187 dB, which is a small value, in Fig.5.27 and Fig. 5.29. Consequently, the results show a good agreement between the two methods. The highest difference in relative magnitude of the frequency-domain results is 1 dB approximately as illustrated in Fig. 5.23, Fig. 5.25, Fig. 5.27 and Fig. 5.29 Moreover, the maximum frequency, given by the coarse mesh dispersion, for the comparison between two methods is 6 GHz.

The relative difference in magnitude of the time-domain results can be found obviously in Fig.5.24 and Fig.5.26 which is because these magnitudes are very small but absolute errors are still small compared with 1 V excitation.

The computational requirements of the two methods are compared as shown in Table5.1.

TABLE 5.1

The comparison of the computational requirements between two models in Fig.5.9 and 5.10.

Model	Number of nodes (NX)x(NY)x(NZ)	Number of time-steps	Memory (kB)	CPU Time (s)
Fine mesh with a metal conductor model $(\Delta l_f = 1mm)$	20 x 5 x 5	4096	1228	3.05
Coarse mesh with the DF nodes model $(\Delta l_{DF} = 5mm)$	4 x 1 x 1	1024	672	0.67

The computer used for the TLM simulation has Intel®Core ™ i7 CPU processor with 1.60 GHz and installed memory (RAM) of 4.00 GB.

5.3.3 Second example

The second example involves a more complex configuration. The example model is a 3 mm x 5 mm x 15 mm (thickness x width x height) silicon block placed in a problem space of 15 mm x 5 mm x 15 mm, with a space step of 1 mm $(\Delta l_f = 1\,\text{mm})$, PEC boundary conditions at the top and bottom of the model (Zmin-Zmax), open-circuit boundary conditions for Ymin-Ymax and matched boundary conditions for Xmin-Xmax, as shown in Fig.5.32. The relative permittivity ε_r of of this silicon block is 15.68 [5.1].
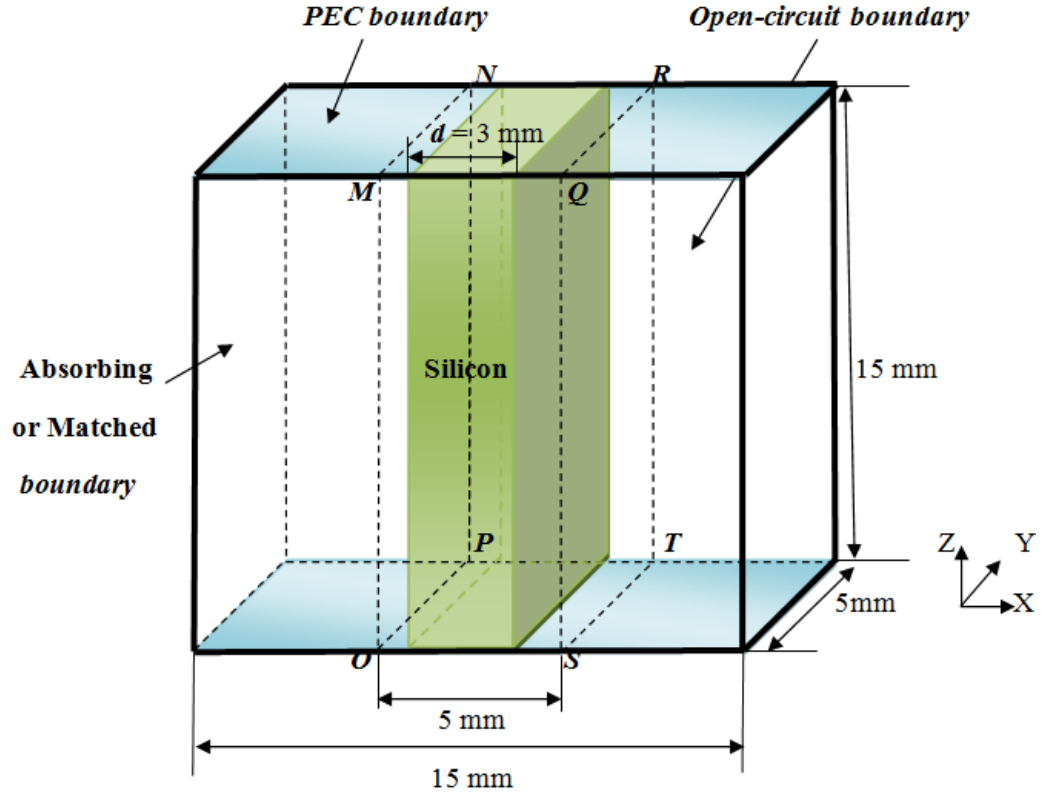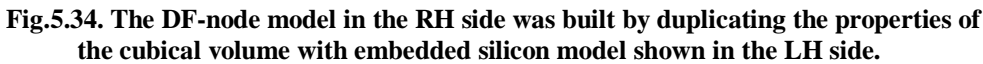
Fig.5.32 The TLM fine mesh with a silicon model, the space step of the model is 1 mm.

A coarse mesh model with a space step of 5 mm $(\Delta l_{DF} = 5\,\mathrm{mm})$ for the configuration shown in Fig.5.32 can be built by joining three homogeneous 5 mm x 5 mm x 5 mm DF-nodes (Fig.5.33) where the DF parameters are obtained from a 3 mm x 5 mm x 5 mm blocks with the silicon embedded into a 5 mm x 5 mm x 5 mm cubical volume with matched boundary conditions for all surfaces (Fig.5.34). In addition, the DF parameters for each DF functions in DF- SCN are obtained by using three and four poles. This coarse mesh model can be used to represent the same properties and characteristics as the fine mesh model in Fig.5.32 but with a much reduced computational cost.

Fig.5.33. The TLM coarse mesh with DF-nodes model (space step 5 mm).

Fig.5.34. The DF-node model in the RH side was built by duplicating the properties of the cubical volume with embedded silicon model shown in the LH side.

Comparison between the finely meshed model in Fig.5.32 and the coarse mesh with DF-nodes model in Fig.5.33 can be made by exciting both with a Gaussian Z-directed voltage source of amplitude 1volt with half-width of 0.85 ns on plane MNOP propagating along X-direction. The output voltages can be then be observed and the following comparisons made;

    (i)   The average reflected Z-directed voltages on the plane MNOP

    (ii)   The average transmitted forward Z-directed voltages on the plane QRST.

These comparisons in time and frequency domains are illustrated in Fig.5.35-5.38. Moreover, for this example, the frequency-domain results in Fig.5.36 and Fig.5.38 can be compared with analytical results which are readily calculated by using Fresnel's reflection formula. The full formulation can be found in [5.2]-[5.3] but is summarised in (2.22) – (2.24) for completeness:

For this example, the complex refractive index of the sample n and the angle of incidence θ are 3.96 and 0 respectively.
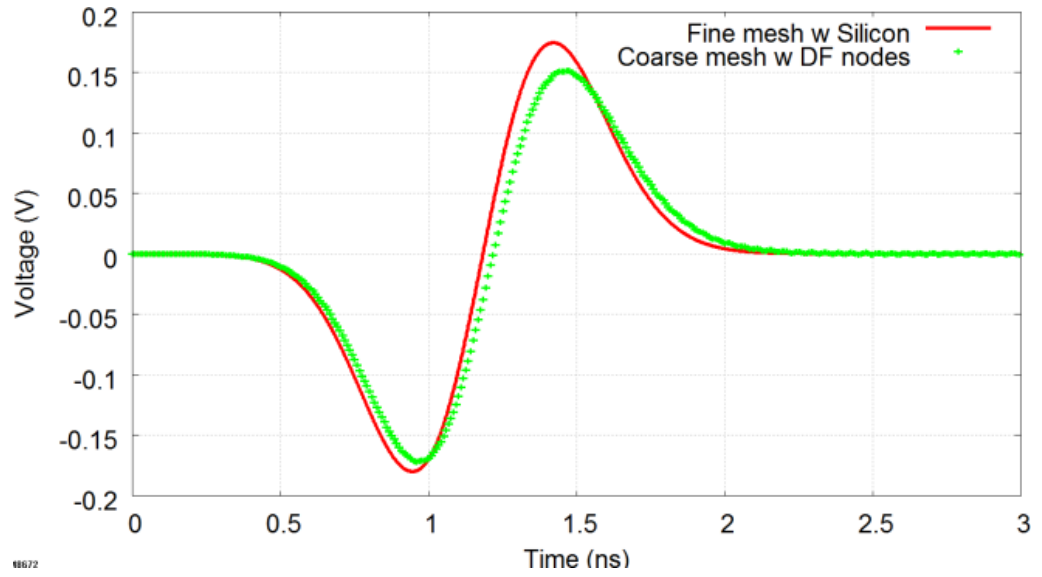
Fig.5.35 The average reflected Z-directed voltage on plane MNOP in the time domain.
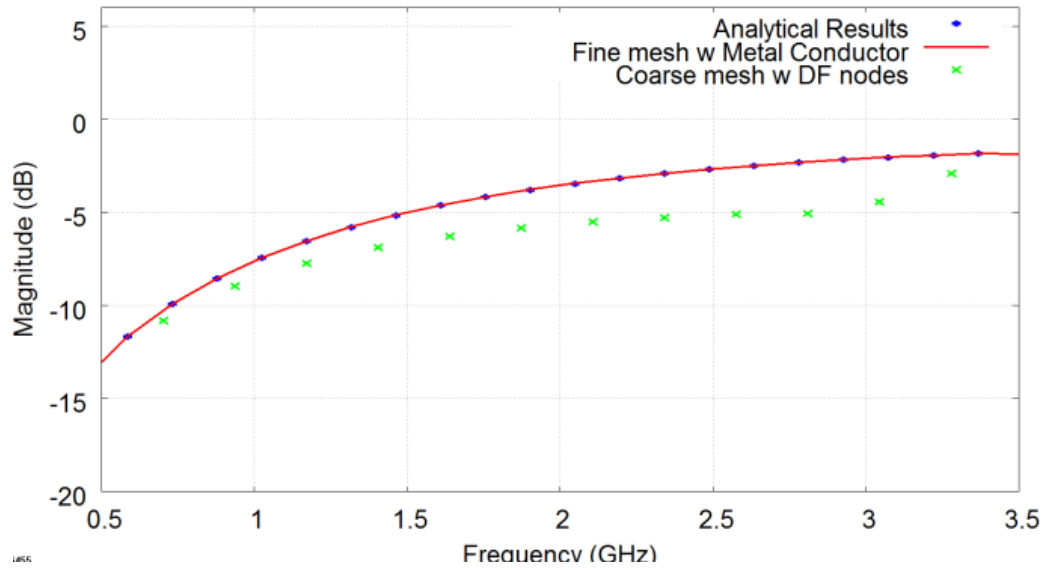

Fig.5.36 The average reflected Z-directed voltage on plane MNOP in the frequency

domain. MSE of the analytical result with respect the fine mesh with metal conductor

model and the coarse mesh with DF nodes model results between 0.5-3.5 GHz are 0.00
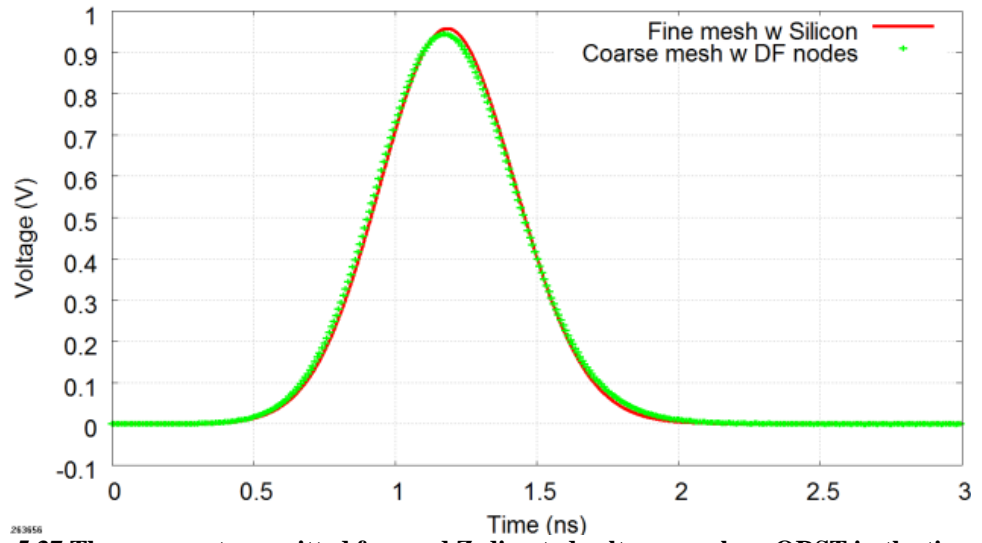
and 3.16 dB respectively.

Fig.5.37 The average transmitted forward Z-directed voltage on plane QRST in the time
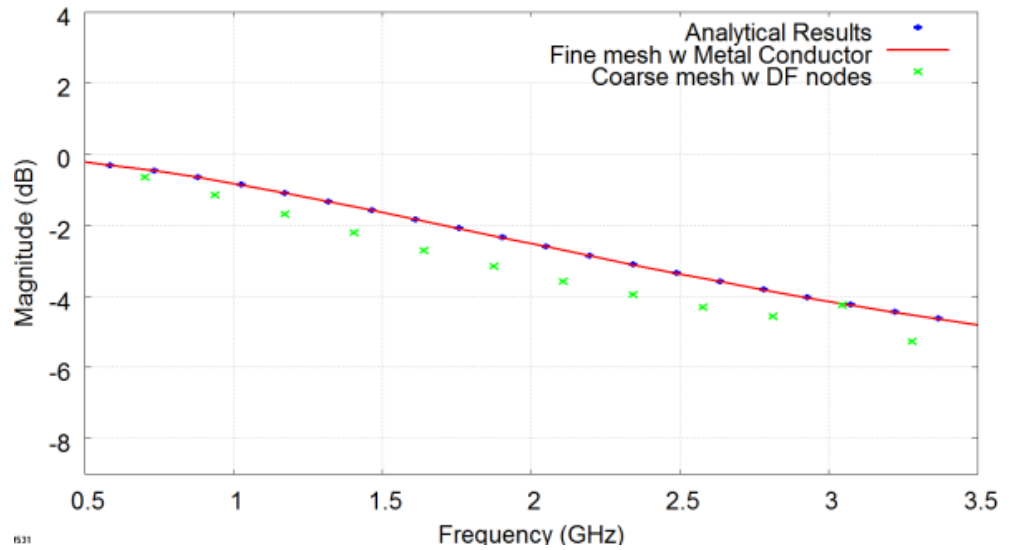
domain.

Fig.5.38 The average transmitted forward Z-directed voltage on plane QRST in the

frequency domain. MSE of the analytical result with respect the fine mesh with metal

conductor model and the coarse mesh with DF nodes model results between 0.5-3.5 GHz

are 0.00 and 0.56 dB respectively.

In Fig.5.35-5.38, the results obtained by the coarse mesh with DF-nodes model in Fig.5.33 are close to the ones obtained by the fine mesh with silicon model in Fig.5.32 and with the analytical results. The highest difference in relative magnitude of results is around 2.6 dB at the frequency of 2.76 GHz approximately as illustrated in Fig. 5.36.

As mentioned, the DF parameters for each DF functions in DF- SCN are obtained by using three and four poles to construct the DF nodes in the coarse mesh with DF nodes model in Fig.5.33. The gaps of magnitude between the results of two methods can be decreased by increasing number of poles. However, the computational costs are required higher.

The computational requirements are given in Table 5.2 again confirming that the proposed model gives much reduced computational demands.

TABLE 5.2

The comparison of the computational requirements of the two models in Fig.5.17 and 5.18.

Model	Number of nodes (NX)x(NY)x(NZ)	Number of time-steps	Memory (kB)	CPU Time (s)
Fine mesh with a dielectric material $(\Delta l_f = 1mm)$	15 x 5 x 15	4096	1480	4.187
Coarse mesh with the DF nodes model $(\Delta l_{DF} = 5mm)$	3 x 1 x 3	512	644	0.359

The computer used for the TLM simulation has Intel®Core ™ i7 CPU processor with 1.60 GHz and installed memory (RAM) of 4.00 GB.

133

5.3.4 The last example

The example demonstrated in this section is a "two-layers of via model" as illustrated in Fig.5.39. A conducting via of 1 mm x 1 mm x 5 mm is connected between two metal conducting plates at top and the bottom (Zmax and Zmin) of a 102.5 mm x 7.5 mm x 5 mm rectangular air-space problem. There is a square hole of 2.5 mm x 2.5 mm (X x Y) located within the conducting plate at the centre of the problem. This hole allows the via passed through in order to connect between top and bottom of the air-space problem. The space-step of this model is 0.25 mm $(\Delta l_f = 0.25 \text{mm})$. The boundaries conditions are PEC at the top and bottom of the model (Zmin-Zmax), open-circuit boundary conditions for Ymin-Ymax and matched boundary conditions for Xmin-Xmax. Examples of via designs can be also found in [5.4]-[5.7].

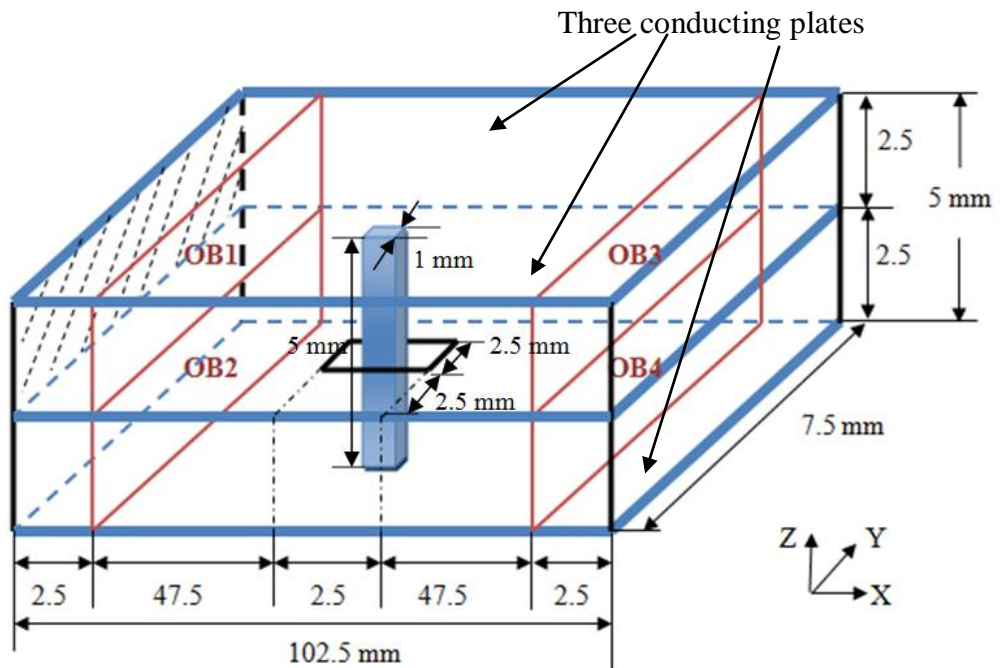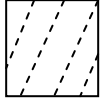**Fig.5.39 A via of 1 mm x 1 mm x 5 mm embedded into the centre of air-space box of 102.5 mm x 7.5 mm x 5 mm.** $(\Delta l_f = 0.25 \text{mm})$

where,

 = metal box of 1 mm x 1 mm x 5 mm   (*X* x *Y* x *Z*)

 = a hole area (slot) of 2.5 mm x 2.5 mm (*X* x *Y*)

 = Average Input Voltage Source area of 1 V.

OB = Observation area 'i' where i is 1, 2, 3 and 4

The DF node for this case can be constructed by duplicating the properties of a via of 1 mm x 1 mm x 2.5 mm embedded inside a matched-boundaries' cube of 2.5 mm x 2.5 mm x 2.5 mm as shown in Fig. 5.40.
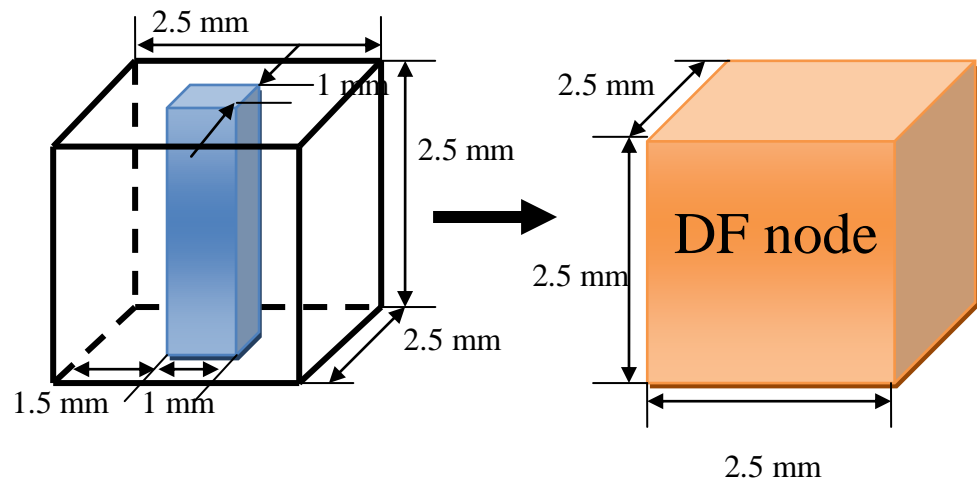

Fig.5.40 A metal box of 1 mm x 1 mm x 2.5 mm embedded into a matched-boundaries' cube of 2.5 mm x 2.5 mm x 2.5 mm with the space-step of 0.25 mm (LH side) is transformed to a DF node of 2.5 mm x 2.5 mm x 2.5 mm with the space-step of 2.5 mm (RH side).

To compare between the fine mesh and coarse DF nodes models in Fig.5.40, two DF nodes in Fig.5.40 on RH side are embedded into the model in Fig. 5.39 by replacing the conducting via at the same location. As a result, the coarse mesh with DF nodes model is obtained as shown in Fig.5.41. The space-step is 2.5mm $(\Delta l_{DF} = 2.5\text{mm})$.
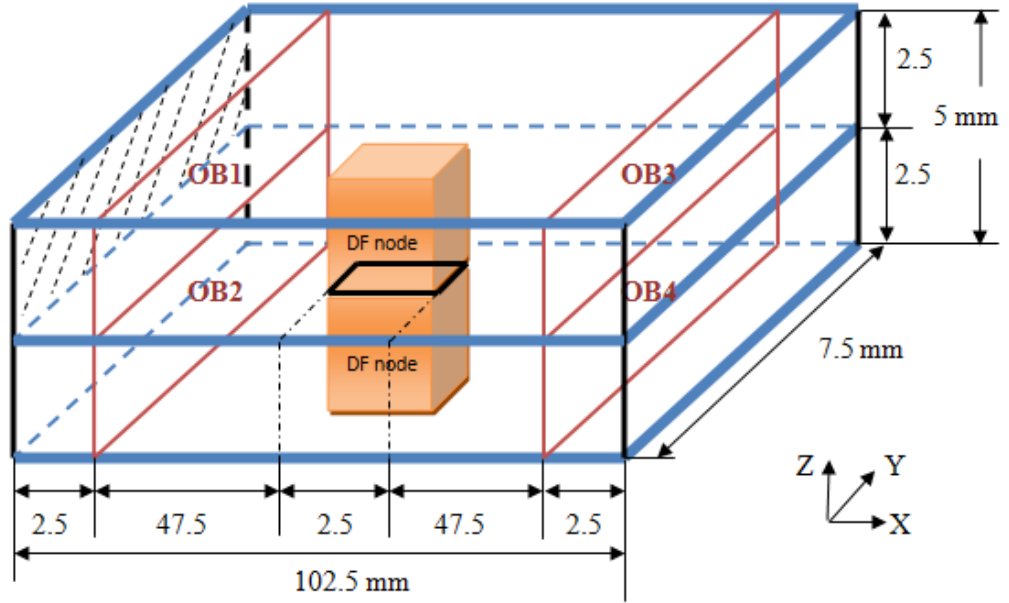

Fig.5.41 Two DF nodes of 2.5 mm x 2.5 mm x 2.5 mm are connected together and placed into the position as a conducting via in the centre of the rectangular air-space problem of 102.5 mm x 7.5 mm x 5 mm with the space-step of 2.5 mm $(\Delta l_{DF} = 2.5\text{mm})$**.**

The comparison between the fine mesh with a conducting via and the coarse mesh with DF nodes can be made by exciting the spatially averaged input Z-directed voltage of 1 V in Gaussian form with half-width of 1 ns on plane at Xmin area between top and middle conducting plates. The propagation is along X-direction. Then, the spatially averaged output Z-directed voltages are

measured at the observation area,OB1, OB2, OB3 and OB4 and the following comparisons can be made;

(i)   The spatially averaged input Z-directed voltages at OB1 area;

(ii)   The spatially averaged reflected Z-directed voltages at OB1 area

(iii)   The spatially averaged transmitted backward Z-directed voltage at OB2 area

(iv)   The spatially averaged transmitted forward Z-directed voltage at OB3 area;

(v)   The spatially averaged transmitted forward Z-directed voltage at OB4 area.

These comparisons are shown in Fig.5.42-5.50 in both the time and frequency domains.

Fig.5.42 The spatially averaged input Z-directed voltages at OB1 area in the time domain.

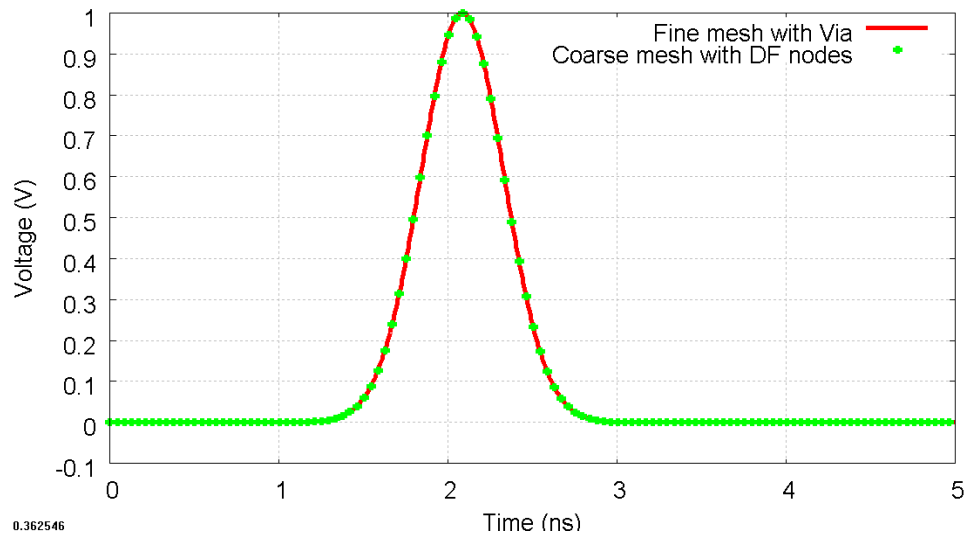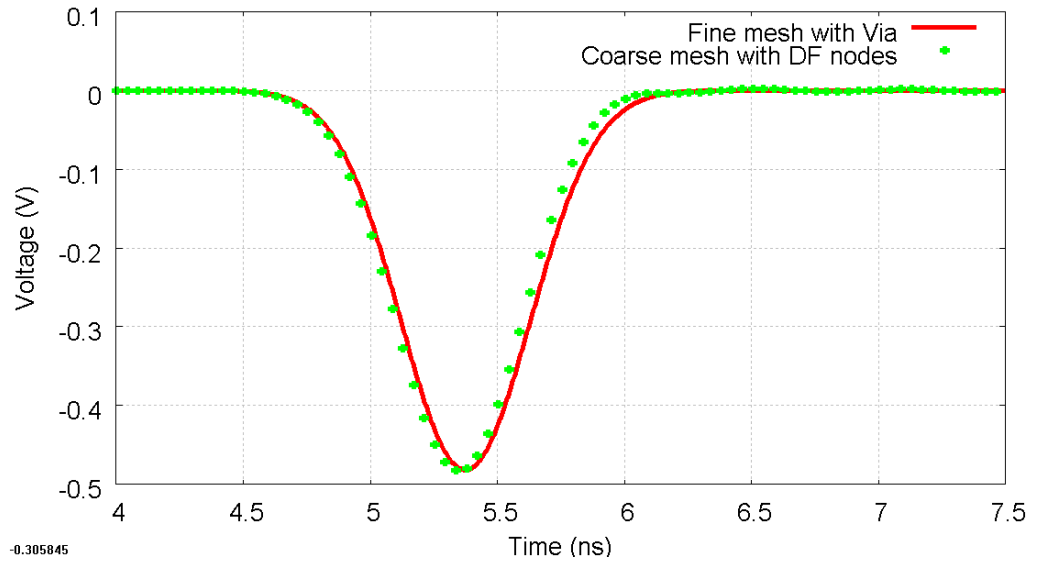**Fig.5.43 The spatially averaged reflected Z-directed voltages at OB1 area in the time domain.**

Fig.5.44 The spatially averaged reflected Z-directed voltages at OB1 area in the frequency domain.
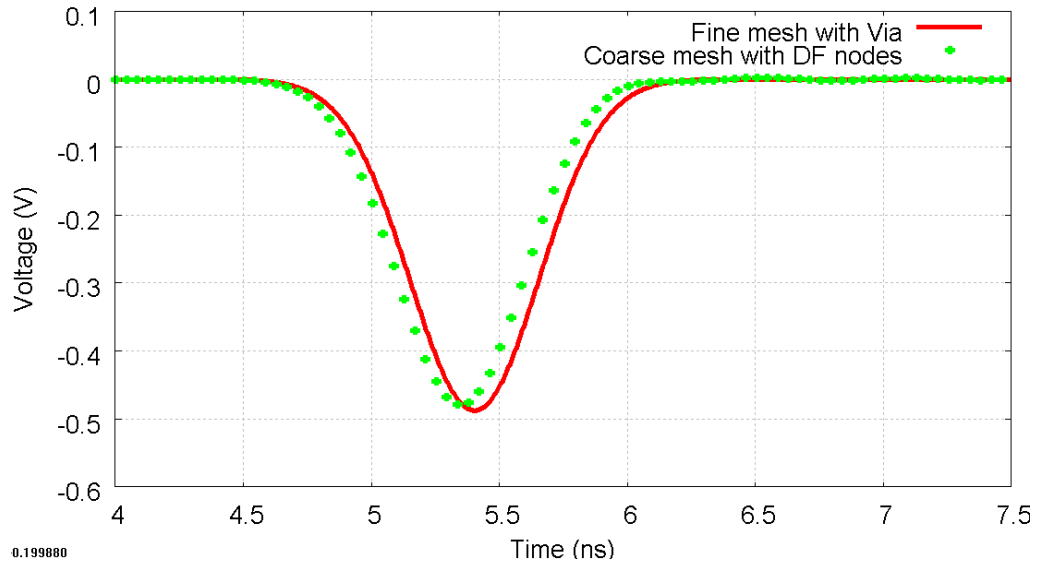
Fig.5.45 The spatially averaged transmitted backward Z-directed voltages at OB2 area in the time domain.

Fig.5.46 The spatially averaged transmitted backward Z-directed voltages at OB2 area in the frequency domain.

139

Fig.5.47 The spatially averaged transmitted forward Z-directed voltages at OB3 area in the time domain.

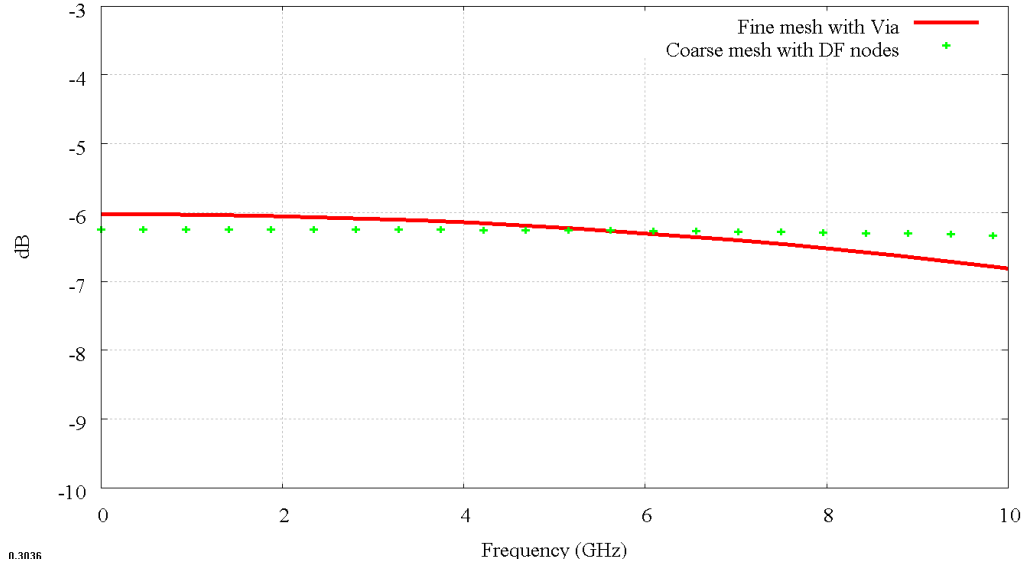**Fig.5.48 The spatially averaged transmitted forward Z-directed voltages at OB3 area in the frequency domain.**

Fig.5.49 The spatially averaged transmitted forward Z-directed voltages at OB4 area in the time domain.
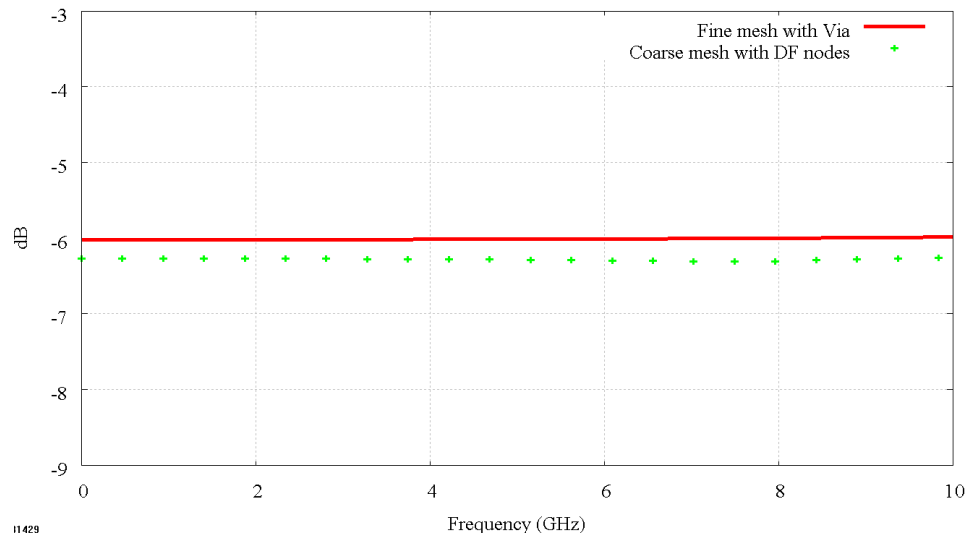
Fig.5.50 The spatially averaged transmitted forward Z-directed voltages at OB4 area in the frequency domain.
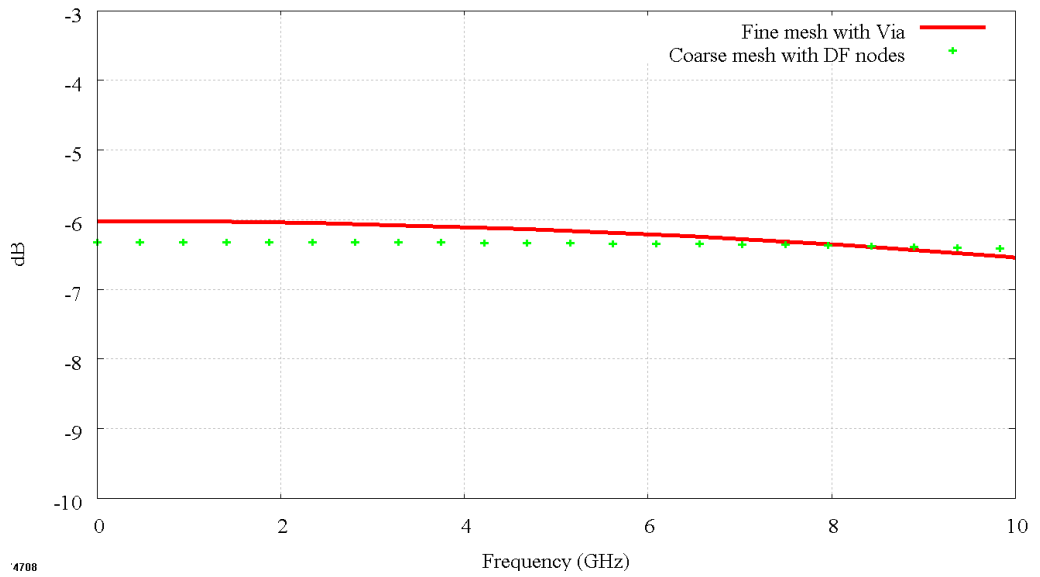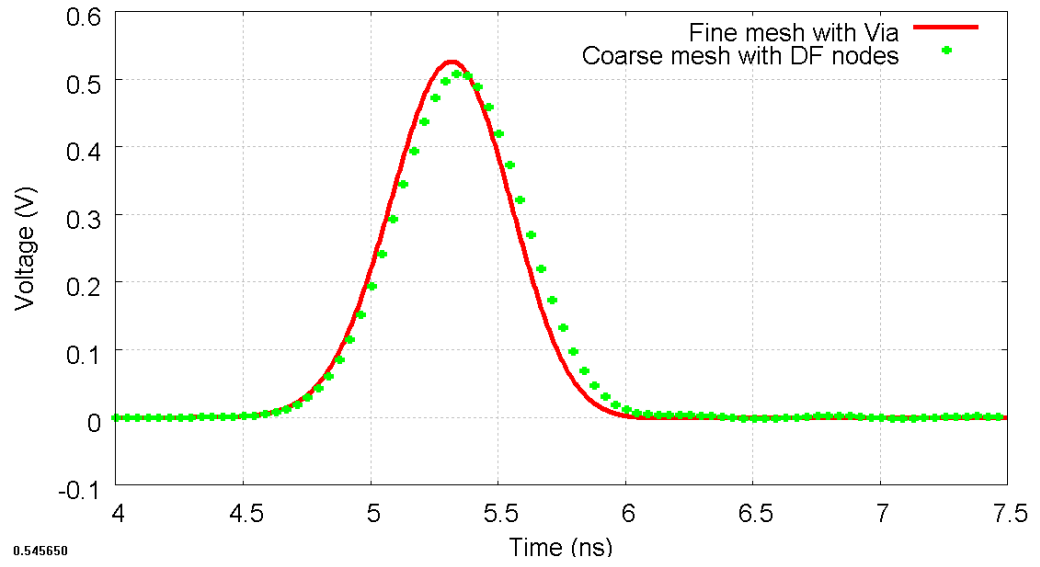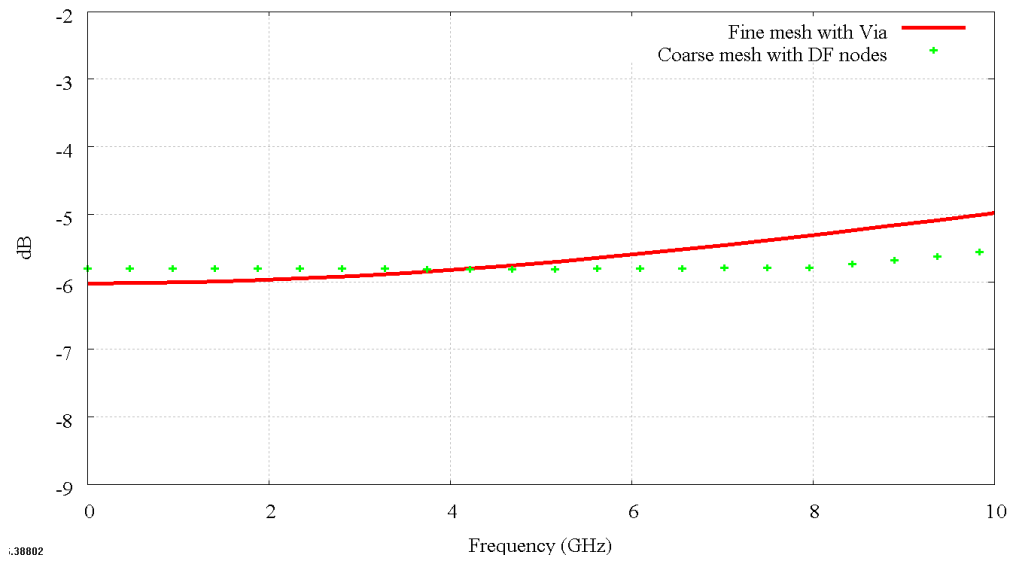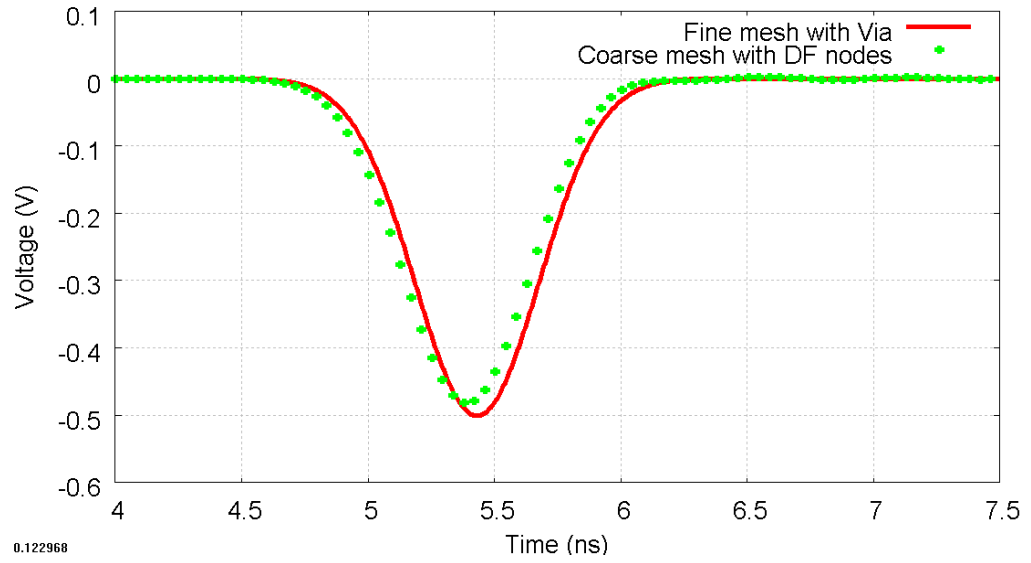
In Fig. 5.42-5.50, the maximum frequency for these comparisons is around 12 GHz, limited by the $\lambda/10$ rule and the mesh dispersion in the TLM coarse mesh. However, the frequencies shown in these figures are limited at 10 GHz,

because the energy of the input voltage—a Gaussian pulse with a half-width of 0.85 ns—is band limited at 10 GHz.

There are slight differences in the time-domain results shown in Fig. 5.43, Fig. 5.45, Fig. 5.47 and Fig. 5.49, between the two methods. The highest difference in magnitude was found to be approximately 0.02V, which was found in Fig.5.49.

In the frequency-domain results in Fig. 5.44, Fig. 5.46, Fig. 5.48 and Fig. 5.50, the highest magnitude difference of approximately 0.6 dB was found in the graph of the average reflected Z-directed voltages at OB1 area and the average transmitted forward Z-directed voltages at OB3 area. These errors occur in the high frequency range of 8-10 GHz.

A comparison of the computational requirements of the two methods is given in Table5.3.

TABLE 5.3

The comparison of the computational requirements between two models in Fig.5.24 and 5.26.

Model	Nodes (X)x(Y)x(Z)	Time Steps	Memory (MB)	CPU Time (s)
Fine mesh with two-layer of a via	410x30x20	4096	70.33	298.34
Coarse mesh with the DF-nodes	41x3x2	512	2.56	0.87

The computer used for the TLM simulation has an Intel®Core ™ i7 CPU clocked at 1.60 GHz and has an installed memory (RAM) of 4.00 GB.

5.4   Conclusion

This chapter introduced and described further development of the DF technique. This technique developed from the initial DF technique can duplicate the properties of fine features in three-dimensions completely with computational cost savings. Another advantage of the presented technique is that the DF nodes can now be connected to represent a larger object. However, a typical disadvantage of the technique is that the highest frequency of the results is limited by the $\lambda/10$ rule or by the mesh dispersion in TLM coarse mesh.

Three examples were used to demonstrate the further development of the DF technique in this chapter;

(i)   The first example is a metal-conductor model, which demonstrated the method of joining DF nodes to represent complex embedded objects. In addition, the unusual way of extracting DF parameters from a boundary area attached to a metal conductor part was explained.

(ii)   The second example demonstrated the application of the further DF technique to the three-dimensional stub loaded SCN. The technique shows a good agreement with the standard TLM and the analytical results in the time and the frequency domains.

(iii)   The last example is a simple two-layer via model, which represents the connection between two DF nodes. It was excited by an input voltage fed into the top DF node between the top and the middle conducting plates. Then, the outputs were observed at the area between the middle and the bottom conducting plates. The results

between the fine mesh with the via and the coarse mesh with the DF nodes were found to be similar. Therefore, it was confirmed that the bottom DF node (the DF node located between the middle and the bottom conducting plates) can receive/transmit responses from/to the top DF node correctly.

5.5   References

[5.1]   M. A. Green and M. J. Keevers, "Optical properties of intrinsic silicon at 300 K", *Progress in Photovoltaics: Research and Applications*, vol. 3, (3), pp. 189 - 192, 1995.

[5.2]   K. Sato, H. Kozima, H. Masuzawa, T. Manabe, T. Ihara, Y. Kasashima, K. Yamaki and T. Tanaka, "Measurements of Reflection Characteristics and Refractive Indices of Interior Construction Materials in Millimeter-Wave Bands,"   *in Proc. 45th IEEE Veh. Technol.*, vol. 1, pp. 449-453, Jul. 1995.

[5.3]   A. Ishimaru, "Electromagnetic Wave Propagation, Radiation, and Scattering," Chap. 3, Prentice-Hall, Englewood Cliffs, NJ, 1991.

[5.4]   H.-G. Low, "Via design optimisation for high speed device packaging," *Electronics Packaging Technology Conference, 1998. Proceedings of 2nd,* pp. 112-118.

[5.5]   W. D. Becker, P. H. Harms and R. Mittra "Time domain electromagnetic analysis of a via in a multilayer computer chip package", *IEEE MTT-S Digest*, pp.1229 -1232, 1992 **.**

[5.6]   R. Sorrentino, F. Alessandri, M. Mongiardo, G. Avitabile and L. Roselli "Full-wave modeling of via-hole grounds in microstrip by 3-D mode matching technique", *IEEE Trans. Microwave Theory Tech.*, vol. 39, no. 12, pp.2228 -2234 1992.

[5.7]   C. Eswarappa and W. J. R. Hoefer "Time domain analysis of shorting

pins in microstrip using 3-D SCN TLM", *IEEE MTT-S Digest*, pp.917

-920,1993.

6.   Conclusions and Future Work

The DF technique has been developed for the three-dimensional TLM method in order to investigate the electromagnetic fields and characteristic behaviors of fine embedded objects accurately. This developed technique can be used for general problems in three-dimensions. The limitations and conditions of usage are discussed here.

6.1   Conclusion

The first chapter discussed the multi-scale problem in numerical methods by using an example of a thin wire inside a regular mesh to demonstrate the problems. The typical solutions for this problem include applying a multi-grid mesh or a hybrid mesh. Both of them are suitable for time-domain simulations such as TLM and FDTD. They also have some limitations and conditions when they applied to solve a problem.

One popular technique that is used to solve multi-scale problems is the TLM multiple grid scheme method that uses fine and coarse meshes to observe electromagnetic fields under four conditions;

> (i)   charge conservation
>
> (ii)   energy conservation
>
> (iii)   no reflections
>
> (iv)   zero delays

The DF technique is a recent technique that can be used to solve this problem and it has been developed as demonstrated in this thesis for general three-dimensional problems.

This chapter also introduced the basics of the TLM method and the DF techniques.

Chapter 2 first provided the history of the three-dimensional TLM. The three-dimensional TLM node was developed from the expanded and the asymmetrical condensed nodes. The recent TLM node is called the three-dimensional SCN introducing by Johns in 1986. The chapter contains the mathematic equations describing the SCN and the procedures to employ three-dimensional SCN nodes in a TLM simulation. These procedures were summarised in schematic diagrams.

The use of stub loading in the three-dimensional TLM was discussed as it is necessary to model fine features such as dielectric and magnetic materials. Then, the example of the stub loaded model was presented in order to demonstrate the accuracy of the simulation program created for the project by comparing the simulation against an analytical result provided by Fresnel formulae [6.1].

The chapter also described the errors and limitations in the three-dimensional TLM method. The typical sources of errors are;

> (i)   coarseness errors

(ii)   velocity error s

(iii)   misalignment of boundaries and dielectric interfaces especially in inhomogeneous structures.

Chapter 3 described the DF technique applied to three-dimensional problems combining four techniques;

(i)   The Fast Fourier Transform (FFT)

(ii)   The frequency-domian Prony's method

(iii)   The Laguerre's Method

(iv)   The Bilinear-Z-transform

These four techniques were applied to the time-domain responses of a fine feature in a time-domain simulation in order to estimate the DF parameters. Then, the digital filters (DFs) were embedded at the surface between three-dimensional TLM nodes and the calculation was accounted for the "connection" process in the TLM simulation.

The fine mesh with a stub loaded model was used to determine the DFs next. These DFs were then placed at the same position as the stub loaded node, but with a coarse mesh model. The comparisons were made and it showed a good agreement between both methods; but the coarse mesh with DFs model had much lower computational requirements.

The chapter also pointed out that the limitation of this technique is that only the responses of single node faces (one dimension) are considered because the DFs can only be placed between TLM nodes as a plane or as an internal boundary.

Chapter 4 introduced a further development of the DF technique. In order to develop the technique, simply, the DF plane or the internal boundary was

149

extended to every external surface except for the surfaces connected to the conducting surfaces, to make a cube called the "DF node". As a result, it provided the electromagnetic properties in two dimensions. Moreover, the DF node was a three-dimensional SCN node which contained many DF transfer functions as given in (3.17).

The limitations and conditions of the initial development of the DF technique were;

(i)   The fine feature must be modelled in a TLM fine mesh with some cubical volume as a TLM coarse mesh node.

(ii)   The relationship between the space steps of the cubical volume containing the fine feature in a fine mesh Δl_f and the coarse DF node Δl_{DF} is $\Delta l_{DF} = n\Delta l_f$.

(iii)   The fine feature must be placed between two metal conducting surfaces.

The chapter also gave the explanation for the use of the time shifting in determining the coefficients of the DF function. Then, a fine mesh with a thin-wire model placed in a large air-space problem was used to demonstrate the technique.

Moreover, the example in this chapter showed that choosing the number of poles and sampling points (NP, NS) to create the DF node, affects the characteristics of the results. It showed that the results can be improved by creating a DF node with an increased number of poles and sampling points.

Chapter 5 provided further development of the DF technique demonstrating how to construct a DF node from fine embedded objects. The DF obtained

from this technique could provide the electromagnetic properties in every dimension. They could also connect to each other and could be combined to represent a complex object. The technique has the same conditions as the initial DF technique except that it is not necessary to place the object between two metal conducting surfaces.

The examples in chapter 5 represented multiple applications. The first example illustrated the method's capability in joining DF nodes to represent an embedded object. The second example was used to show that the accuracy is acceptable compared to the analytical results. The last example was used to show that the voltage responses from adjacent DF nodes are correct.

The initial and further DF techniques have been developed to solve and minimise the multi-scale problems in three-dimensional TLM. The advantages of these were given. The disadvantages include the high frequency limitation of the result by $\lambda/10$ rule and the large mesh dispersion in a coarse TLM mesh.

6.2   Future work

There are short and long term plans for future work.

For short term plans, the developed DF technique was demonstrated with relatively simple examples such as dielectric materials and conducting objects. The technique needs to be applied to more general problems for complete validation. A microstrip line with two-vias model [6.2] is a sizable problem

that can be simulated to make comparisons between the DF techniques and the experimental results. Moreover, this model can be developed from the last example in chapter 5 as shown in Fig. 6.1 and Fig. 6.2.

For longer term plans, as mentioned in chapter 3, the DF technique can be also applied to the FDTD method. In theory, the main difference between 3D-TLM and FDTD nodes is that, in FDTD, the electric and magnetic fields are not measured at the same point in space, and that it requires a half time-step to do so. But, in TLM, they can be measured at the same position and at the same time instance. Therefore, the developed DF technique should be able to be used in FDTD method by creating a DF node, which has the DF transfer functions $(DF())$ for both fields separately. However, it might require double the number of DF functions as the magnetic and electric fields are done separately in a DF-node scattering matrix (DFS) which may lead to high computational costs.
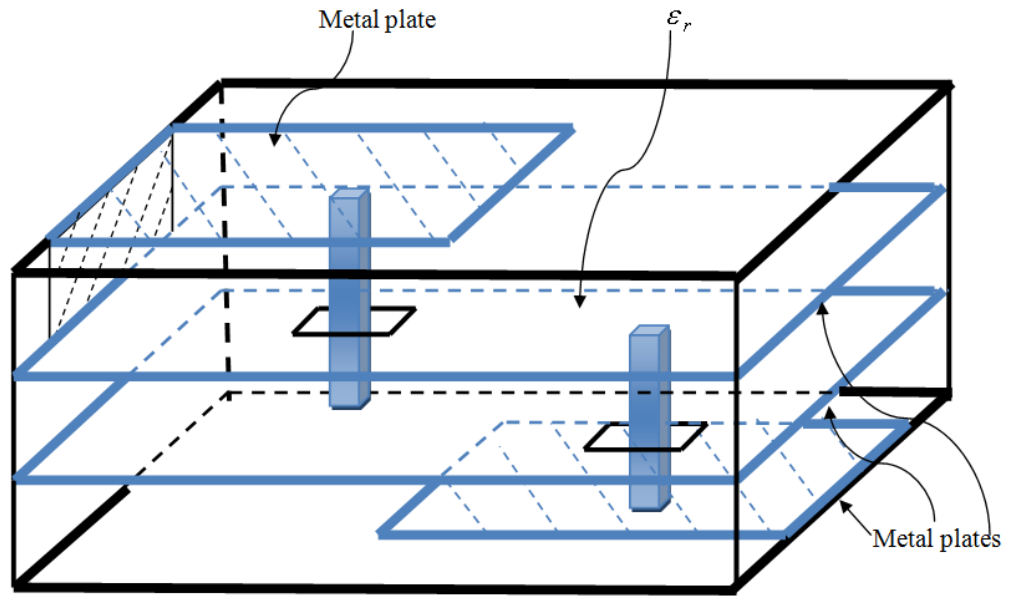
Fig.6.1 A fine mesh microstrip line with two vias model which contains the dielectric substrate of ε_r between metal plates. Space step is Δl_f
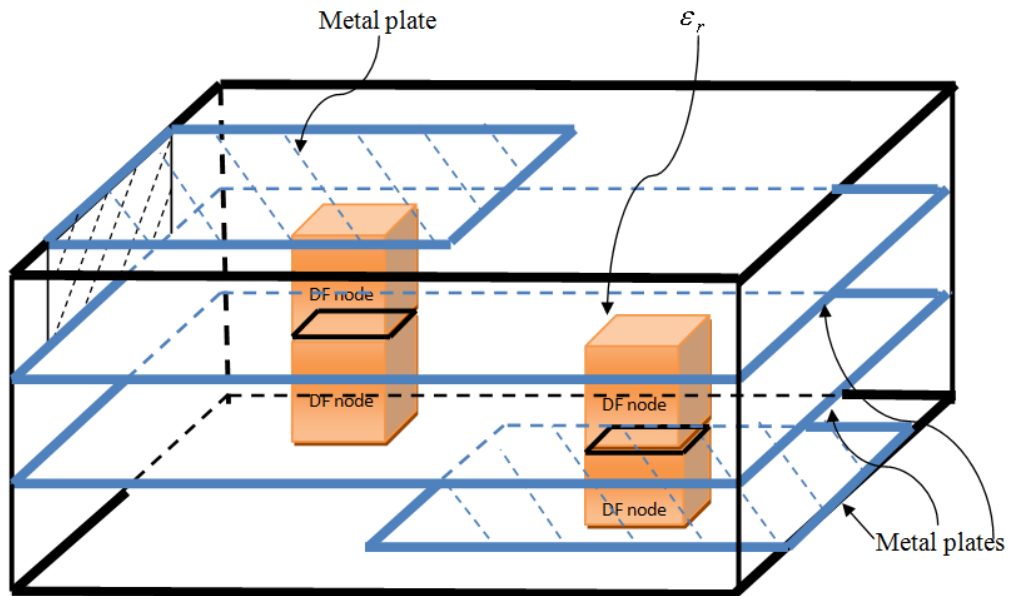
Fig.6.2 A Coarse mesh microstrip line with DF nodes model of ε_r. Space step is

$$\Delta l_{DF} = n\Delta l_f$$

6.3 References

[6.1] K. Sato, H. Kozima, H. Masuzawa, T. Manabe, T. Ihara, Y. Kasashima, K. Yamaki, T. Tanaka, "Measurements of Reflection Characteristics and Refractive Indices of Interior Construction Materials in Millimeter-Wave Bands," *in Proc. 45th IEEE Veh. Technol.*, vol. 1, pp. 449-453, Jul. 1995.

[6.2] A. S. Cimiński and B. J. Janiczak, "Efficient modeling of the time-domain crosstalk phenomena in coupled microstrip lines," *Microwave and Optical Technology Letters*, vol. 46, no.4, pp. 326-331, Aug. 2005.

Appendix

The complete derivation of formulae from (3.8) to (3.12) with an example of 3 poles

Equation (3.8) is

$$F(s) = \frac{b_{NP}(s - s_{z0})(s - s_{z1})\cdots(s - s_{z(NP-1)})}{(s - s_{p0})(s - s_{p1})\cdots(s - s_{p(NP-1)})} \tag{A1}$$

For $NP = 3$, $F(s)$ in (A1) can be obtained as given in (A2).

$$F(s) = \frac{b_3(s - s_{z0})(s - s_{z1})(s - s_{z2})}{(s - s_{p0})(s - s_{p1})(s - s_{p2})} \tag{A2}$$

The bilinear Z-transform as given in (A3) is substituted to (A2). Then, $F(z)$ can be obtained by following step in (A4) and (A5).

$$s \xrightarrow{\quad z \quad} \frac{2}{\Delta t}\left(\frac{1 - z^{-1}}{1 + z^{-1}}\right) \tag{A3}$$

Appendix

Giving that,

$$\left(s - s_{zi}\right) = \alpha_{zi}\left(\frac{1 - z^{-1}\beta_{zi}}{1 + z^{-1}}\right) \tag{A4a}$$

and

$$\left(s - s_{pi}\right) = \alpha_{pi}\left(\frac{1 - z^{-1}\beta_{pi}}{1 + z^{-1}}\right) \tag{A4b}$$

where $\qquad \alpha_{zi} = \dfrac{2 - s_{zi}\Delta t}{\Delta t}$, $\beta_{zi} = \dfrac{2 + s_{zi}\Delta t}{2 - s_{zi}\Delta t}$,

$$\alpha_{pi} = \frac{2 - s_{pi}\Delta t}{\Delta t} \ , \ \beta_{pi} = \frac{2 + s_{pi}\Delta t}{2 - s_{pi}\Delta t}$$

(A4) substitutes into (A2),

$$F(z) = b_3 . \frac{\alpha_{z0}\left(\dfrac{1 - z^{-1}\beta_{z0}}{1 + z^{-1}}\right)\alpha_{z1}\left(\dfrac{1 - z^{-1}\beta_{z1}}{1 + z^{-1}}\right)\alpha_{z2}\left(\dfrac{1 - z^{-1}\beta_{z2}}{1 + z^{-1}}\right)}{\alpha_{p0}\left(\dfrac{1 - z^{-1}\beta_{p0}}{1 + z^{-1}}\right)\alpha_{p1}\left(\dfrac{1 - z^{-1}\beta_{p1}}{1 + z^{-1}}\right)\alpha_{p2}\left(\dfrac{1 - z^{-1}\beta_{p2}}{1 + z^{-1}}\right)}$$

$$F(z) = \left(b_3 \frac{\alpha_{z0}\alpha_{z1}\alpha_{z2}}{\alpha_{p0}\alpha_{p1}\alpha_{p2}}\right) . \frac{\left(1 - z^{-1}\beta_{z0}\right)\left(1 - z^{-1}\beta_{z1}\right)\left(1 - z^{-1}\beta_{z2}\right)}{\left(1 - z^{-1}\beta_{p0}\right)\left(1 - z^{-1}\beta_{p1}\right)\left(1 - z^{-1}\beta_{p2}\right)}$$

$$\tag{A5a}$$

Appendix

Let $B_0 = \left(b_3 \dfrac{\alpha_{z0}\alpha_{z1}\alpha_{z2}}{\alpha_{p0}\alpha_{p1}\alpha_{p2}} \right)$, $F(s)$ in (A5a) can be obtained as given in (A5b).

$$F(z) = B_0 \cdot \frac{\left(1 - z^{-1}\beta_{z0}\right)\left(1 - z^{-1}\beta_{z1}\right)\left(1 - z^{-1}\beta_{z2}\right)}{\left(1 - z^{-1}\beta_{p0}\right)\left(1 - z^{-1}\beta_{p1}\right)\left(1 - z^{-1}\beta_{p2}\right)} \qquad \text{(A5b)}$$

Then, carry out multiplication in (A5b).

$$F(z) = B_0 \cdot \frac{\left(1 - z^{-1}\beta_{z0} - z^{-1}\beta_{z1} + z^{-2}\beta_{z0}\beta_{z1}\right)\left(1 - z^{-1}\beta_{z2}\right)}{\left(1 - z^{-1}\beta_{p0} - z^{-1}\beta_{p1} + z^{-2}\beta_{p0}\beta_{p1}\right)\left(1 - z^{-1}\beta_{p2}\right)}$$

$$F(z) = \frac{B_0 + z^{-1}\left(-B_0\left(\beta_{z0} + \beta_{z1} + \beta_{z2}\right)\right) + z^{-2}\left(B_0\left(\beta_{z0}\beta_{z1} + \beta_{z0}\beta_{z2} + \beta_{z1}\beta_{z2}\right)\right) + z^{-3}\left(-B_0\left(\beta_{z0}\beta_{z1}\beta_{z2}\right)\right)}{1 + z^{-1}\left(-\beta_{p0} - \beta_{p1} - \beta_{p2}\right) + z^{-2}\left(\beta_{p0}\beta_{p1} + \beta_{p0}\beta_{p2} + \beta_{p1}\beta_{p2}\right) + z^{-3}\left(-\beta_{p0}\beta_{p1}\beta_{p2}\right)}$$

Appendix

$$F(z) = \frac{B_0 + \sum\limits_{i=1}^{3} B_i z^{-i}}{1 + \sum\limits_{i=1}^{3} A_i z^{-i}} \qquad \text{(A5c)}$$

where

$$B_1 = -B_0\left(\beta_{z0} + \beta_{z1} + \beta_{z2}\right)$$

$$B_2 = B_0\left(\beta_{z0}\beta_{z1} + \beta_{z0}\beta_{z2} + \beta_{z1}\beta_{z2}\right)$$

$$B_3 = -B_0\left(\beta_{z0}\beta_{z1}\beta_{z2}\right)$$

$$A_1 = -\left(\beta_{p0} + \beta_{p1} + \beta_{p2}\right)$$

$$A_2 = \beta_{p0}\beta_{p1} + \beta_{p0}\beta_{p2} + \beta_{p1}\beta_{p2}$$

$$A_3 = -\beta_{p0}\beta_{p1}\beta_{p2}$$

Then, $B_0 A_i z^{-i}$ is added and subtracted in the numerator inside the SUM of

(A5c). We obtains

$$F(z) = \frac{B_0 + \sum\limits_{i=1}^{3}\left(B_i z^{-i} + B_0 A_i z^{-i} - B_0 A_i z^{-i}\right)}{1 + \sum\limits_{i=1}^{3} A_i z^{-i}}$$

$$F(z) = \frac{B_0\left(1 + \sum\limits_{i=1}^{3} A_i z^{-i}\right) + \sum\limits_{i=1}^{3}\left(B_i - B_0 A_i\right)z^{-i}}{1 + \sum\limits_{i=1}^{3} A_i z^{-i}}$$

$$F(z) = B_0 + \frac{\sum\limits_{i=1}^{NP}\left(B_i - B_0 A_i\right)z^{-i}}{1 + \sum\limits_{i=1}^{NP} A_i z^{-i}} \tag{A5d}$$

Let $B'_i = B_i - B_0 A_i$, then $F(z)$ can be obtained as given in (A5e) which is the

same as (3.12) in chapter 3.

$$F(z) = B_0 + \frac{\sum\limits_{i=1}^{NP} B'_i z^{-i}}{1 + \sum\limits_{i=1}^{NP} A_i z^{-i}} \tag{A5e}$$